19960503 134

AXISYMMETRIC FILAMENTARY STRUCTURES

by A. F. Fraser, P. R. Preiswerk,
M. D. Benton, and O. R. Burggraf

Prepared by
ASTRO RESEARCH CORPORATION
Santa Barbara, Calif.
for

NATIONAL AERONAUTICS AND SPACE ADMINISTRATION • WASHINGTON, D. C. • APRIL 1970

AXISYMMETRIC FILAMENTARY STRUCTURES

By A. F. Fraser, P. R. Preiswerk,
M. D. Benton, and O. R. Burggraf

CONTENTS

LIST OF ILLUSTRATIONS

AXISYMMETRIC FILAMENTARY STRUCTURES

By A.F. Fraser, P.R. Preiswerk,
M.D. Benton, and O.R. Burggraf
Astro Research Corporation

SUMMARY

The theory of filamentary axisymmetric structures is broadened to include surface loads other than normal pressure. Structures with two sets of symmetrically disposed fiber are considered in detail, and force transfer between filaments is accounted for in the theory.

The governing equations are derived, and isotensoid surface shapes are determined and classified for a wide range of load conditions. The governing equations are also applied to problems where the surface shape and loading are prescribed and the filament geometry and load variation in the surface are to be determined.

The general nature of filamentary structures is discussed in depth, and useful qualitative results are obtained for multiple layer nets.

A non-axisymmetric isotensoid (or isocompressoid) is obtained as a special limiting case. The shape is a cylindrical paraboloid, and the load is equivalent to a gravity force field. Application in civil engineering structures is indicated.

INTRODUCTION

The observed strength of many materials is often greatly increased if they are tested in the form of thin filaments. For example, continuous glass filaments can be produced with reproducible tensile strengths ranging from 200 000 to 700 000 psi. Bulk glass, on the other hand, is usually limited to tensile strengths in the order of 10 000 to 50 000 psi.

The high strength of filaments is being exploited at an increasing rate in the aircraft, space, and missile industries. The volume of recently published information relating to filament materials is a good indication of the current level of effort expended in both industrial and Government laboratories determining material properties and performing design and stress analyses. In the analysis and design areas, there are two different but overlapping approaches; one is associated with composite-material structures and the other with filament-dominated structures. By way of definition, in the former, the filaments are embedded in a structural matrix which to a significant extent affects the performance of the material in structural applications. In the latter, whether or not there is a matrix, the stiffness and strength of the filaments completely dominate the structural performance of the material.

Methods of analysis of composite materials are based on anisotropic elasticity or shell theories (see e.g. Ref. 1). The accuracy of these analyses depends on the care taken in obtaining the moduli and strength of the composites. A wealth of published information is available in this field (see e.g., Ref. 2). The accuracy of the analysis of filament-dominated structures depends on the degree to which the filaments actually dominate the response of the structures analyzed.

As methods of obtaining composite material properties improve and as techniques of including effects other than axial filament stiffness and strength enter into filament-dominant analyses, the two methods should coalesce to the point where materials that are marginally in one class or another may be treated by either method. The work reported in this paper broadens the analysis of structures made of filament-dominated materials to include the effect of force transfer between filaments or interfilament forces.

In order to identify the value of accounting for interfilament forces, it is worthwhile to trace the recent development of the analysis of structures in which filament strength and stiffness play dominent roles. This research is almost exclusively confined to axisymmetric membrane or net structures which are subjected to axisymmetric surface and edge loads.

Examination of the equation for membrane stresses in shells of revolution subject to uniform internal pressure, p , reveals one of the major early stimulants to filamentary-structure design. For this loading (see Ref. 3).

$$N_1 = \frac{pr_1}{2} \left(2 - \frac{r_1}{r_2} \right)$$

where N_1 is the circumferential load per inch in the membrane, and r_1 and r_2 are the principal radii of curvature of the surface, as defined in Reference 3. It is apparent that for $r_1/r_2 = 2$ throughout the shell, there is no stress in the circumferential direction. This led to the supposition that the phenomenal strength of thin filamentary materials could be used in engineering applications. For the surface defined by $r_1/r_2 = 2$, filaments positioned on meridional lines would carry the meridional stresses with uniform filament tension and no load-carrying capacity in the circumferential direction would be required except at the edges of the surface.

This concept was applied in the design of parachutes as early as 1923 (Ref. 4), and more recently in the design development of radial cord tires. In 1959, end closures for filament-wound pressure vessels (rocket chambers) were designed (Refs. 5, 14, and 15). In 1960 a "radial cord" toroidal, deployable space-station model was designed (Ref. 16), and 48-inch and 24-foot diameter engineering test models were constructed and subsequently evaluated (Refs. 17, 18, and 19). In 1965 an airlock design for space application was proposed (Ref. 6). In all these applications a membrane is required to contain internal pressure and to introduce the loads into the filaments.

With the exception of the airlock and the toroidal configurations, the disadvantages of filament buildup at the apex of the membrane led to examination of other surface shapes in which uniform tension in filaments placed on non-meridional lines would

contain the internal pressure. The problem was formulated in
Reference 5 for the simple case of two sets of filaments sym-
metrically disposed with respect to meridional lines, and the re-
sulting shapes were determined in Reference 7 for various edge
conditions.

The isotensoid concept, that of placing filaments on sur-
faces of revolution so that design loads are precisely balanced
by axial and uniform stresses in the filaments, was then put on
a firm basis in 1962 with the appearance of Reference 8. In this
reference, the complete theory of pressurized filament-wound
shells was formulated; a systematic study of isotensoid shapes
was made, and the basis for analysis which includes centrifugal
loads caused by rotation was explored. Also, the equations were
developed for nonuniform pressure and multiple-layer shells, and
a wide range of isotensoid structures was described in Reference
20. The isotensoid shapes determined in Reference 8 made pos-
sible the solution of the indirect design problem in some cases.
That is, given a mission objective, if one of the shapes result-
ing from the analysis would perform the mission, the problem was
solved.

The following year, the problem of designing pressurized
rotating net structures was solved and published in Reference 9.
The problem was completely defined and all possible shapes
determined and reported. It was shown that filament tension of
necessity varies in a spinning pressurized net provided that
there is no force transfer between filaments at crossover points.

Concurrent with this work, another approach to the design of
pressure containers was taken and reported in Reference 10.
Here, the direct problem was solved by allowing a continuous dis-
tribution of filament angles or layers of filaments. Using the
results of Reference 10, one can, in principle, specify membrane
geometry, pressure loading, and isotensoid filament stresses and
determine the required distribution of filaments in the membrane.
Practical design considerations dictate the continuous distribu-
tion be replaced by a finite set, thus approximations are
required.

In summary, the principal results of published investiga-
tions into filament-dominated designs can be found in References
8, 9, and 10. Reference 8 identifies the isotensoid shapes pos-
sible for two-family symmetrically wrapped pressurized shells of
revolution and presents solutions for single-layer (two-family)
and multiple-layer (more than two-family) isotensoids. Reference

3

9 identifies shapes for spinning pressurized nets formed by fila-
ments symmetrically disposed on a shell of revolution and pre-
sents solutions for these shapes and equations for filament
tension variation. Reference 10 gives a method of solution and
equations defining the filament wrap pattern for isotensoid de-
signs of pressurized shells of revolution when the shell geometry
is specified.

Throughout the research reviewed above, an artificial design
constraint has been imposed; that is, force transfer between
filaments at filament crossover points is neglected. In nets
this transfer is manifested in knot forces, and in composites it
is manifested in self-equilibrated matrix stresses. In both
cases the interfiber force has the characteristics of shear loads,
and it has been termed interfiber shear or interlaminar shear, etc.
Unfortunately, this terminology carries the connotation of shear
in continuum mechanics and the fundamental nature of the force
transfer between filaments is obscured. For this reason, the
term "interfilament force transfer" will be used throughout this
report.

The design freedom obtained by employing the interfilament
force transfer is exemplified in Reference 11 where the solution
is obtained for an isotensoid spinning filamentary disk. If the
interfilament force-transfer capability is ignored in a spinning
disk, it becomes a degenerate case of the general theory of Ref-
erence 9 for which isotensoid design is impossible. Therefore,
consideration of interfilament force transfer allows isotensoid
(and minimum weight) design where it was not formerly possible.
Also, as will be indicated in the section entitled "Fundamental
Nature of Filamentary Structures", the use of interfilament force
transfer in the design process allows solution of problems where
the shape is prescribed without resorting to continuous distribu-
tions of filaments as was necessary in the approach taken in Ref-
erence 10.

The work reported in this paper introduces the interfilament
force transfer developed in Reference 11 into the general ap-
proach of References 8 and 9. This is done for arbitrary sym-
metric loading of axisymmetric nets formed by two families (or
one layer) of filaments as defined in the section entitled
"Fundamental Nature of Filamentary Structures". It is shown that
isotensoid solutions are possible for many problems in the pres-
ence of·any axisymmetric-surface load-vector field provided the

vector field is confined to meridional planes. Thus pressure, centrifugal force, and axial surface load can be accommodated with isotensoid minimum-weight design.

In the section entitled "Fundamental Nature of Filamentary Structures", the fundamental nature of string structures is discussed qualitatively. The governing equations for two-family nets are derived in the section entitled "Analysis of Single Layer Surfaces". These equations are solved for a number of load and design conditions, and the results are reported and discussed as they are obtained. The problem of determining the filament orientation in the surface and tension variation along filaments when the surface shape is prescribed, is solved. Four illustrative examples are given. Effort is then concentrated on isotensoid design, and the equations are specialized to apply to the case of uniform filament tension. A wide range of load conditions is considered and methods of solution, classification of isotensoid surface shapes, and numerous specific examples are given. A summary of the results is given in the section entitled "Closure", and possible extensions are discussed.

SYMBOLS

a	uniform acceleration in negative z direction
b	parameter defined by Equation (87)
d	parameter defined by Equation (86)
k_i	argument in elliptic integrals defined in Equations (73), (77), (81), and (85)
ℓ	distance measured along filament
$\Delta\ell$	distance measured along a filament between two adjacent filament intersections
m'	mass per unit length of filament
n	total number of filaments in a layer
p	pressure
p_o	pressure at $r = r_o$
r	radial coordinate
r_1, r_2	principal radii of curvature of surface (circumferential and meridional respectively)
r_o	reference radius
r_∞	parameter used in allowing radial coordinate to approach infinity
y	resulting cartesian coordinate when $r_\infty \longrightarrow \infty$ ($r = r_\infty + y$)
z	axial coordinate
A	axial acceleration load parameter (Equation 12)
A,B,C,D	solution types defined by Equation (67)
$\overline{A}$	A/r_o

6

c_i constants

D denominator function (Equation 88)

$E(\psi_i, k_i), E(k_i)$ elliptic integrals of the second kind

$\overline{F}$ vector force field acting on a filament (lb/in)

F_k force at filament intersections (lb)

F_n, F_m, F_c components of $\overline{F}$ in normal, meridional and circumferential directions

$F(\psi_i, k_i)$ elliptic integral of the first kind

G parameter defined by Equation 68

K pressure load parameter (Equation 12)

$K(k_i)$ complete elliptic integral of the first kind

$\overline{L}$ vector surface load (lb/in^2)

L_n, L_m components of $\overline{L}$ in normal and meridional directions (lb/in^2)

N numerator function (Equation 88)

Q function defined by Equation (22)

R $R = r/r_o$

T filament tension

T_o filament tension at $r = r_o$

X $X = R^2 = (r/r_o)^2$

X_2, X_3 roots of Equation (66) given in Equation (67)

$Y(X)$ function defined in Equation (66)

Z $Z = z/r_o$

α angle between meridional tangent and z axis

α_O value of α at $r = r_O$

β angle between filament and meridian

β_O value of β at $r = r_O$

Φ longitudinal coordinate

ψ_i argument in elliptic integrals defined in Equations (72), (76), (80), and (84).

ω angular velocity

Ω spin load parameter (Equation 12)

FUNDAMENTAL NATURE OF FILAMENTARY STRUCTURES

In order to discuss the fundamental nature of filamentary structures, it is necessary to develop clear and concise definitions. In what follows, all discussion is restricted to axisymmetric surfaces and axisymmetric-applied surface and edge loads both of which have no components normal to the meridional planes.

The equation of the surface is expressed in the cylindrical polar coordinates of Figure 1 as

$$z = z(r)$$

$$\text{or} \quad Z = Z(R)$$

where $Z = z/r_o$ and $R = r/r_o$, and r_o is some reference radius. The external load vector field shown in Figure 1

$$\overline{L} = \overline{L}(r)$$

has no component normal to meridional planes and is independent of the longitude, Φ .

With reference to Figure 2, a filament set or family is a collection of filaments which on parallel circles form equal angles, β , with meridional lines on the surface. Within a filament set $\beta = \beta(r)$ as shown in Figure 2a. To each filament set or family at β , there corresponds a complementary set at $-\beta$ as shown in Figure 2b. These two sets together are called a layer (Fig. 2c). It is apparent from the symmetry of the system under consideration that filament sets always appear in complementary pairs forming a layer. In some cases a single filament will belong to both sets in a layer, as shown in Figure 2d. It is apparent that filaments in a set do not intersect except on unique parallel circles where $\beta = \pi/2$, and on these circles, each filament is leaving one set of a layer and entering the complementary set. Filament sets at $\beta \equiv \pi/2$ and $\beta \equiv 0$ are considered to be degenerate layers in which complementary sets each include one half the filaments in the layer, and both sets are the same. Filamentary shells or nets can be designed with one or more

9

layers; the single layer nets will be discussed first.

Single Layer Nets. - Consider a single layer net as shown in Figure 2c and for the moment let the surface load vector be directed normal to the surface formed by the net. Further, assume that the filaments in a set are free to slide relative to the other set in the layer. The net will form an axisymmetric surface shape which depends on the pressure, the inner and outer radii (assuming they are fixed), the length of the filaments, and the total angle, Φ ,traversed by each filament as it is traced from the inner radius to the outer radius. The filaments will be stressed uniformly and will trace out geodesic curves on the surface formed. These facts are established in Reference 8. The net considered is clearly a mechanism which assumes different isotensoid shapes which will depend on how the surface load vector varies.

Now relax the condition that the surface load vector be normal to the surface and allow, for example, centrifugal surface forces. (This simple terminology is used in place of the more exact expression "centrifugal body force per unit area of surface".) The surface shape and the filament paths will change. In fact, the filament geometry in the new surface will be such that the surface-load-vector field can be projected at each point into two components; one in the direction of the principal normal of the filament and the other in the direction of the tangent to the filament. The latter surface force component causes the tension in each filament to vary along its length. These facts are established in Reference 9 and account for the fact that isotensoid design is not possible under the load and net conditions stipulated.

Now assume that at each junction among filaments in separate sets in the layer there is either a knot or a dab of glue. As a consequence, if there is any tendency of the filaments in complementary sets to slide relative to one another, a constraining force will result in the knot or glue and the sliding motion will be arrested. The axisymmetry of the net and the loading do not allow the force transferred from one filament to the other to have a component in the meridional direction of the surface. The interfilament force transfer between filaments in complementary sets of a layer must, therefore, be in the circumferential direction as shown in Figure 3. It is termed F_k . Thus, if there is any tendency for slip to occur between filament sets in a layer, even though the applied load is restricted to lie in meridional planes, each filament will experience a load vector with a

10

component, F_k , out of the meridional plane at each of the inter-sections with fibers from the complementary set. These loads, F_k , are internal and self equilibrating.

Now consider the effect of interfilament force transfer on the two problems discussed above. For the case of surface load-ing normal to the surface, imagine that a pressure has been applied to a system in which sliding can occur and the appropriate isotensoid shape has been assumed. Now imagine that the filaments are either knotted or glued at each intersection. It is clear that the surface, the filament geometry in the surface, and the stress level in the filaments is undisturbed. Consequently, the presence of knots does not increase the number of design parame-ters for the geometry and load considered.

In the second case where the surface-force-vector field is not normal to the surface, filament force transfer can be used to much greater advantage. It has been established (Reference 8) that isotensoid design is not possible in the absence of inter-filament force transfer when the surface load vector is not nor-mal to the surface. Consider now a design where interfilament force transfer exists and non-normal surface load is applied. The possibility exists that the filament geometry (and therefore the filament intersections) and the surface shape can be deter-mined so that the vector sum of external load per filament and the interfilament load has its direction along the principal normal to the filament path in the surface. The resulting net configuration will be isotensoid under the applied loads. Then the use of fila-ment force transfer in the design stage will allow optimum design and minimum weight in single layer nets when the surface load vec-tor field is not normal to the surface. The examination of this problem is the subject of a large part of the remainder of this report.

Multiple Layer Nets. - Consider a system of two layers form-ing an axisymmetric surface and subjected to the type of general symmetric loads defined above. Forces tangent to the surface (in addition to bearing forces) can be transferred between layers, and in addition to the transfer of a part of the tangential com-ponent of the surface load to the inner layer, a self-equilibrated system of loads between layers similar to that between sets may arise. Symmetry considerations restrict the self-equilibrated load system between layers to be directed along meridians of the surface. The load on a filament is then the vector sum of the applied load, a circumferential load due to the self-equilibrated

11

forces between complementary sets, and a meridional load due to the self-equilibrated forces between layers. The possibility then exists that the shape and surface load be specified and the filament paths in both layers determined so that the resultant filament loads are directed along the principal normals of the filaments. Under these conditions, isotensoid design is possible with a finite number of layers even when the geometry is specified. In the absence of interfilament force transfer, this problem has been solved only for normal surface loads, and an infinite number of layers was required (Ref. 10).

A basic difference between single-layer nets and multiple-layer nets has implicitly manifested itself in this section. That is, single-layer nets, even with pinned intersections, are mechanisms and the shape taken by them is strongly load dependent. On the contrary, multiple-layer nets, if knotted or glued, are redundant structures, and fundamentally different design freedom can be achieved.

ANALYSIS OF SINGLE LAYER NETS

Consider equilibrium of a net formed by one layer (Fig. 2c) of complementary sets as defined in the section entitled "Fundamental Nature of Filamentary Structures". The filaments making up the sets are flexible but essentially inextensible. Each intersection between filaments in complementary sets is pinned either by a knot or a dab of glue. The surface load is a vector field with components confined to meridional planes (Fig. 1) and is independent of longitudinal position on the surface.

Let $\overline{F}$ be the load vector per unit length acting on a filament. The components of $\overline{F}$ in the normal and meridional directions of the surface are related to the similarly directed component of surface loading, $\overline{L}$, by

$$F_i = \frac{2\pi r \cos\beta}{n} L_i \tag{1}$$

where β is the filament angle defined in Figure 4, n is the total number of filaments in the surface, and the subscript, i, denotes either the meridional or normal direction.

In order to obtain the component of $\overline{F}$ in the longitudinal direction, assume that filament crossover points or intersections are sufficiently close that the filament transfer force can be averaged between intersections. Then an interfilament force per unit length, F_c, can be defined where $F_c \Delta\ell = F_k$ and $\Delta\ell$ is the distance along a filament between intersections. The total load per unit length of filament is the vector sum of the orthogonal components.

Equilibrium of a surface element is enforced by considering equilibrium of filaments in one set and accounting for the presence of the other set through the filament transfer force, F_c. To this end, consider equilibrium of a filament of length, $d\ell$, (Fig. 4) where along a filament, the following differential relations hold

$$dr = d\ell \, \cos\beta \, \sin\alpha$$

$$d\Phi = d\ell \, r^{-1} \, \sin\beta \qquad\qquad (2)$$

$$dz = -d\ell \, \cos\beta \, \cos\alpha$$

where α is the angle between a meridian on the surface and the z-axis as shown in Figure 4.

With $T = T(r)$ the tensile force in the filament, three independent equilibrium equations can be written; equilibrium of forces parallel to the filament, equilibrium of forces in the z-direction, and equilibrium of torques about the z-axis. These equations read respectively:

$$\left.\begin{array}{l} dT - F_c \, \sin\beta \, d\ell - F_m \, \cos\beta \, d\ell = 0 \\[2mm] d(T \, \cos\beta \, \cos\alpha) - F_n \, \sin\alpha \, d\ell - F_m \, \cos\alpha \, d\ell = 0 \\[2mm] d(rT \, \sin\beta) - F_c r \, d\ell = 0 \end{array}\right\} \qquad (3)$$

Equation 2 can be used to eliminate $d\ell$ from Equation (3). With r chosen as the independent variable, Equations (3) then read:

$$\frac{dT}{dr} - F_c \, \tan\beta \, \csc\alpha - F_m \, \csc\alpha = 0 \qquad\qquad (4)$$

$$\frac{d(T \, \cos\beta \, \cos\alpha)}{dr} - F_n \, \sec\beta - F_m \, \sec\beta \, \operatorname{ctn}\alpha = 0 \qquad\qquad (5)$$

$$\frac{d(rT \, \sin\beta)}{dr} - F_c r \, \sec\beta \, \csc\alpha = 0 \qquad\qquad (6)$$

This system of first-order differential equations governs the design and analysis of single-layer nets. The functions, $\beta(r)$ and $\alpha(r)$, can be thought of as the intrinsic coordinates

14

of the filament paths on the surface and the surface shape, respectively. They are related to the more practical design functions, $\Phi(r)$ and $z(r)$, by two first-order differential equations obtained by eliminating $d\ell$ from Equation (2).

$$\frac{d\Phi}{dr} = r^{-1} \tan\beta \csc\alpha \tag{7}$$

$$\frac{dz}{dr} = - \operatorname{ctn}\alpha \tag{8}$$

Equations (4) through (8) have been examined in detail for the special case of combined pressure and centrifugal loading with no force transfer between filaments $(F_c = 0)$ in Reference 9, and for pressure loading $(F_m = F_c = 0)$ in Reference 8 where an arbitrary number of layers was considered. In neither case could the shape be prescribed. As pointed out in the section entitled "Fundamental Nature of Filamentary Structures", force transfer between filaments in separate sets of a layer allows specification of the surface shape provided filament tension may vary along a filament. This extends the design freedom in problems of the type treated in Reference 9. Further, the inclusion of filament force transfer allows isotensoid design when the surface load vector is not normal to the surface. Thus, the results of Reference 8 can be extended to determine isotensoid shapes for arbitrary symmetric surface loading.

Two distinct classes of problems are thus identified for single layer nets:

(1) The shape and surface load are prescribed and the filament tension, $T(r)$, and the filament geometry, $\Phi(r)$, are to be determined.

(2) The surface load and uniform filament tension are prescribed and the surface shape, $z(r)$, and the filament geometry, $\Phi(r)$, are to be determined.

Both of these problems are treated below. Under certain conditions a third type of problem, not considered here, must be addressed. If the interfilament forces become excessive, failure can occur between sets in a bonded design or in knots in a knotted

15

design. Therefore, in any design application, an allowable must be established for F_c and care taken that it is not exceeded.

Before solutions for the two problem types can be developed, the explicit dependence of F_m and F_n on the independent variable, r , must be stipulated. Three specific load cases are considered; surface pressure, p , centrifugal surface load caused by angular rotation, ω , about the axis of symmetry, and a d'Alembert surface load in the positive g-direction caused by a uniform acceleration, "a" , in the negative z-direction.

For pressure, $p(r)$

$$\left.\begin{aligned} F_n &= \frac{2\pi r}{n} \cos\beta \; p(r) \\[3em] F_m &= 0 \end{aligned}\right\} \tag{9}$$

For radial acceleration caused by spin velocity, ω

$$\left.\begin{aligned} F_n &= m'\omega^2 r \cos\alpha \\[3em] F_m &= -\,m'\,\omega^2 r \sin\alpha \end{aligned}\right\} \tag{10}$$

For axial acceleration, "a" , in the negative, z-direction

$$\left.\begin{aligned} F_n &= m'a \sin\alpha \\[3em] F_m &= m'a \cos\alpha \end{aligned}\right\} \tag{11}$$

where m' is the filament mass per unit length. Note that the presence of a dense fluid contained within the surface and under-going acceleration and rotation may be accounted for through the pressure, $p(r)$. It is advantageous at this point to nondimensionalize the equations. Let T_o and p_o be the filament tension and pressure load at some reference radius, r_o , and let the following dimensionless quantities be defined

16

Pressure parameter $\qquad\qquad K = \dfrac{2\pi r_o^2}{nT_o}\, p_o$

Spin parameter $\qquad\qquad\qquad \Omega = \dfrac{m'\omega^2 r_o^2}{T_o}$

$\left.\phantom{\begin{array}{c}1\\1\\1\\1\\1\\1\\1\end{array}}\right\}$ (12)

Axial acceleration parameter $\quad A = \dfrac{m' a r_o}{T_o}$

Radial coordinate $\qquad\qquad R = r/r_o$

The filament loads per unit length, F_m and F_n , are convenient-ly expressed by use of the definitions (12) and summing Equations (9) through (11).

$$F_m = \frac{T_o}{r_o}\,(-\Omega\, R\, \sin\alpha + A\, \cos\alpha)$$

$$F_n = \frac{T_o}{r_o}\,(KR\, p/p_o\, \cos\beta + \Omega\, R\, \cos\alpha + A\, \sin\alpha)$$

$\left.\phantom{\begin{array}{c}1\\1\\1\\1\\1\end{array}}\right\}$ (13)

Equation (13) for F_m and F_n can be used in Equations (4) through (6) to obtain the nondimensional governing equations for single-layer surfaces of revolution loaded by internal pressure, axial acceleration, and spin.

$$\frac{d(T/T_o)}{dR} - \frac{F_c\, r_o}{T_o}\,\tan\beta\,\csc\alpha + \Omega\, R - A\,\text{ctn}\,\alpha = 0 \qquad (14)$$

$$\frac{d(\cos\beta\,\cos\alpha\,T/T_o)}{dR} - KR\, p/p_o - A\,\sec\beta\,\csc\alpha = 0 \qquad (15)$$

17

$$\frac{d \ (R \ \sin\beta \ T/T_o)}{dR} - \left(\frac{F_c \ r_o}{T_o}\right) R \ \sec\beta \ \csc\alpha = 0 \qquad (16)$$

For convenience, Equations (7) and (8), which are the differential relations among the intrinsic coordinates (β and α), and the more practical design functions (z and Φ), are recorded in nondimensional form. Let $z/r_o = Z$ in Equations (7) and (8), then

$$\frac{d\Phi}{dR} = R^{-1} \ \tan\beta \ \csc\alpha \qquad (17)$$

$$\frac{dZ}{dR} = - \ \text{ctn}\alpha \qquad (18)$$

The remainder of this work is devoted to the solution of these governing equations for two types of problems:

(1) Surface shape and loading prescribed, filament tension and filament angle to be determined, and

(2) Uniform tension and loading prescribed and surface shape to be determined.

In problems of the first type, it is possible to apply edge boundary conditions on loads by use of either Equation (23) or (35) below. However, it is more convenient in the problems treated to specify the filament angle at the edge and determine the edge filament loads parametrically in terms of the specified angle. In problems of the second type, the shape and edge position are unknown at the outset, consequently it is convenient again to use the filament angle β_o at $R = 1$ as a boundary condition and to determine the shapes with β_o as a parameter. The shapes thus determined may terminate at edges where $\beta \neq \pi/2$. Then, with the shape and filament angle known at the edge, the edge load conditions necessary to support the filament loads may then be determined.

The Direct Problem – Shape Prescribed

Barring the exceptional case when the prescribed shape is

an isotensoid shape for the loads applied, the tension in the filaments of a single layer surface will be functions of r. With the loads (K, A, Ω) and shape (α) prescribed, Equations (14), (15), and (16) must be used to determine the unknown functions, $F_c(r)$, $\beta(r)$, and $T(r)$. The function, $F_c(r)$, is easily eliminated from Equations (14) and (16), leaving two governing equations

$$\sin\beta \; \frac{d(R \sin\beta \; T/T_o)}{dR} = R \; \frac{d(T/T_o)}{dR} + \Omega \; R^2 - AR \; \text{ctn}\alpha \qquad (19)$$

$$\frac{d(\cos\beta \; \cos\alpha \; T/T_o)}{dR} = KR \; p/p_o + A \; \sec\beta \; \csc\alpha \qquad (20)$$

For $A \neq 0$, the appearance of β in the last term in Equation (2) precludes its solution by simple integration. The two cases, $A = 0$ and $A \neq 0$, are therefore treated separately.

Solution When $A = 0$. - For $A = 0$, solutions when they exist can be expressed analytically. Equation (20) can be integrated

$$\left(\frac{T}{T_o}\right) \cos\beta = K \sec\alpha \int p/p_o \; RdR$$

As boundary condition, set $\beta = \beta_o$ and $\sin\beta_o = C$ at $R = 1$ and for convenience, define the new independent variable, $X = R^2$. Then

$$\left(\frac{T}{T_o}\right) \cos\beta = \sec\alpha \left\{ \sqrt{1 - C^2} \; \cos\alpha_o - \frac{K}{2} \int_X^1 \left(\frac{p}{p_o}\right) dX \right\} \qquad (21)$$

The right side of Equation (21) is a known function of the independent variable, $X = R^2 = (r/r_o)^2$, which depends on the shape and prescribed pressure load. Let it equal $Q(X)$. Then

$$Q(X) = \left\{ \sqrt{1 - C^2} \cos\alpha_o - \frac{K}{2} \int_X^1 (p/p_o) \; dX \right\} \sec\alpha \qquad (22)$$

and Equation (21) reads

$$\frac{T}{T_o} = Q \sec\beta \qquad (23)$$

Equation (23) can be used to eliminate T/T_o from Equation (19) when $A = 0$ with the result

$$\sin\beta \frac{d}{dR} [R \; Q \; \tan\beta] = R \frac{d}{dR} [Q \; \sec\beta] + \Omega \; R^2$$

If this expression is multiplied by $Q \sec\beta$ and the change to independent variable, X, completed, the following expression results

$$\frac{d}{dX} [X \; Q^2 \; \tan^2\beta] = X \frac{d}{dX} [Q^2 \; \sec^2\beta] + \Omega \; X \; Q \; \sec\beta \qquad (24)$$

Use of the identity $\tan^2\beta = \sec^2\beta - 1$ in (24) and recognition that

$$\frac{d}{dX} [X \; Q^2 \; \sec^2\beta] = X \frac{d}{dX} [Q^2 \; \sec^2\beta] + Q^2 \; \sec^2\beta$$

results in the following quadratic equation for $\sec\beta$

$$Q^2 \; \sec^2\beta - \Omega \; X \; Q \; \sec\beta - \frac{d}{dX} [X \; Q^2] = 0 \qquad (25)$$

from which,

$$\sec\beta = \frac{1}{2Q} \left\{ \Omega X \pm \sqrt{\Omega^2 X^2 + 4 \frac{d}{dX} [X Q^2]} \right\} \qquad (26)$$

The sign in (26) is chosen so that $\sec\beta > 1$. With this result for the filament geometry, the tension is given by Equation (23).

$$\frac{T}{T_O} = \frac{1}{2} \left\{ \Omega X \pm \sqrt{\Omega^2 X^2 + 4 \frac{d}{dX} [X Q^2]} \right\} \qquad (27.)$$

where the sign is chosen as for $\sec\beta$. The interfilament force can now be computed directly from Equation (16). The filament path in terms of the polar coordinates is determined by integration of Equation (17) for β given by Equation (26).

From these results it is apparent that not all the parameters can be chosen independently. For example, if Equation (25) is evaluated at $X = 1$, the following condition results

$$\Omega = 1 - \left\{ \frac{d}{dX} [X Q^2] \right\}_{(X = 1)} \qquad (28)$$

To obtain Equation (28), note that $Q(1)$ was determined from Equation (22) as

$$Q(1) = \sqrt{1 - c^2} = \cos\beta_O \qquad (29)$$

Equation (28) may be regarded as a relation between β_O and T_O for geometry, load, and all other parameters fixed. Thus with either T_O or β_O specified at $r = r_O$, Equations (26) and (27) determine the unique solution for tension and filament path in the specified surface subjected to the specified loads.

The minimum (maximum) radius to which the solution extends on the specified shape occurs at $\beta = \pi/2$ or $\beta = 0$. For the filament tension to remain finite, when $\beta = \pi/2$, Equation (23) requires that

21

$$Q(X_{max}) = 0 \tag{30}$$

For this condition Equation (22) determines X_{max} (or X_{min})

$$\int_{X_{max}}^{1} (p/p_o) \, dX = \frac{2}{K} \sqrt{1 - c^2} \cos\alpha_o \tag{31}$$

Equation (31) defines the minimum radius for internal pressure $(K > 0)$ and the maximum radius for external pressure $(K < 0)$.

Finally, if the filaments become tangent to the meridians, the solution ends. In this case $\beta = 0$ and Equation (25) requires that

$$\frac{dQ}{dX} = -\frac{\Omega}{2} \text{ for } \beta = 0 \tag{32}$$

Three examples are given to illustrate the solution method.

Example 1 - Spherical Pressure Vessel. - $\Omega = 0$, $p = p_o$
The shape of the sphere is defined by

$$\cos\alpha = R = \sqrt{X}$$

Hence

$$Q(X) = \left\{ \sqrt{1 - c^2} - \frac{K}{2} (1 - X) \right\} X^{-\frac{1}{2}}$$

and

$$\frac{d}{dX} [X Q^2] = K \left\{ \sqrt{1 - c^2} - \frac{K}{2} (1 - X) \right\}$$

With this result, the boundary condition, Equation (28), gives

22

$$K = \frac{1}{\sqrt{1 - c^2}} = \sec\beta_o$$

which with the definition of K in Equation (12) determines the tension, T_o, as a function of the pressure, p, the reference radius, r_o, the number of filaments, n, and the filament angle, β_o, at the reference radius. From Equation (31), the minimum radius to which the filaments extend is given by

$$R^2_{min} = X_{min} = 2c^2 - 1$$

where the reference radius is chosen such that $\alpha_o = 0$. Also, from Equation (32), the filament becomes tangent to the meridian plane for

$$X_{min} = 1 - 2c^2$$

Thus for $c^2 < 1/2$, the filament forms a cusp, while for $c^2 > 1/2$ a smooth loop is formed. For the special case $\beta_o = 45^o$ ($c^2 = 1/2$), the complete sphere is covered with filaments overlapping severely at the poles. The filament curve is obtained from Equation (26)

$$\sec\beta = \frac{\sqrt{KX\left\{\sqrt{1 - c^2} - \frac{K}{2}(1 - X)\right\}}}{\sqrt{1 - c^2} - \frac{K}{2}(1 - X)} = \sqrt{\frac{2R^2}{R^2 - (2c^2 - 1)}}$$

and the tension in the filaments by

$$\frac{T}{T_o} = \sqrt{1 - \frac{1 - R^2}{2(1 - c^2)}}$$

23

Note that T vanishes for $R^2 = 2C^2 - 1$, which corresponds to the minimum radius determined above when $C^2 > 1/2$. For the three distinct cases $C^2 < 1/2$, $C^2 = 1/2$, $C^2 > 1/2$, the filament angle, β, and the tension, T/T_O, are plotted versus the radial coordinate, R, in Figure 5. Corresponding sketches of the net are also shown in Figure 5.

Example 2 - Spinning Cone With Uniform External Pressure. - Take p to be the uniform surface pressure on the outside of the cone $(p < 0)$. Then $p/p_O = 1$, $\alpha = \alpha_O$, and $K < 0$.

Hence from Equation (22)

$$Q(X) = \sqrt{1 - C^2} - \frac{K}{2}(1 - X)\sec\alpha$$

The boundary condition on Ω is obtained immediately from Equation (28)

$$\Omega = C^2 - K \sec\alpha \sqrt{1 - C^2}$$

The special case of radial filaments emanating as linear rays from the apex along the cone is given by $C = 0$. Then

$$\Omega = - K \sec\alpha$$

For this case, each filament is in equilibrium with only pressure and inertia loading, the interfilament forces vanishing. For $C \neq 0$, the maximum radius is given by Equation (31) and K can be eliminated by the use of Equation (28)

$$R^2_{max} = X_{max} = 1 - \frac{2}{K}\sqrt{1 - C^2}\cos\alpha = 1 + \frac{2(1 - C^2)}{\Omega - C^2}$$

The condition that the filaments be tangent to the meridian plane is given by Equation (32) and merely reproduces the condition for radial filaments given above: $\Omega = - K \sec\alpha$. The filament

24

geometry and tension are obtained by substituting the expression given above for $Q(X)$ into Equations (26) and (27).

$$\sec\beta =$$

$$\frac{\Omega X + [\Omega^2 X^2 + 4(1-C^2) - 4\sqrt{1-C^2}\ K\sec\alpha\,(1-2X) + K^2\sec^2\alpha\,(1-4X + 3X^2)]^{\frac{1}{2}}}{2\sqrt{1-C^2} - K\sec\alpha\,(1-X)}$$

$$\frac{T}{T_O} =$$

$$\frac{\Omega X}{2} \pm \frac{1}{2}\,[\Omega^2 X^2 + 4(1-C^2) - 4\sqrt{1-C^2}\ K\sec\alpha\,(1-2X) + K^2\sec^2\alpha\,(1-4X + 3X^2)]^{\frac{1}{2}}$$

These results are shown on Figure 6 for particular values of C, α, and K. For the parameters chosen, T/T_O is maximum at $X = X_{max}$. Because $\beta = \pi/2$ at $X = X_{max}$, there is no edge load at the aft end of the cone, however, there is a concentrated load at the apex, D, given by

$$D = n\,T\,\cos\alpha$$

where n is the total number of filaments.

Example 3 - Spinning Paraboloid. - $\Omega \neq 0$, $K = 0$. The meridional curve for a paraboloid with aperture-to-focal-length ratio of 2 is

$$Z = -R^2/4$$

By Equations (22) and (28), the angular velocity parameter, Ω, is related to the boundary condition on β at the outer edge of the surface

$$\Omega = 1 - \cos^2\beta_O\,\cos^2\alpha_O = \frac{4 + C^2}{5}$$

25

where $C = \sin\beta_O$, and the value of $\cos^2\alpha_O = 1/5$ is obtained from the equation of the meridian and simple differential geometry. The filament tension and geometry in the surface are easily obtained from Equations (27) and (26) respectively.

$$\frac{T}{T_O} = \frac{1}{2} \left\{ X \frac{4 + C^2}{5} + \sqrt{X^2 \left(\frac{4 + C^2}{5}\right)^2 + \frac{4}{5} (1 - C^2)} \right\}$$

$$\cos\beta = \frac{2 \sqrt{1 - C^2} \left(\frac{4}{5X} + \frac{1}{5}\right)^{\frac{1}{2}}}{X \left(\frac{4 + C^2}{5}\right) + \sqrt{X^2 \left(\frac{4 + C^2}{5}\right) + \frac{4}{5} (1 - C^2)}}$$

These results are shown on Figure 7 where both T/T_O and β are plotted versus R with the square of the sine of the filament angle at the outer edge, β_O , as a parameter. The minimum radius to which the surface is covered decreases to zero as β_O approaches $\pi/2$. At this limit, however, the solution is a family of disconnected parallel circles.

Except for the limit case of $\beta_O = \pi/2$, tensile forces exist at both the inner and outer edges of the surface. These forces are obtained from the relation between Ω and β_O above and the definition of Ω in Equation (12).

$$\Omega = \frac{m' \omega^2 r_O{}^2}{T_O} = \frac{4 + C^2}{5}$$

Thus

$$T_O = \frac{5 \, m' \omega^2 r_O{}^2}{4 + \sin^2\beta_O}$$

This is the tension in the filaments at $R = 1$ or $r = r_O$, the outer radius of the paraboloid. The edge load at the inner edge is obtained from Figure 7 and the value of T_O above.

<u>Solution When $A \neq 0$</u>. – For the general loading conditions $A \neq 0$, $\Omega \neq 0$, $K \neq 0$, Equations (19) and (20) can be reduced to one algebraic equation and one differential equation. With minor modification, Equations (19) and (20) can be written as

$$\frac{d(T/T_O \sin\beta)^2}{dR} = \frac{d(T/T_O)^2}{dR} + 2\Omega\, T/T_O\, R - 2A\, T/T_O\, \operatorname{ctn}\alpha - \frac{2}{R}\, (T/T_O\, \sin\beta)^2$$

$$\frac{d(T/T_O \cos\beta)^2}{dR} = \frac{2\, T/T_O\, R\, K\, \cos\beta}{\cos\alpha} + \frac{2\, T/T_O\, A}{\sin\alpha\, \cos\alpha} - \frac{2\,(T/T_O\, \cos\beta)^2}{\cos\alpha}\, \frac{d(\cos\alpha)}{dR}$$

If these expressions are added together, the terms involving derivatives of T/T_O drop out and the resulting expression may be solved for T/T_O. Thus,

$$\frac{T}{T_O} = \frac{\Omega R^2 + \dfrac{K\, R^2\, \cos\beta}{\cos\alpha} + A\, R\, \tan\alpha}{\sin^2\beta + \dfrac{\cos^2\beta}{\cos\alpha}\, R\, \dfrac{d(\cos\alpha)}{dR}} \tag{33}$$

Equation (33) in conjunction with either of Equations (19) and (20) or some combination thereof may be used to numerically determine the filament tension, T/T_O, and the filament angle, β, for the given geometry and load conditions.

<u>Example 4 – Gravity Loaded Paraboloid</u>. – $A \neq 0$, $\Omega = K = 0$ As a simple example solution when $A \neq 0$, consider a paraboloid supported at its outer edge in a gravitational or other acceleration field. The meridional curve is again as in Example 3

$$Z = -\frac{R^2}{4}$$

Equation (33) with $\Omega = K = 0$ reads

$$\frac{T}{T_o} = \frac{AR \tan\alpha}{\sin^2\beta + \dfrac{\cos^2\beta}{\cos\alpha} R \dfrac{d(\cos\alpha)}{dR}}$$

which for the paraboloidal geometry may be written

$$\frac{T}{T_o} = \frac{2A (4 + R^2)}{4 + R^2 \sin^2\beta}$$

The second equation used is obtained by eliminating A between Equations (19) and (20) and then carrying out the indicated differentations and solving for $d\beta/dR$.

$$\frac{d\beta}{dR} =$$

$$\frac{4R^2 \cos\beta (4 \csc\beta - 8 \sin\beta - R^2 \sin\beta) - (4 + R^2)^2 (4 + R^2 \sin^2\beta) \tan\beta}{4R [R^2 (1 + \cos^2\beta) + 4] (4 + R^2)}$$

A digital computer program was written and used to determine T/T_o and β from these two governing equations. The initial condition, β_o at $R = 1$, determines the minimum radius to which the solution extends. Thus by trial and error, the value of β_o for which the paraboloid is completely covered may be determined. For a value of $\beta_o = 15.7172^o$, the solution extends to $R <$ 0.003 . For values of $\beta_o < 15.7172^o$, $\beta = 0$ at the minimum radius to which the solution extends, thus, a force is required at the inner edge. For $\beta_o > 15.7172^o$, $\beta = \pi/2$ at the inner edge, thus, the filaments end only at the outer edge and no force is required at the inner edge.

The tension variation, $T/(T_o A)$, and filament angle β are plotted versus radial position, R ,for $\beta_o = 15.7172^o$ on Figure 8. Note that $T/(T_o A)$ is maximum at the outer radius $R = 1$ and by use of the definition of A (Equation 12) and Figure 8

$$\frac{T_{max}}{m'ar_o} = 2.455$$

This equation can be used to determine the maximum size paraboloid that can be made in terms of the filament density and maximum stress. In engineering terminology

$$\frac{\sigma_{max}}{\rho \; n \; 2.455} = r_{o_{max}}$$

where ρ is the weight density, n is the number of g's acceleration and σ/ρ is termed the specific strength.

The Indirect Problem - Isotensoid Design

Return now to the governing Equations (14) through (18) and stipulate that the filament tension be uniform. Then $T/T_o = 1$ and Equation (14) yields an explicit expression for the inter-filament force

$$\left(\frac{F_c \; r_o}{T_o}\right) = \Omega \; R \; \text{ctn}\beta \; \sin\alpha - A \; \text{ctn}\beta \; \cos\alpha \qquad (34)$$

Equation (34) can be used to eliminate F_c from Equation (16) and for $T/T_o = 1$, Equation (15) and (16) read

$$\frac{d(\cos\beta \; \cos\alpha)}{dR} = KR \; p/p_o + A \; \sec\beta \; \csc\alpha \qquad (35)$$

$$\frac{d(R \; \sin\beta)}{dR} = \Omega \; R^2 \; \csc\beta - AR \; \text{ctn}\alpha \; \csc\beta \qquad (36)$$

A convenient form for these equations is obtained by multiplying Equation (35) by $\cos\beta \; \cos\alpha$ and Equation (36) by $R \; \sin\beta$. Then

29

$$\frac{d(\cos^2\beta \ \cos^2\alpha)}{dR} = 2\,(K\ R\ p/p_O\ \cos\beta\ \cos\alpha\ +\ A\ \text{ctn}\alpha) \tag{37}$$

$$\frac{d(R^2\ \sin^2\beta)}{dR} = 2\ (\Omega\ R^3\ -\ A\ R^2\ \text{ctn}\alpha) \tag{38}$$

As with the direct problem, the presence of $A \neq 0$ complicates the integration of Equations (37) and (38). As a consequence, when $A \neq 0$, numerical integration has been employed in their solution. Expressions for $d\alpha/dR$ and $d\beta/dR$ suitable for numerical integration are readily obtained from Equations (37) and (38) by carrying out the indicated differentiation. There results

$$\frac{d\alpha}{dR} =$$

$$- K\ p/p_O R\ \csc\alpha\ \sec\beta\ -\ \Omega\ R\ \text{ctn}\alpha\ \sec^2\beta\ -\ A\ \sec^2\beta\ +\ \tan^2\beta\ \text{ctn}\alpha R^{-1} \tag{39}$$

$$\frac{d\beta}{dR} = \Omega\ R\ \csc\beta\ \sec\beta\ -\ A\ \text{ctn}\alpha\ \csc\beta\ \sec\beta\ -\ \tan\beta R^{-1} \tag{40}$$

and from Equation (18)

$$\frac{dZ}{dR} = -\ \text{ctn}\alpha$$

It is clear that as α approaches zero, Equation (18) becomes unsuitable for numerical integration. This is remedied by changing independent variables from R to Z. Then Equations (39), (40), and (18) read

$$\frac{d\alpha}{dZ} = K\ p/p_O\ R\ \sec\alpha\ \sec\beta\ +\ \Omega\ R\ \sec^2\beta\ +\ A\ \tan\beta\ \sec^2\beta\ -\ \tan^2\beta R^{-1} \tag{41}$$

$$\frac{d\beta}{dZ} = -\Omega R \tan\alpha \csc\beta \sec\beta + A \csc\beta \sec\beta + \tan\beta \tan\alpha R^{-1} \qquad (42)$$

$$\frac{dR}{dZ} = - \tan\alpha \qquad (43)$$

Integration of Governing Equations

Solutions to the governing equations are given below in order of increasing complexity, starting with cases where only one load parameter is nonzero and moving on to all load parameters nonzero. The following cases are considered:

Case 1 $K \neq 0$ $\Omega = 0$ $A = 0$

Case 2 $K = 0$ $\Omega \neq 0$ $A = 0$

Case 3 $K = 0$ $\Omega = 0$ $A \neq 0$

Case 4 $K \neq 0$ $\Omega > 0$ $A = 0$

Case 5 $K \neq 0$ $\Omega > 0$ $A \neq 0$

Case 1 – $K \neq 0$. – Pressure load. This case is treated extensively in Reference 8.

Case 2 – $\Omega \neq 0$. – Load due to spin. For this case, Equations (37) and (38) read

(a) $$\frac{d(\cos\beta \cos\alpha)}{dR} = 0$$

(b) $$\frac{d(R^2 \sin^2\beta)}{dR} = 2 \Omega R^3$$

Using the previous notation for fiber angle at the reference radius

31

$$\sin\beta_{(R=1)} = C$$

where

$$\alpha_{(R=1)} = 0$$

and using an auxiliary parameter

$$B = \frac{2C^2}{\Omega}$$

expressions (a) and (b) can be readily integrated, yielding

(c) $$\cos\beta \, \cos\alpha = \sqrt{1-C^2}$$

(d) $$\sin\beta = \frac{1}{R}\sqrt{\frac{\Omega}{2}\left[R^4 + (B-1)\right]}$$

Substituting (d) into (c) yields an expression for the meridian angle

(e) $$\cos\alpha = \sqrt{\frac{1-C^2}{1 - \frac{\Omega}{2}\left[R^2 + (B-1)\frac{1}{R^2}\right]}}$$

and, using Equation (18)

(f) $$\frac{dZ}{dR} = -\cot\alpha = \mp R\sqrt{\frac{2(1-C^2)}{\Omega\left[-R^4 + B(R^2-1) + 1\right]}}$$

Expression (f) can be integrated as

32

$$(g) \qquad Z = \pm \sqrt{\frac{1-C^2}{2\Omega}} \int \frac{d(R^2)}{\sqrt{(1-R^2)\,(R^2-B+1)}}$$

Other quantities of interest are the fiber azimuth, from Equation (7) and from expressions (c) and (d) above:

$$(h) \qquad \frac{d\Phi}{dR} = \frac{1}{R} \frac{\sin\beta}{\cos\beta\,\sin\alpha} = \frac{1}{R} \sqrt{\frac{R^4 + (B-1)}{(1-R^2)\,(R^2-B+1)}}$$

The nondimensional fiber length $dL = d\ell/ro$ from Equation (2) and (d) becomes

$$(i) \qquad \frac{dL}{d\Phi} = \frac{R}{\sin\beta} = \frac{R^2}{\sqrt{\frac{\Omega}{2}\,[R^4+B-1]}}$$

or, with Z as a variable

$$(j) \qquad \frac{dL}{dZ} = \frac{1}{\cos\beta\,\cos\alpha} = \frac{1}{\sqrt{1-C^2}} = \csc\beta_{(R=1)}$$

Expression (c) permits the calculation of fiber lengths between fiber intersections, defining the metric properties of the two-family fiber net. Expression (j) shows the fiber length increment in the axial direction to be dependent only on the parameter, C, (i.e. the fiber angle at the equator $R = 1$) and therefore relates the fiber length (and consequently the structural mass) directly to the axial distance between poles of the spinning structure. Hence, with the boundary condition $Z_{(R=1)} = 0$

$$(k) \qquad L = \frac{Z}{\sqrt{1-C^2}}$$

An examination of (g) and (d) reveals the existence of real solutions for either positive or negative values of Ω. Using the boundary conditions $Z = 0$ at $R = 1$, (g) becomes for positive values of Ω

$$Z = \frac{1}{2} \sqrt{\frac{2}{\Omega}(1-C^2)} \left[\left(\sin^{-1}\frac{B-2R^2}{B-2}\right) - \frac{\pi}{2}\right] \qquad (44a)$$

or

$$Z = \sqrt{\frac{2}{\Omega}(1-C^2)} \ \tan^{-1}\sqrt{\frac{R^2-1}{B-1-R^2}} \qquad (44b)$$

And for negative values of Ω

$$Z = \sqrt{\frac{2}{\Omega}(C^2-1)} \ \ln\left|\frac{\sqrt{R^2-1}+\sqrt{R^2+1-B}}{\sqrt{2-B}}\right| \qquad (44c)$$

or

$$Z = \sqrt{\frac{2}{\Omega}(C^2-1)} \ \tanh^{-1}\sqrt{\frac{R^2-1}{R^2+(1-B)}} \qquad (44d)$$

Meridional shapes and fiber patterns are shown in Figures 9 and 10, respectively. They can be described as follows:

1. For $0 < C^2 < \frac{\Omega}{2}$ (or $0 < B < 1$), the structure forms a barrel open at both ends, symmetrical to the equatorial mid-plane at $R = 1$ with the fibers terminating at the barrel ends at a radius $R = \sqrt[4]{1-B}$ and in directions tangential to the meridian.

2. For $C^2 = \frac{\Omega}{2}$ (or $B=1$), the meridian of the structure will intersect the Z-axis twice, with a slope, approached in the

limit by $\cos \alpha_{(R=0)} = \pm \sqrt{1-c^2} = \sin \beta_{(R=1)}$, and the axial distance between the two intersections is in nondimensional notation

$$(2Z_{R=0}) = \pi \sqrt{\frac{2}{\Omega}\left(1-c^2\right)}$$

The structure is that of a spindle, symmetrical with respect to an equatorial plane, pointed at two ends, covered by fibers that form a maximum angle, β_o , at the equator and with the fiber angle declining to zero at the two apexes. This structure has the additional interesting property that the distances between fiber intersections are all equal and given by

$$\Delta L = \frac{\Delta \ell}{r_o} = \frac{\pi}{n} \sqrt{\frac{2}{\Omega}}$$

This is seen readily from Expression (i) by letting $B = 1$ and and $\Delta \Phi = \frac{\pi}{n}$. The fiber pattern, projected into the equatorial plane assumes the form of circles with radius $\rho = \frac{r_o}{2}$ tangent to the periphery, $R=1$, and intersecting the center (see Fig. 11).

3. For $\frac{\Omega}{2} < c^2 < \Omega$ (or $1 < B < 2$), the structure describes a periodically "corrugated" tube of radius range $1 \geq R \geq \sqrt{B-1}$ indefinitely extended along the Z-axis. The fiber angle, β , is at a maximum at both radial extremes. The axial distance between two extremes is, in nondimensional notation

$$2Z_{(R=R_{min})} = \pi \sqrt{\frac{2}{\Omega}} (1-c^2)$$

4. For $c^2 = \Omega$, or $(B=2)$, Equation (44) yields an indefinite value, real only for $R=1$. The corresponding structure is a right circular cylinder of radius, R , covered by fibers forming helices of constant pitch.

5. For $C^2 > \Omega$ or $(B > 2)$, the structure is geometrically similar to that described in (3), but the radius range is restricted to $\sqrt{(B-1)} > R > 1$. It can be readily shown that the two types of solutions differ only by a geometrical scale factor of $\sqrt{(B-1)}$.

6. For $C=1$, a special case obtains: (h) yields $Z = 0$ for $R \leq 1$. The structure is that of a flat annular disk originally discovered by Kyser (Ref. 11).

7. For $\Omega < 0$ ($B < 0$ since $2C^2$ is positive definite) real solutions for the surface exist only for $R \geq 1$ and real solutions for the filament paths exist only for $R \leq \sqrt[4]{1-B}$. Thus for $\Omega < 0$ ($B<0$), solutions exist in the range $1 \leq R \leq \sqrt[4]{1-B}$. The structure is formed by inward arches tangent to the cylinder $R=1$. At the outer perimeter, the fibers become parallel to the meridian, i.e., fiber angle β becomes zero. The slope angle of a meridian in the surface at the outer periphery is equal to the fiber angle at $R=1$, i.e., $\alpha_{R=R_{max}} = \beta_0 = \beta_{R=1}$.

Case 3 – $A \neq 0 \quad \Omega = K = 0$. – Uniform acceleration in negative Z-direction. For this case, Equations (37), (38), and (18) read:

(1)
$$\frac{d(\cos^2\beta \, \cos^2\alpha)}{dR} = 2A \, \text{ctn}\alpha$$

$$\frac{d(R^2 \sin^2\beta)}{dR} = -2A \, R^2 \, \text{ctn}\alpha$$

(m)
$$\frac{dZ}{dR} = - \, \text{ctn}\alpha$$

Eliminating $\text{ctn}\alpha$ from (1) by use of (m) and integrating

$$\cos^2\beta \, \cos2\alpha = - \, 2AZ + C_3 \tag{45}$$

where C_3 is an integration constant. Note that the right side of Equation (45) is confined to the interval $(0, 1)$. Equation

36

(45) allows the determination of the shape, $Z(R)$, once α and β are known. These functions are most conveniently determined numerically using Equations (39) and (40) which for $\Omega = K = 0$ read

(n) $$\frac{d\alpha}{dR} = - A \sec^2\beta + \tan^2\beta \ \text{ctn}\alpha \ R^{-1}$$

(o) $$\frac{d\beta}{dR} = - A \ \text{ctn}\alpha \ \csc\beta \ \sec\beta - \tan\beta \ R^{-1}$$

The shape $Z(R)$ is determined by Equation (45). These Equations have been numerically integrated and the resulting shapes $Z(R)$ are shown on Figures 11 for various ranges of α_o , β_o , r_o , and A .

The meridional shapes shown in Figures 11 terminate at both peripheral edges when β , the filament angle, goes to zero. The direction and magnitude of the edge loads required to support these surfaces is determined by the surface angle, α , at the periphery, the number of filaments, and the filament load. Recalling the definition of the axial load parameter (Eq. 12), A is the product of the reference radius and the ratio of surface load, $m'a$, to filament tension, T_o . Thus, considering r_o constant as A approaches zero, the filament tension dominates the surface load and the shape is determined almost entirely by the edge loads. In the limit, $A = 0$, there is no surface load, and the surface becomes a hyperboloid of one sheet generated by the now straight filaments (See Flugge, Ref. 3, p. 78). This is indicated in Figure 11a where α_o and β_o are maintained constant and the meridional shapes shown reflect a parametric variation of A . For small values of A , Figure 11b demonstrates that the effect of β_o on the meridional shapes is to change the near-asymptotic angle of near-hyperbolic curves. Figure 11c demonstrates that the isotensoid generated by these conditions are circularly symmetric arches supported on two peripheral lines by forces with both axial and vertical components. If, however, the upper portion of the surface is terminated where a horizontal tangent occurs $(\alpha = \pi/2)$ the axial surface of load A is supported entirely at the base periphery and the upper periphery requires only radial support loads. A wire model of this configuration was constructed and is shown in Figure 12. The

37

intersections of the wires are spot welded to allow interfilament force transfer. Note also that a simultaneous reversal of the sense of the acceleration, "a", and the filament load, T_O, does not affect either the load parameter, "A", or the solution shapes. Thus the surfaces described by the meridional curves in Figures 11 are, for axial loading conditions, either isotensoid or isocompressoid surfaces depending on the surface orientation with respect to the surface load and the edge condition. The model shown in Figure 12 is isotensoid if it is suspended in a gravity or acceleration field from the smaller internal periphery with the large edge down, or an isocompressoid "cantilever dish" if it is supported at the inner edge, with the inner edge down. Application of this cantilever dish to civil engineering structures is indicated.

Figure 11d shows the meridians of the isotensoid (or isocompressoid) shapes generated by axial loading for large values of r_O.

An interesting and practical shape is obtained as the radius r_O approaches infinity. To take this limit, let $r = r_\infty + y$ where r_∞ is a parameter. Then Equations (n) and (o) read

(p)
$$\frac{d\alpha}{dy} = -\bar{A} \sec^2\beta + \frac{\tan^2\beta \, \text{ctn}\alpha}{r_\infty + y}$$

(q)
$$\frac{d\beta}{dy} = -\frac{\bar{A} \, \text{ctn}\alpha}{\sin\beta \, \cos\beta} - \frac{\tan\beta}{r_\infty + y}$$

and Equation (18) becomes

(r)
$$\frac{dz}{dy} = -\text{ctn}\alpha$$

where

$$\bar{A} = A/r_O = m'a/T_O$$

$\bar{A}$ can also be written as

$$\bar{A} = \frac{\rho}{\sigma} n$$

Now let $r_\infty \to \infty$. (y, z) are now cartesian coordinates and Equations (p), (q), and (r) read

$$\frac{d\alpha}{dy} = - \overline{A} \sec^2 \beta$$

$$\frac{d\beta}{dy} = - \frac{\overline{A} \ ctn\alpha}{\sin\beta \ \cos\beta}$$

$$\frac{dz}{dy} = - ctn\alpha$$

This system of equations is easily integrated with the following result:

$$z = \frac{\sin^2 (\beta_{max})}{2 \ \overline{A}} \left[1 - \left(\frac{2 \ \overline{A}}{\sin (2\beta_{max})} \right)^2 y^2 \right] \tag{46}$$

$$\sin\alpha \ \cos\beta = \cos\beta_{max} \tag{47}$$

$$ctn\alpha = \left(\frac{\overline{A}}{\cos^2 \beta_{max}} \ y \right) \tag{48}$$

$$\cos\beta = \cos\beta_{max} \left[1 + \left(\frac{\overline{A}}{\cos^2 \beta_{max}} \ y \right)^2 \right]^{\frac{1}{2}} \tag{49}$$

The integration constants were evaluated such that $Z = 0$ at the maximum value of y, and by Equation (47) $\beta = \beta_{max}$ at $\alpha = \pi/2$. The values of maximum z and y are

$$z_{max} = \frac{\sin^2 \beta_{max}}{2\overline{A}} = \left(\frac{\sigma}{\rho}\right) \frac{\sin^2 \beta_{max}}{2g} \tag{50}$$

$$y_{max} = \frac{\sin 2\beta_{max}}{2\overline{A}} = \left(\frac{\sigma}{\rho}\right) \frac{\sin 2\beta_{max}}{2g} \tag{51}$$

Equation (46) defines a strikingly simple isotensoid shape; a cylindrical parabola. This uniform stress shape can be used in civil engineering structures. The acceleration is then the gravitational field $g = 1$, and the internal loads are uniform compression.

The surface shapes determined from Equation (46) are shown in Figure 13a. Here, $z\overline{A}$ is plotted versus $y\overline{A}$, thus the complete range of shapes is given by parametric variation of β_{max} only. The filament angles determined from Equation (49) are shown in Figure 13b. Here β is plotted versus $y\overline{A}$ and once again the complete range of variations is given by parametric variation of β_{max}. Because of the way in which the design parameters β_{max} and $\overline{A}$ enter Equation (46), the ratio of z_{max} to y_{max} and the focal length can be varied independently. In fact from Equations (50) and (51),

$$\frac{z_{max}}{y_{max}} = \frac{\tan \beta_{max}}{2}$$

and from standard relations between focal length and the coefficients in Equation (46),

$$\text{Focal Length} = \frac{\cos^2 \beta_{max}}{2\overline{A}}$$

40

A model of this structure was made with slotted aluminum strips in order to demonstrate the foldability of the configuration. Pictures of the model in both the deployed and folded configurations are shown in Figures 14.

Case 4 - $K \neq 0$, $\Omega \neq 0$, $A = 0$. - In the remainder of this report the applied pressure is assumed uniform, $p = p_O$. With this stipulation and $A = 0$, the governing Equations (35) and (36) read:

$$\frac{d(\cos\beta \; \cos\alpha)}{dR} = KR \tag{52}$$

$$\frac{d(R \; \sin\beta)}{dR} = \frac{\Omega \; R^3}{(R \; \sin\beta)} \tag{53}$$

Equation (52) can be integrated directly, resulting in

$$\cos\alpha = [KR^2/2 + C_1] \; [\cos\beta]^{-1} \tag{54}$$

Equation (53) can be readily integrated, resulting in

$$R \sin\beta = \sqrt{\Omega \; R^4/2 + C_2} \tag{55}$$

where C_1 and C_2 are constants of integration. With the constant, C_2 , evaluated such that $\beta = \beta_O$ at $R = 1$ (and with the notation $\sin\beta_O = C$) , and with C_1 evaluated such that $\alpha = 0$ at $R = 1$, and letting $X = R$, Equations (55) and (54) are compactly expressed as

$$\sin\beta = \left[\frac{\Omega}{2} X + (C^2 - \frac{\Omega}{2}) \frac{1}{X} \right]^{\frac{1}{2}} \tag{56}$$

$$\cos\alpha = \pm \frac{\sqrt{1 - c^2} - \frac{K}{2}(1 - X)}{\left[1 - \frac{\Omega}{2}X - (c^2 - \frac{\Omega}{2})\frac{1}{X}\right]^{\frac{1}{2}}} \qquad (57)$$

For $\Omega = 0$, Equation (56) reduces to the equation for geodesic paths on a surface of revolution and Equation (57) reduces to Equation (30b) of Reference 8.

With the intrinsic filament geometry, β , and the intrinsic surface shape, α , known through Equations (56) and (57) as functions of the radial coordinate, X , the more practical design functions, Z and Φ , can be determined by integrating Equations (17) and (18). The filament length can also be determined by integrating the first of Equations (2). Changing to the X-notation, these equations read

$$\frac{dz}{dX} = -\frac{ctn\alpha}{2\sqrt{X}} \qquad (58)$$

$$\frac{d\Phi}{dX} = -\frac{\tan\beta}{2X \sin\alpha} \qquad (59)$$

$$\frac{d\ell}{dX} = -\frac{\csc\alpha \ \sec\beta}{2\sqrt{X}} \qquad (60)$$

Solutions of Equations (58) and (60) in terms of elliptic integrals of the first and second kind are given below. Equation (59) which determines the longitudinal position of a filament as a function of radial position leads in general to hyper-elliptic integrals and no attempt is made to record the closed form solution.

In order to integrate Equations (58) and (60) it is convenient to define a function, y , as

$$y^2 = X \cos^2\beta \ \sin^2\alpha \qquad (61)$$

42

Use of Equations (56) and (57) to eliminate β and α from Equation (61) yields the following expression for $y(X)$

$$y^2 =$$

$$\frac{K^2 X^3}{4} - \left[\frac{\Omega}{2} + K \left(\sqrt{1-C^2} - \frac{K}{2} \right) \right] X^2 + \left[1 - \left(\sqrt{1-C^2} - \frac{K}{2} \right)^2 \right] X - \left(C^2 - \frac{\Omega}{2} \right) \quad (62)$$

Equations (56), (57), and (61) can be used to eliminate β and α from Equations (58), (59), and (60) with the following result

$$\frac{dZ}{dX} = - \frac{\operatorname{ctn}\alpha}{2\sqrt{X}} = \mp \frac{\left[\left(\sqrt{1-C^2} - \frac{K}{2} \right) + \frac{K}{2} X \right]}{2y} \quad (63)$$

$$\frac{d\Phi}{dX} = - \frac{\tan\beta}{2X \sin\alpha} = \mp \frac{1}{2X\,y} \sqrt{\frac{\Omega\, X^2}{2} + C^2 - \frac{\Omega}{2}} \quad (64)$$

$$\frac{d\ell}{dX} = - \frac{\csc\alpha\,\sec\beta}{2\sqrt{X}} = \mp \frac{1}{2y} \quad (65)$$

To integrate these equations, note that y^2 has the form of a cubic in X, which expressed in factored form is

$$y^2 = \frac{K^2}{4} (1 - X) \, (X - X_2) \, (X - X_3) \quad (66)$$

where

$$X_2 = -\frac{2}{K^2}\left\{G - \sqrt{G^2 + K^2(C^2 - \Omega/2)}\right\}$$

$$\tag{67}$$

$$X_3 = -\frac{2}{K^2}\left\{G + \sqrt{G^2 + K^2(C^2 - \Omega/2)}\right\}$$

and

$$G = (K\sqrt{1 - C^2} + \frac{\Omega}{2} - \frac{K^2}{4}) \tag{68}$$

Investigation of these roots and Equation (66) shows that for real values of y, four types of solutions are possible for $0 \le C^2 \le 1$ and the range of X including $X = 1$,

Type A	$X_3 < X_2 \le X \le 1$
Type B	$X_3 < 1 \le X < X_2$
Type C	$X \le 1 < X_3 < X_2$
Type D	X_2 , X_3 complex conjugates $X \le 1$

$$\tag{69}$$

The solutions of Equation (63) for the shape $Z(X)$ and Equation (65) for the filament length, $\ell(X)$, are found in Reference 12 for the four types listed above.

Type A:

$$Z = \sqrt{1 - X_3}\left\{\left(1 - \frac{2}{K}\frac{\sqrt{1 - C^2}}{(1 - X_3)}\right)F(\psi_1, k_1) - E(\psi_1, k_1)\right\} \tag{70}$$

$$\ell = \frac{2 \ F(\psi_1, \ k_1)}{K \ \sqrt{1 - X_3}} \tag{71}$$

with

$$\sin\psi_1 = \sqrt{\frac{1 - X}{1 - X_2}} \tag{72}$$

and

$$k_1^{\ 2} = \frac{1 - X_2}{1 - X_3} \tag{73}$$

Type B:

$$Z = \tag{74}$$

$$\sqrt{X_2 - X_3} \ \left\{ E(k_2) - E(\psi_2, \ k_2) + \left[\frac{X_3 - 1 + \frac{2}{K} \sqrt{1-c^2}}{X_2 - X_3} \right] [K(k_2) - F(\psi_2, \ k_2)] \right\}$$

$$\ell = \frac{2}{K} \ \frac{1}{\sqrt{X_2 - X_3}} \ [K(k_2) - F(\psi_2, \ k_2)] \tag{75}$$

with

$$\sin\psi_2 = \sqrt{\frac{X_2 - X}{X_2 - 1}} \tag{76}$$

and

$$k_2^{\ 2} = \frac{X_2 - 1}{X_2 - X_3} \tag{77}$$

45

Type C:

$$Z = \tag{78}$$

$$\sqrt{X_2 - 1} \left\{ \frac{2\sqrt{1-c^2}}{K(X_2-1)} F(\psi_3, k_3) + E(\psi_3, k_3) - \tan\psi_3 \sqrt{1-k_3^2 \sin^2\psi_3} \right\}$$

$$\ell = \frac{F(\psi_3, k_3)}{\sqrt{X_2 - 1}} \tag{79}$$

with

$$\sin\psi_3 = \sqrt{\frac{1-X}{X_3-X}} \tag{80}$$

and

$$k_3^2 = \frac{X_2 - X_3}{X_2 - 1} \tag{81}$$

Type D:

$$Z = $$

$$\left[(1-d)^2 + b^2\right]^{\frac{1}{4}} \left\{ \frac{1}{2}\left(1 - \frac{2}{K}\frac{\sqrt{1-c^2}}{\sqrt{(1-d)^2+b^2}}\right) F(\psi_4, k_4) - E(\psi_4, k_4) \right.$$

$$\left. + \frac{\sin\psi_4 \sqrt{1-k_4^2 \sin^2\psi_4}}{1+\cos\psi_4} \right\} \tag{82}$$

$$\ell = \frac{1}{2} F(\psi_4, k_4) \left[(1-d)^2 + b^2 \right]^{-\frac{1}{4}} \tag{83}$$

with

$$\cos\psi_4 = \frac{\sqrt{(1-d)^2 + b^2} - (1-X)}{\sqrt{(1-d)^2 + b^2} + (1-X)} \tag{84}$$

$$k_4^2 = \frac{1}{2} \left(1 + \frac{1-d}{\sqrt{(1-d)^2 + b^2}} \right) \tag{85}$$

and

$$d = -\frac{2G}{K^2} \tag{86}$$

$$b = \frac{2}{K^2} \sqrt{K^2 \left(\frac{\Omega}{2} - c^2 \right) - G^2} \tag{87}$$

47

Within each solution type are a multitude of isotensoid shapes. For the direct problem where K, Ω, and C are specified, the solution type can be identified by calculating the roots, X_2 and X_3, from Equations (67) and comparing with Inequalities (69). With the solution type identified, the meridional profile is determined by the appropriate equation for $Z(X)$ (Equation 70, 74, 78, or 82) with the aid of tabulated elliptic integrals. Figures 15 and 16 are generated from Equations (67)-(69) and indicate the solution type which governs for various values of the load parameters, K, Ω, and the design parameter, C. For example, in Figure 15, the boundaries between solution types are defined by C = constant curves in K, Ω space; and in Figure 16 the boundaries between solution types are defined by Ω = constant curves in K, C space. Note that solution type-C occurs over such a limited range of parameters that the thickness of the lines in Figure 15 obscures the region, and in Figure 16, the regions of solution type-C is barely discernible.

In order to identify and discuss the isotensoid meridional shapes generated by the solution equations over the entire range of the parameters K, Ω, and C, it is advantageous to resort to a semigraphical technique.

To this end, consider Equation (57), the equation for $\cos\alpha$, and note that the denominator in the expression is equal to $\cos\beta$. The expression for $\cos\alpha$ completely defines the meridional profiles, and the denominator ($\cos\beta$) completely defines the filament geometry within the surfaces generated by the meridians. Let the numerator be called N and the denominator D. Then

$$\cos\alpha = \pm \frac{N}{D} = \pm \frac{\sqrt{1 - c^2 - \frac{K}{2}(1 - X)}}{\sqrt{1 - \frac{\Omega}{2}X - (c^2 - \frac{\Omega}{2})\frac{1}{X}}} \tag{88}$$

The $\pm$ sign characterizes the symmetry of the meridional profiles with respect to an equatorial plane (for convenience, the plane $Z = 0$) and stems from the boundary condition, $\alpha(R = 1) = 0$.

The meridian profiles depend on the three parameters C, Ω, and K. However, Ω and K dominate the meridian profile to a greater extent than C. The semigraphical method of identifying the solution meridional profiles is facilitated by the fact that Ω and C appear without K in the denominator of Equation (88), and K and C appear without Ω in the numerator. The method is straightforward but its execution is tedious.

For the moment, let C be a fixed constant. Then N and D individually can be plotted versus X on the same graph with Ω as a parameter in the plot of D, and K as a parameter in the plot of N. The ratio of the values of the separate families on the graph for fixed X represents the $\cos\alpha$ at the value of X.

A great deal of information is immediately available by examination of these plots. For example, when $D > 1$, no real solution exists for β, thus a bound on the solution profile is established. When $N > D$, no real solution exists for α, thus a second bounding condition is apparent from observation of N and D. Further, by setting $N = D$, there results

$$\sqrt{1 - C^2} - \frac{K}{2}(1 - X) = \pm\sqrt{1 - \frac{\Omega}{2}X - \left(C^2 - \frac{\Omega}{2}\right)\frac{1}{X}} \qquad (89)$$

Equation (89) is the same cubic equation encountered in the elliptic integrals for Z, and its roots $(1, X_2, X_3)$ are given by Equation (67). As a consequence, by observing where $N = D$ on the plots of N and D versus X, and comparing with the inequalities (69), the solution types can be easily identified.

Other properties of the solution meridians are also evident. When $N = 0$, $\cos\alpha = 0$; thus α equals $\pi/2$ and the meridian locally attains a maximum or minimum value in Z. Further if N is everywhere nonzero, the meridional profile has no maxima or minima in Z. When $D = 1$, not only is a boundary in X reached, but $\beta = 0$ at this boundary. Also, since $X = R^2$, $X > 0$ is a requirement, and by stipulation, the coordinates are nondimensionalized such that $X = 1$ is always a limiting value for the meridional curves. (One exception, $X \neq 1$ at both boundaries, occurs in what is later termed special case 1 of region 3).

The numerator, N, is a family of straight lines with slope, $\frac{K}{2}$. All these lines pass through the point $(X = 1, N = \sqrt{1 - c^2})$ which is also an intersection point for D. This is a consequence of the boundary condition $\alpha = 0$ at $X = 1$, for then $\cos\alpha = 1$ and $N = D$.

Solution Types for Pressure and Spin Loading

The denominator, D, is sketched in Figures 17a-i. Examination of Equation (88) reveals that the D-curves always pass through the four points $(X = 1, D = \pm \sqrt{1 - c^2})$ and $(X = -1, D = \pm \sqrt{1 + c^2})$. Changing the value of C shifts these points on the $X = \pm 1$ lines but does not significantly alter the character of the curves. The sketches identify three naturally separated regions for values of the parameter, Ω, and the two interesting boundaries separating these regions. The sketches show how the distinctive curves for each group smoothly pass through the limiting boundary cases and change their basic character. In examining Figure 17, note that ϵ is a small positive number introduced only to show that the parameter, Ω, is close to a boundary case. The regions and boundaries are

Region 1	$\Omega < 0$	Figures 17a, b
Boundary Case 1	$\Omega = 0$	Figure 17c
Region 2	$0 < \Omega < 2c^2$	Figures 17d, e
Boundary Case 2	$\Omega = 2c^2$	Figure 17f
Region 3	$2c^2 < \Omega < \infty$	Figures 17g, h, i

Typical curves for the three regions and two boundary cases are sketched superimposed on Figure 18. In order to illustrate the conditions under which different solution types are encountered, a limited number of N-curves are also shown. The intersection of the N- and D-curves identifies the roots $(1, X_3, X_2)$ of the cubic Equation (89), and by comparison to Equation (69), the solution type is known. The region of interest in these

curves is in the vicinity of $X = 1$. The following facts are evident.

Region 1 $\Omega < 0$ (Figure 17a). - Only solution types A and B are possible. For solution type A, X_2 (Equation 67) is always the minimum value to which the meridian extends, and $\alpha = 0$ at that limit. The upper bound is always $X = 1$ at which $\alpha = 0$ also. For solution type B, $X = 1$ is always the minimum value to which the meridian extends, and the maximum value is defined either by X_2 (Equation 67) or the value of $X > 0$ at which $D = 1$. The upper limit will depend on N in this case.

Boundary Case 1 $\Omega = 0$ (Figure 17c). - Only solution types A and B are possible. For solution type A, the bounds are the same as when $\Omega < 0$; however, for solution type B, the maximum value to which the surface extends is always X_2 which can be quite large for small values of K.

Region 2 $0 < \Omega < 2C^2$ (Figure 17d). - Only solutions of type A and B are possible in this region; X_2 is always the minimum for type A, and X_2 is always the maximum for type B.

Boundary Case 2 $\Omega = 2C^2$ (Figure 17f). - Only solution types A and B are possible here. Note that only under the conditions $\Omega = 2C^2$ is it possible for the meridians to close in the axis of symmetry. This is illustrated by the N-curve labeled A on Figure 17f. For solution type A, either X_2 or zero is the minimum; and for solution type B, X_2 is always the maximum.

Region 3 $2C^2 < \Omega$ (Figure 17h). - In this region, all four solution types are possible depending on N. This region is covered in detail below.

Meridional Profiles for Pressure and Spin Loading

In each of Figures 19a-g there are two families of sketches. In the upper family are sketched one typical D- versus X-curve and a number of N- versus X-curves. The lower family of curves are sketches of the meridional profiles generated by the N-lines above. Note that these meridional profiles are topologically equivalent to the physical meridional profiles but are distorted

51

because they are sketched as functions of $X = R^2$, not R . Identifying numbers relate the meridians generated by each N-line shown. Number 1 always corresponds to large negative K . K increases as the identifying number increases, and the highest number on each figure corresponds to a large positive value of K . The solution type associated with each K-line is also recorded in the upper sketch.

Boundary Case 1, $\Omega = 0$, Figure 19a. - The N-line marked "1" corresponds to $K << 0$, passes through zero, and intersects the D-curve at $X = X_2 > 1$. Thus the slope of curve 1 in the lower sketch goes through zero and then ∞ , forming the meridian of closed loops shown. As K increases, the loops increase in size and X_2 increases as depicted by curve 2. In the limit, as $K \to 0$ curve 3 is approached. The surface shape corresponding to this meridian is a hyperboloid of one sheet generated by straight filaments having edge load but no surface load ($K = \Omega = 0$, see Flugge, Ref. 3 p. 78). The slope of the D-curves at $X = 1$ are

$$\left(\frac{d(D)}{dX}\right)_{X\ =\ 1} = \frac{1}{2}\frac{C^2 - \Omega}{\sqrt{1 - C^2}}$$

and the slope of the N- curves are

$$\left(\frac{dN}{dX}\right)_{X\ =\ 1} = \frac{K}{2}$$

As can be seen on Figure 19a, when the slope of the N-curve at $X = 1$ is less than the slope of the D-curve, solution type B results with $X > 1$. Thus for

$$0 < \frac{K}{2} < \frac{1}{2}\frac{C^2 - \Omega}{\sqrt{1 - C^2}}$$

N-curves typified by number 4 generate meridians which, when rotated about the axis of symmetry, generate periodically corrugated tubes with limits on X of $1 \leq X \leq X_2$. When

$$\frac{K}{2} = \frac{1}{2} \frac{c^2 - \Omega}{\sqrt{1 - c^2}}$$

the corrugations pass to the limiting case of a cylinder (curve 5). Note that this is also the transition from solution type B to solution type A. N-curve 6 generates corrugations once again; however, the limits on X are now $X_2 \leq X \leq 1$. N-curve 7 is a unique boundary between corrugations and loops. Note that for curve 7, $N \rightarrow 0$ and $N \rightarrow D$ at the same time. Thus $\beta \rightarrow \pi/2$ and an inward cusp is formed. N-curve 8 indicates that α goes through $\pi/2$ and then on to π, forming a loop inwards as shown. N-curve 9 generates the meridian of a torus which is the boundary between the two types of looped meridians shown (8 and 10). There is no closed-form equation for the values of K and C which generate this useful shape. However, the condition for this meridian is that $Z = 0$ at $X = X_2$. This is solution type A. Consequently, the torus conditions are obtained by setting $Z = 0$ in Equation (70) and $X = X_2$. In this case, $\psi_1 = \pi/2$ (see Equation 72 for $X = X_2$) and the incomplete elliptic integrals become complete elliptic integrals. The condition for a torus is therefore.

$$\left(1 - \frac{2}{K} \frac{\sqrt{1 - c^2}}{(1 - X_3)}\right) K(k_1) - E(k_1) = 0$$

where k_1 is given by Equation (73) and X_2 and X_3 by Equation (67) with $\Omega = 0$. For larger values of K, loops of type 10 in Figure 19a result.

Region 2 $0 < \Omega < 2c^2$, Figure 19b. - In this region the D-curve is closed and D is always less than 1. Curve 1 does

53

not differ from the case $\Omega = 0$; however, as K increases from large negative values, a value is reached where $Z = 0$ at $X = X_2$. This corresponds to curve 2, a toroidal shape with $X > 1$. The torus is the boundary between the two types of loops, curves 1 and 3. The torus conditions are obtained by setting $Z = 0$ in Equation (74) and $X = X_2$. As K increases further, the unique case labeled "4" occurs. Here D and N both go to zero, thus an outward cusp is formed with $\beta = \pi/2$ at the outer periphery. The condition for shape 4 is that $N = 0$ at $X = X_2$.

For higher values of K , corrugated tubes are formed, with the limiting case again a cylinder, 6 , at $X = 1$. The higher N-curves, 7 through 11, are similar to those discussed under boundary Case 1 and introduce no new shapes.

Boundary Case 2, $\Omega = 2C^2$, Figure 19c. - N-lines 1 - 6 correspond to solution types B and generate meridians already discussed: the two types of closed loops reported by the torus, an outward cusp in which $\beta = \pi/2$ at the periphery, and a corrugated tube degenerating to a cylinder when the slopes of the N- and D-curves are equal at $X = 1$. For larger values of K solution type A is encountered, and corrugated tubes inboard of $X = 1$ are generated (curves 7). The unique character of the solutions generated when $\Omega = 2c^2$ is found by examining curves 8 - 12 which are the only solution types which close on the axis of symmetry. When $\Omega = 2c^2$, the D-curve is a parabola which passes through the three points $(X = X_2 , D' = 0)$, $(X = 1 , D = \sqrt{1 - c^2})$, and $(X = 0 , D = 1)$ N-curve 8 is that N-curve which also intersects $(X = 0 , N = 1)$. Under these conditions, $X_2 = X_3 = 0$. When these conditions obtain, examination of the solution equations for solution type A yields $k_1^2 = 1$, $\psi_2 = \pi/2$ and because $F(\pi/2 , 1) = K(1) = \infty$, the meridional shape generated by curve 8 is asymptotic to the $X = 0$ line. The surface shape is therefore a closed pointed bottle of ∞ extent in Z . The relationship between K and C at which this shape is generated is obtained by setting $N = 1$ at $X = 0$. This yields

$$K = 2 (\sqrt{1 - c^2} - 1)$$

Skipping for the moment to N-curve 12, note that $N = -1$ at $X = 0$. It is easy to establish that $Z \to -\infty$ as $X \to 0$ for curve 12, and that $K = 2(1 + \sqrt{1 - c^2})$ defines this condition. For values of K between these two limits, the meridians close on the axis of symmetry and $\beta \to 0$ as $X \to 0$. Thus in order for the solution shapes to close on the axis of symmetry,

$$\left. \begin{array}{c} \Omega = 2c^2 \\[2ex] 2(\sqrt{1 - c^2} - 1) \leq K \leq 2(1 + \sqrt{1 - c^2}) \end{array} \right\} \qquad (90)$$

and $\beta = 0$ at $X = 0$.

Within this range, a distinct value of K generates curve 10 for which $\cos\alpha = 0$ at the axis of symmetry. This occurs when $N = 0$ at $X = 0$ or

$$K = 2\sqrt{1 - c^2}$$

thus for $2(\sqrt{1 - c^2} - 1) \leq K < 2\sqrt{1 - c^2}$ shapes typified by curve 9 are generated, and for $Z(\sqrt{1 - c^2} < K < 2(1 + \sqrt{1 - c^2})$, shapes typified by curve 11 are generated. These surface shapes are closed bottles requiring supporting structure at the apices while shape 10 is self supporting. Values of K above $2(1 + \sqrt{1 - c^2})$ generate the close-loop meridians represented by curve 13. It is not likely that closed loops of the other type (Curve 9 on Figure 19b) or tori are generated for this value of Ω in combination with positive values of K.

Region 3 $\Omega > 2c^2$, Figures 19d, 19e, 19f. - Region 3 is complicated by the fact that the D-curve has an inflection point. The position of this point relative to $X = 1$ has a distinctive effect on the solution types generated.

It can be shown that for $1 > c^2 > 1/3$ the inflection point

$\left(\dfrac{d^2}{dX^2} D = 0\right)$ occurs in the range $X < 1$. For $c^2 < 1/3$, it occurs in the range $X > 1$ provided

$$1 - \sqrt{1 - 4c^2 + 3c^4} < \Omega < 1 + \sqrt{1 - 4c^2 + 3c^4} \qquad (91)$$

When $\Omega > 2$, the inflection point occurs at values at X where D is greater than 1 ($X < X$ minimum). Thus three distinct cases arise, hereafter referred to as special cases. In special case 1 the inflection occurs at $X > 1$, Figure 19d. The conditions for this case are $c^2 < 1/3$ and Ω bounded by Equation (91). These are the only conditions under which solution type C is encountered where X_2 and X_3 are greater than $1 > X$ (N-curve 7C in Figure 19d). In the range of Ω for which Figure 19d applies, N-curves 1 – 5 are similar to those discussed before. N-curve 7C typifies the only range of solution type-C.

Note that a fifth solution type is possible. It occurs only under the same conditions as solution type-C and generates corrugated tubes (curve 7). For this solution type $1 < X_3 \leq X < X_2$. This is the exception identified earlier where the solution is not bounded by $X = 1$. The solution equations for this rare case are not recorded here but can be obtained from Reference 12.

Of particular interest is the fact that in this range of Ω and c^2, the D-curve is concave upward at $X = 1$. As a consequence, when the slope of the N-curves is equal to the slope of the D-curves at $X = 1$, solutions for $X \geq 1$ and $X \leq 1$ occur for the same values of all parameters. Thus a corrugated shape can fare into an inward arch with compatible filament patterns at $X = 1$. This is shown by the extension to curve 6 in the lower sketch of Figure 19d. When the inflection point is at $X = 1$, which is the condition which separates special cases 1 and 2, the corrugated tubes degenerate to a cylinder when D and N have the same slope; thus the interesting meridian which generates a cylinder with an end cap identified by the numbers 6 – 7 on Figure 19d is obtained.

56

Once the slope of N is greater than the slope of D at
X = 1 , the lower limit of the solution shapes is reached at the
value of X where D = 1 and β = 0 . Thus curves 6 - 11
generate meridional profiles with central openings requiring
support of the filaments. That unique curve corresponding to
$\cos\alpha = 0$ ($\alpha = \frac{\pi}{2}$) at the same value that D = 1   (curve 9)
requires only hoop constraint while all others require tension
or compression support.

The limiting value of K for these solutions is obtained
by setting N = -1 at $X = X_2$ (curve 11). For values of K
larger than this, the closed loops like curve 12 are obtained.
It is doubtful that tori and the other type of loops exist for
large values of K and this range of Ω . With reference to
Figure 17h, it is apparent that solution type D is encountered
whenever the N-lines intersect neither the D-curve for nega-
tive X nor the D-curve for positive X except at X = 1 .
This occurs for two ranges of K , one negative and one positive.

In a second special case, the inflection occurs between the
value of X where D = 1 and X = 1 . This is shown on Figure
19e. The conditions for this are $2c^2 < \Omega < 2$ and $1 > c^2 > 1/3$
or $2c^2 < \Omega < 2$, $c^2 < 1/3$ and Equation (91) not satisfied. The
curves associated with all numbers but 8 are similar to cases
already covered. For N-curve 8, the N-line and D-curve are
tangent at $X = X_2 = X_3$. This represents a branch or bifur-
cation point from which two isotensoid meridians are possible as
shown in the lower sketch 8 in Figure 19e.

The third special case is obtained when $\Omega > 2$ and is shown
in Figure 19f. There the inflection point in D falls outside
the range of real solutions. All the profiles except those num-
bered 8 and 12 have been discussed above. In cases 8 and 12,
$D = \pm 1$ at $X = X_2$ and N = 1. Thus for case 8, a corrugated
tube is formed in which β = 0 at the inner radius, and for
case 12 loops are formed for which β = 0 at the inner or
minimum radius.

In general, Region 3 includes solutions of types A, B, and
D and for certain special conditions, type C. The minimum radial
coordinate to which the solutions extend is bounded by the value

of X where $D = 1$ over most of the range of K applicable to solution types A, D and C.

In Figure 19g the isocompressoid meridional profiles are shown for $\Omega < 0$. Recalling the definition of Ω (Equation 12) the filament load, T_o , is necessarily less than zero if $\Omega < 0$. For $T_o < 0$, the sense of p_o is reversed in the sign convention for K . The N-lines 1, and 7 through 13 generate meridional profiles already discussed. In each case, however, the pressure loading is reversed and the internal loads are compressive. For N-curves 2 and 6, $N = \pm 1$ respectively and $D = 1$. Thus curve 2 generates outward loops tangent to the value of X at which $X = X_2$ and $D = 1$ simultaneously. In this case $\beta = 0$ at the outer periphery. For curve 6 a corrugated tube is formed tangent to the same X value at its outer periphery and with $\beta = 0$. Curves 3, 4, and 5 are inward arches with positive, zero, and negative slope at the outer periphery defined by $D = 1$. The special case when $K = 0$ (not shown on Figure 19g) was discussed under the general case 2 for which $K = A = 0 \; \Omega \neq 0$.

In order to illustrate briefly the design potential, four spinning pressurized isotensoid designs are given. Figure 20 shows a closed spinning isotensoid pressure vessel. This design closes on the axis of symmetry and is obtained by choosing $\Omega = 2c^2$ and determining C by setting $N = 0$ at $X = 0$. This corresponds to N-curve 10 in Figure 19c. Figures 21 and 22 are spinning isotensoid "tires" with, $\beta = 0°$ $(\Omega > 2c^2)$ and $\beta = 90°$ $(\Omega < 2c^2)$ at the inner periphery, respectively. They correspond to N-line 8 on Figure 19b for zero β at the hub, and N-line 9 on Figure 19d for $\beta = 90°$ at the hub.

Figure 23 depicts a design of a spinning net with internal (positive) pressure on the upper portion and external (negative) pressure on the lower portion, representative of the loading on a spinning aerodynamic decelerator.

Case 5 - $K \neq 0$, $\Omega \neq 0$, $A \neq 0$. - An analytic solution was not found for this general loading case where all loads are nonzero. The equations suitable for integration by digital computer were used. These are Equations (18), (39), (40) when α is sufficiently far from zero; and Equations (41), (42), and (43)

58

when α is sufficiently far from $\pi/2$. There are five signifi-
cant parameters in these equations: the three load parameters
K , Ω , and A , and two boundary parameters, β_o and α_o at
$r = r_o$. (The third boundary parameter, Z_o , is unessential
because it serves only to shift the surface with respect to the
Z-axis.) This results in a five-dimensional space to explore
for significant shapes using numerical techniques. As a conse-
quence, no attempt to classify shapes was made. Instead, a
modest attempt was made to determine the effect of a uniform
acceleration load, A , on the shapes determined in the previous
case treated where only K- and Ω-loads were present. The
details of the calculation as well as the computer program used
are given in the Appendix.

In order to obtain a reasonably broad coverage, β_o was
set equal to 45° and held constant so that $c^2 = \frac{1}{2}$. Shapes were
determined for $\Omega < 2c^2$, $\Omega = 2c^2$, and $\Omega > 2c^2$ for various
values of K and for $A = 0$. For each one of these shapes
determined, a second shape was determined for $A = 0.25$. The
plots of the resulting meridional profiles shown in Figures 24
illustrate the sensitivity of isotensoid shapes to axial loading
$A \neq 0$.

In particular, note that none of the isotensoids with the
A-load present extend to the axis of symmetry. This leads to
examination of the governing equations for values of R near
zero to determine if there are any isotensoid surfaces with
$A \neq 0$ which close on the axis of symmetry. The details of
this study are included in the Appendix. The results can be
summarized as follows:

In the vicinity of $R = 0$, the filament angle, β , and
the meridional angle , α , are governed by the approximate
relations

$$\beta \cong \sqrt{\frac{\Omega - A^2}{2}}\, R - \frac{KA}{10\sqrt{\frac{\Omega - A^2}{2}}}\, R^2 \tag{92}$$

59

$$\alpha \cong \frac{\pi}{2} - AR - \frac{K}{2} R^2 \qquad\qquad (93)$$

It is apparent from Equation (92) that $\Omega > A^2$ is a necessary condition for closed shapes.

In order to illustrate surfaces of this type, Equations (92) and (63) are used to generate values of α and β for small r which can be used as initial conditions for the governing Equations away from the singularity at $R = 0$. The results are shown in Figure 25 for $\Omega = 1$, $K = 1$, and a range of A; and in Figure 26 for $\Omega = 1$, $K = 0$ for a range of A. The variation of β with R is shown in Figure 27 for one case, $\Omega = 1$, $K = 0$, $A = 0.1$. This is representative for all cases shown. Note that $\beta = 0$ at the lower opening in the surface, thus, a tension ring (or the load equivalent) and an axial force must be supplied for equilibrium. There is an indication therefore that this analysis may be applied to approximate conditions for design of a high-altitude (spinning) parachute of the type discussed in Reference 13. The edge condition is then supplied by payload weight which is suspended from the filaments.

CLOSURE

The results reported here represent a step toward reducing net structure design to standard methods. Consideration has been restricted to axisymmetric nets subject to axisymmetric but, in general, non-normal surface loads. The filament geometry is restricted to two families of filaments symmetrically disposed within the surface.

In the problems where the exact surface shape is prescribed, the tension variation, filament geometry, and interfilament force level are given in terms of load levels and boundary conditions. Also, the region of the prescribed shape over which a net structure can be used to react the loads is given as a function of the design parameter, $C = \sin\beta_o$.

The exact shape cannot be prescribed if isotensoid design is desired in two-family systems; however, some freedom in design is possible. When the load conditions are pressure and spin $(K \neq 0$ $\Omega \neq 0$, $A = 0)$ the designer may refer to the classification of shapes in Table I and determine values of the design parameter, $C = \sin\beta_o$, which generate isotensoid shapes best suited for the particular design application. With K , Ω , and C known, the surface shape may be determined from the appropriate closed-form solutions which require use of elliptic integral tables, or the digital computer program given in Appendix A may be employed. When the load condition includes $A \neq 0$, use of the digital computer program is mandatory. If, in this case, it is desired that the surface close on the axis of symmetry, the method for generating initial conditions near the apex as outlined in Appendix A, may be employed.

It is clear from the restrictions placed on the solutions obtained that a number of problems cannot as yet be handled. The most glaring omission for symmetric loading is the ability to prescribe structure shape and obtain isotensoid design solutions. Two directions can be taken in attacking this problem, both requiring an increase in the number of layers of filaments in the net. First, a finite number of layers as treated in Reference 8, with the addition of interfilament force transfer between families in each layer, F_c , and interfilament force transfer

61

between layers, F_m, will allow isotensoid design when shape is prescribed. Second, passage to a continuum of filament layers, as done in Reference 10, may be attempted. Non-uniform pressure and meridional surface loads must be included, however, and the non-geodesic nature of the filament paths must be accounted for so that the internal meridional and circumferential loads are accommodated. This leads to a pair of integral equations for the distribution of filament density as defined in Reference 10. As discussed earlier, physical interpretation of the results of this method requires approximation by a finite number of layers. It, therefore, appears that the assumption of a finite number of layers at the onset is the best approach. If an exact solution covering the required region of the prescribed shape is not possible, the difference between the resulting shapes and the prescribed one may be minimized with respect to the boundary values of the angles in each layer.

A second serious omission is the ability to design isotensoid filament surfaces in the presence of asymmetric loading. It is apparent that isotensoid design is not possible if the load distribution varies with time. However, for fixed asymmetric loads, say of the type which lead to resultant moment, shear and torque at the surface edges, the conditions under which isotensoid design is possible can be determined. This could lead to significant weight savings for some design applications.

Finally, the role of interfilament force level has not been exploited as a full design parameter. The weight of a net will be affected by the level of the interfilament forces because matrix material or knots are present. Thus, it may be desirable to use the maximum value of interfilament force as a design parameter in much the same way as $C = \sin\beta_o$ is employed. Methods should then be developed to have the interfilament force as a design input. Also, isotensoid shapes could be classified in terms of this parameter instead of $C = \sin\beta_o$.
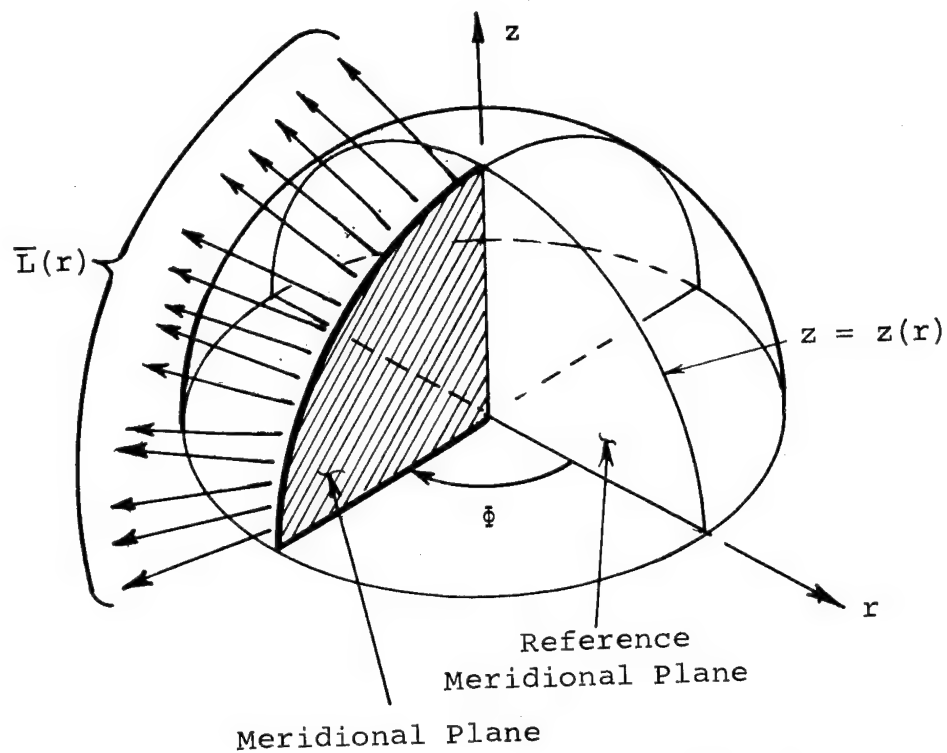
Figure 1.   Coordinates and Surface Load
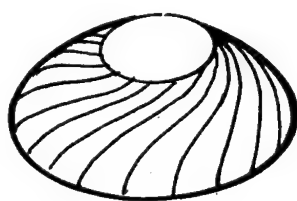
2a   Fiber Set at β
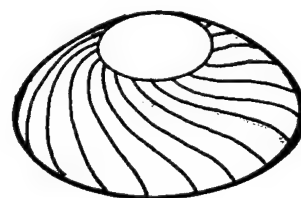
2b   Fiber Set at -β
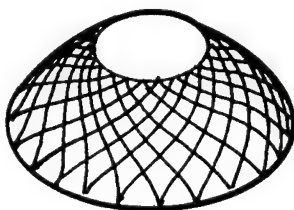
2c   Fiber Layer with
      Complimentary Sets
      at β and -β
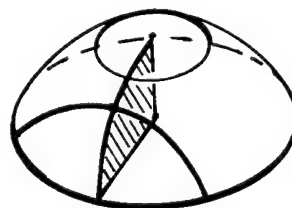
2d   Single Fiber Be-
      longing to Both
      Sets in a Layer

Figures 2.   Definition of Filament Sets and Filament Layers
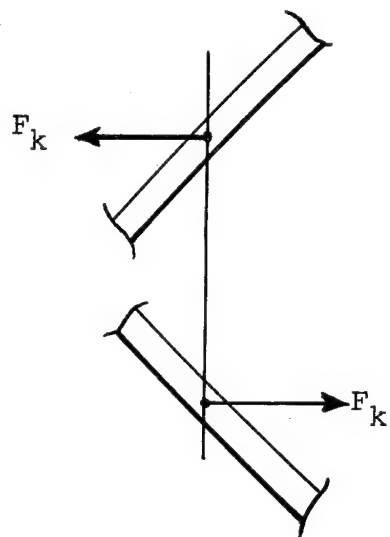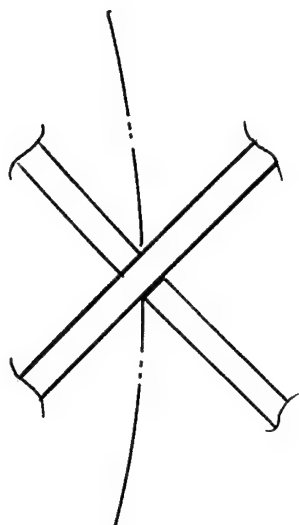
Glued Intersection
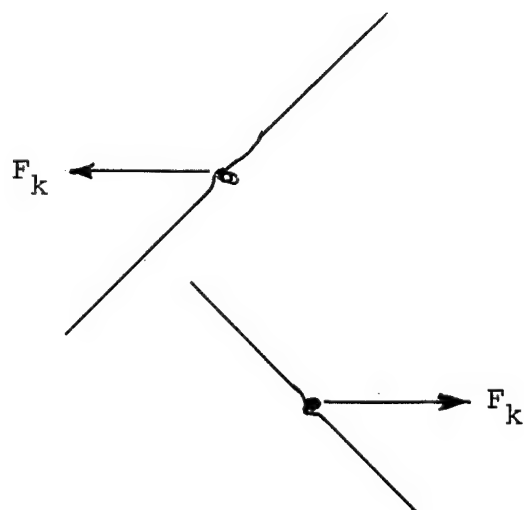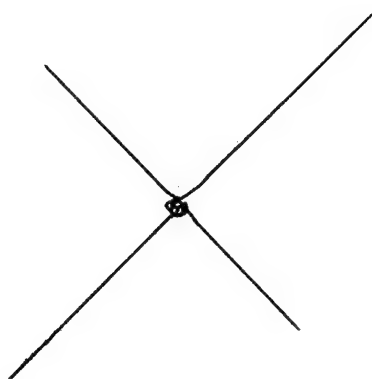
Knotted Intersection

Figure 3.   Force Transfer Between Filaments in Complementary
Sets of One Layer

64
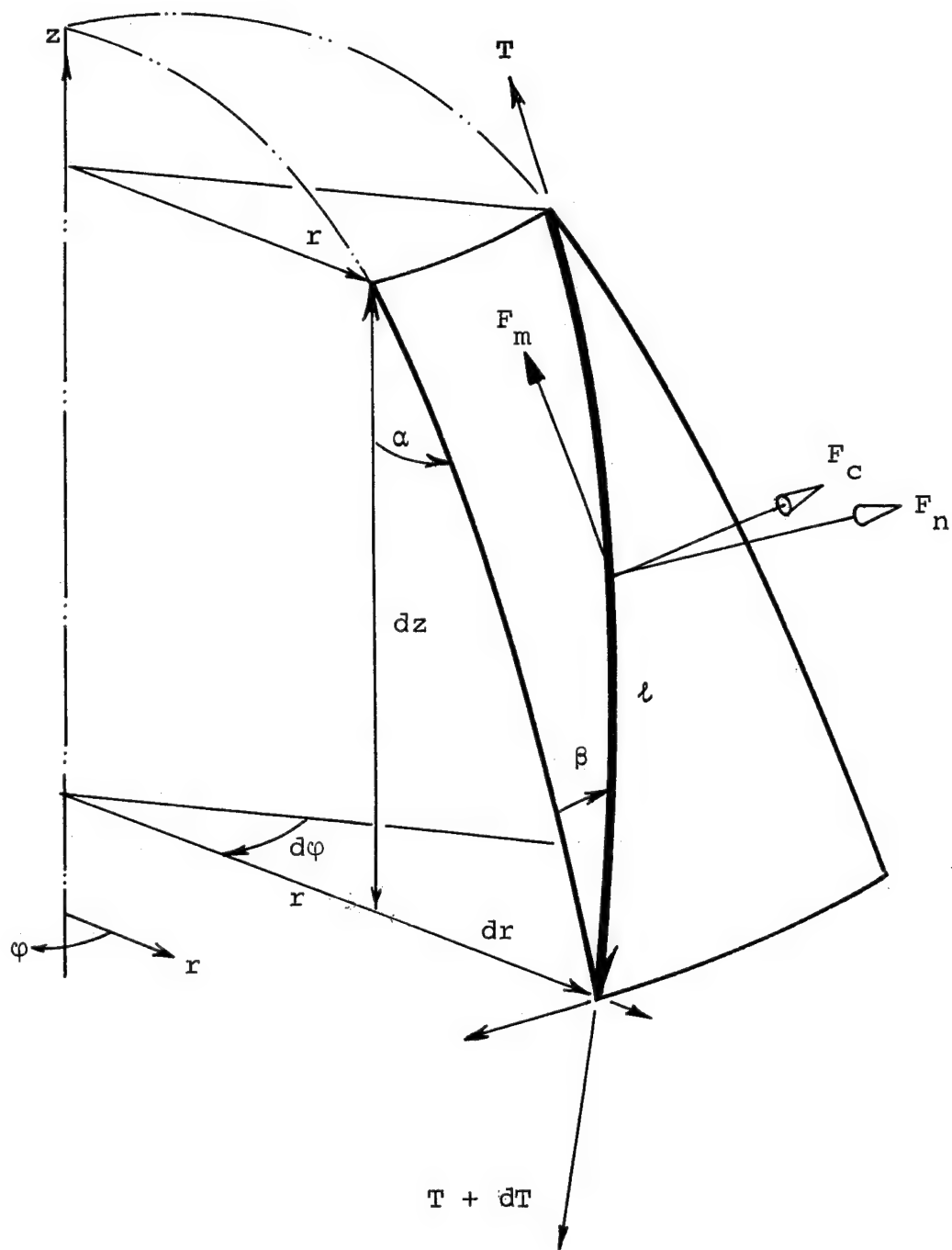
Figure 4   Coordinates and Notation

65
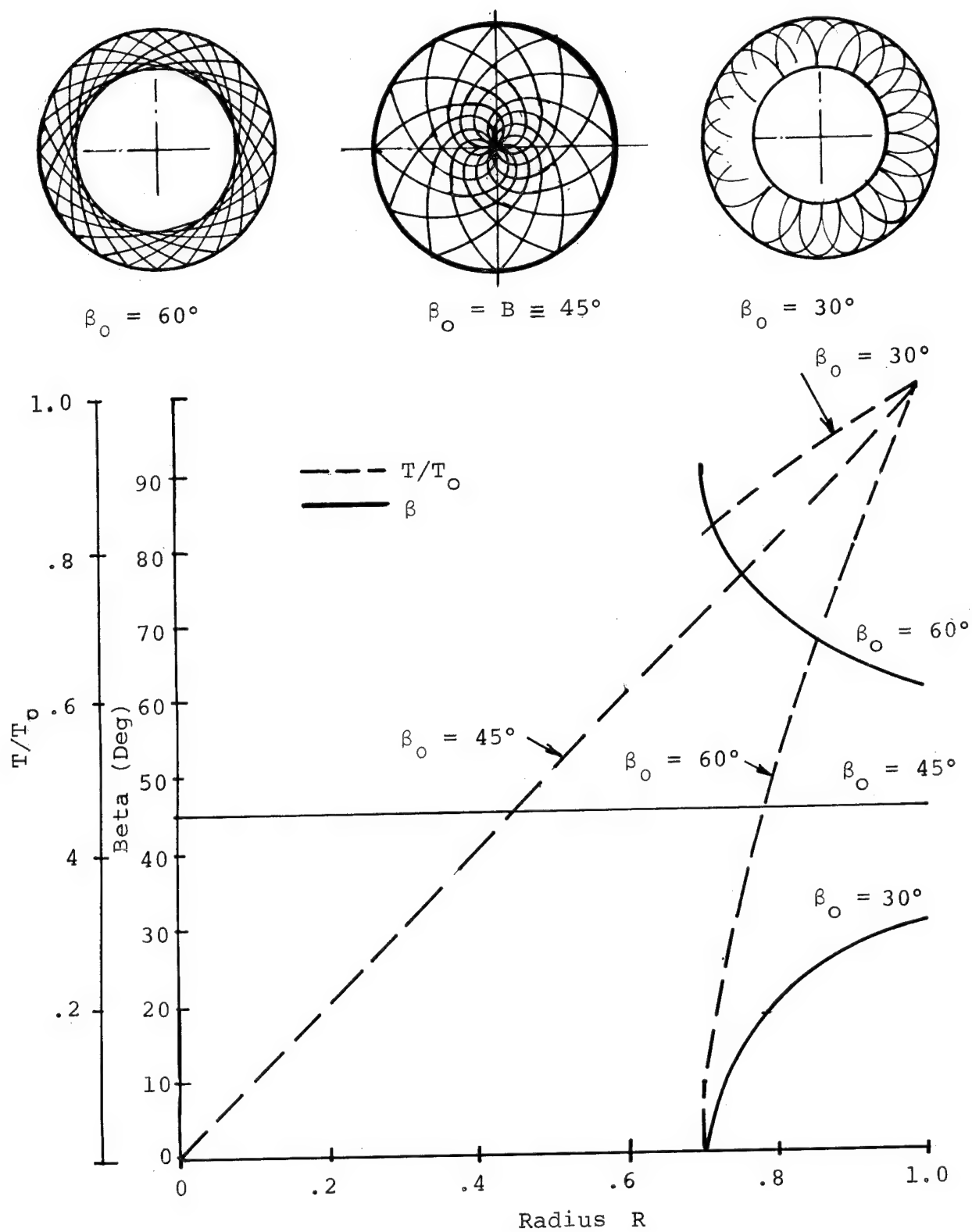
Figure 5.   Uniform Pressure in Spherical Container
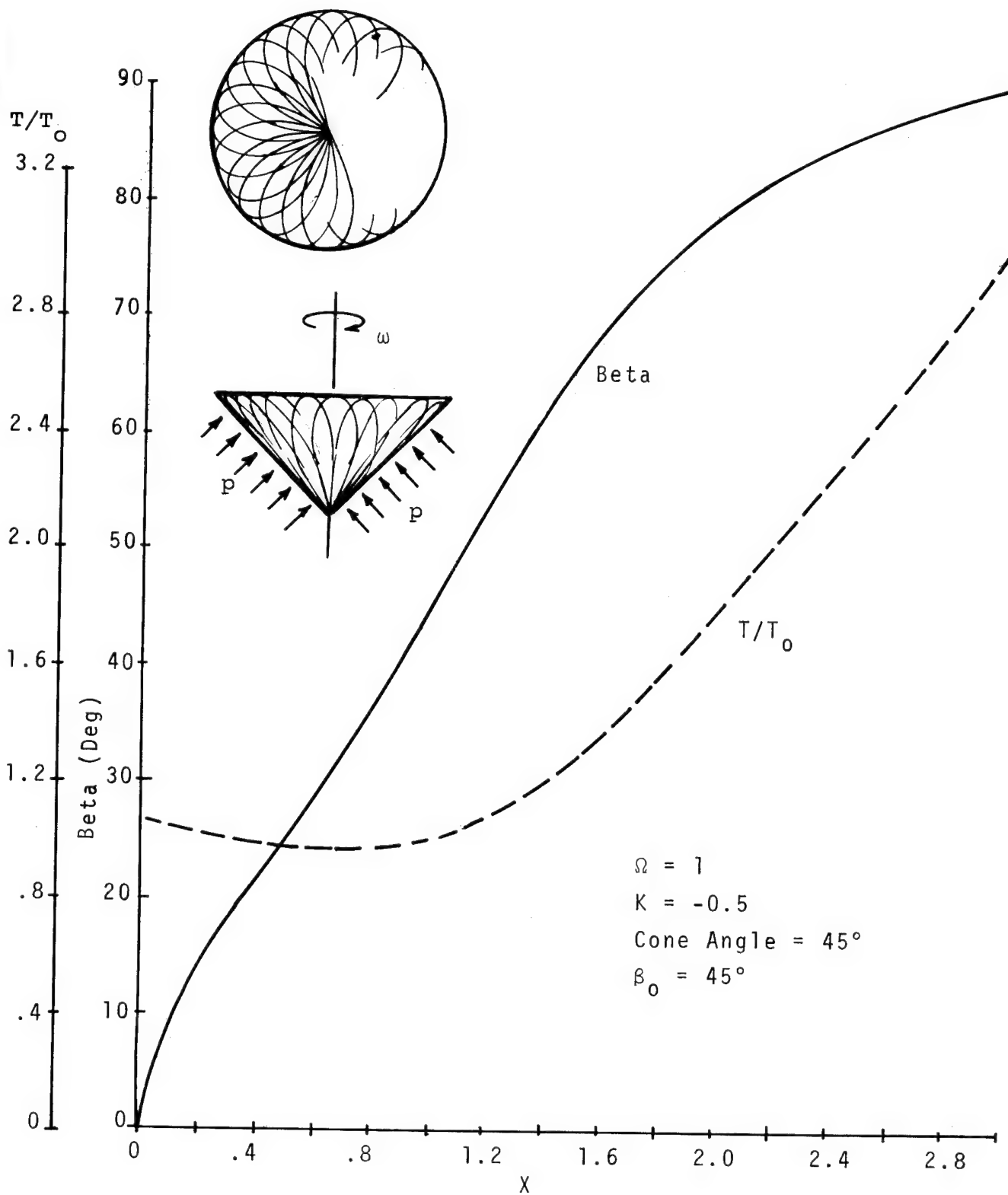
Figure 6.   Spinning Cone in Supersonic Flight
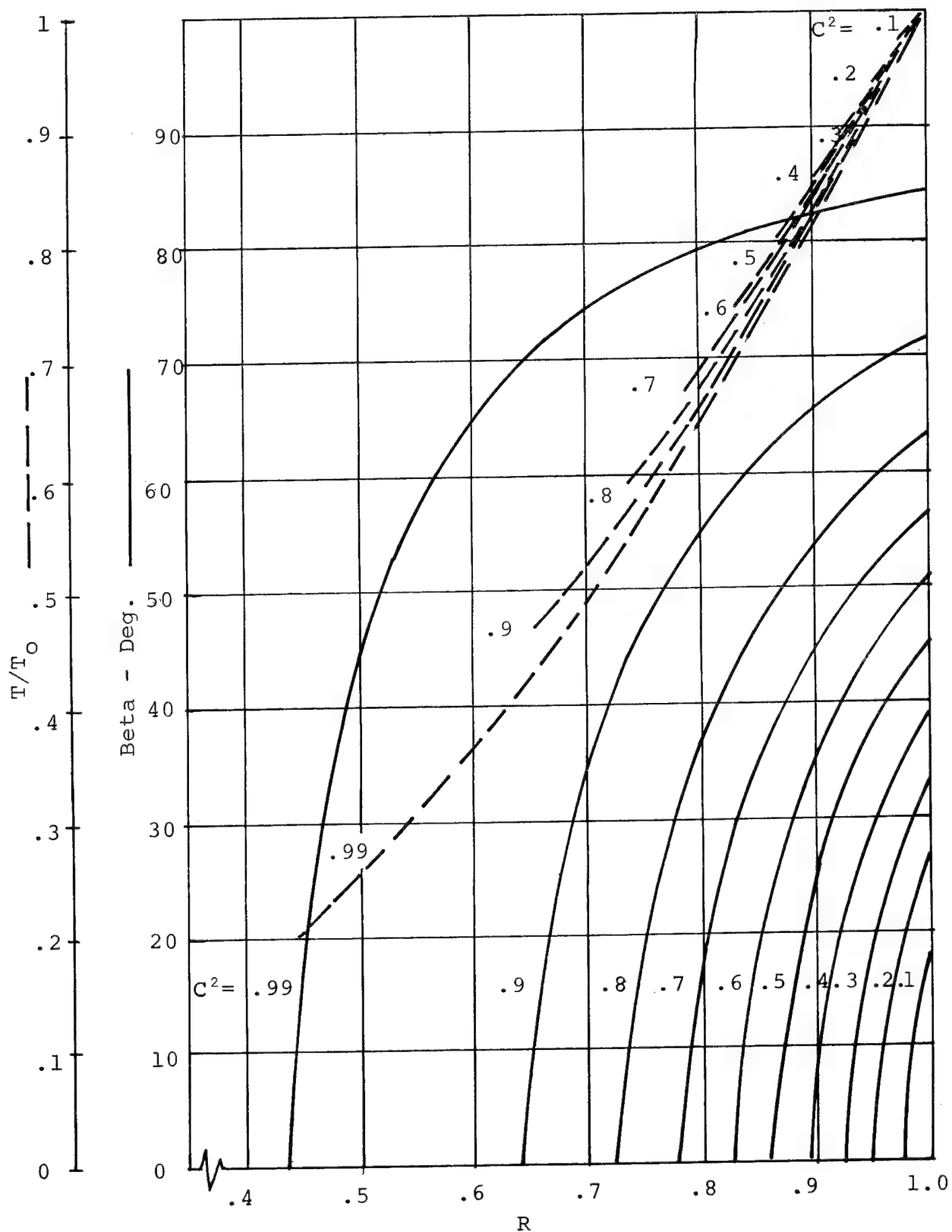
Figure 7.   Tension and Filament Geometry in Spinning Paraboloids
With $\sin^2\beta_O = C^2$ as Parameters

68
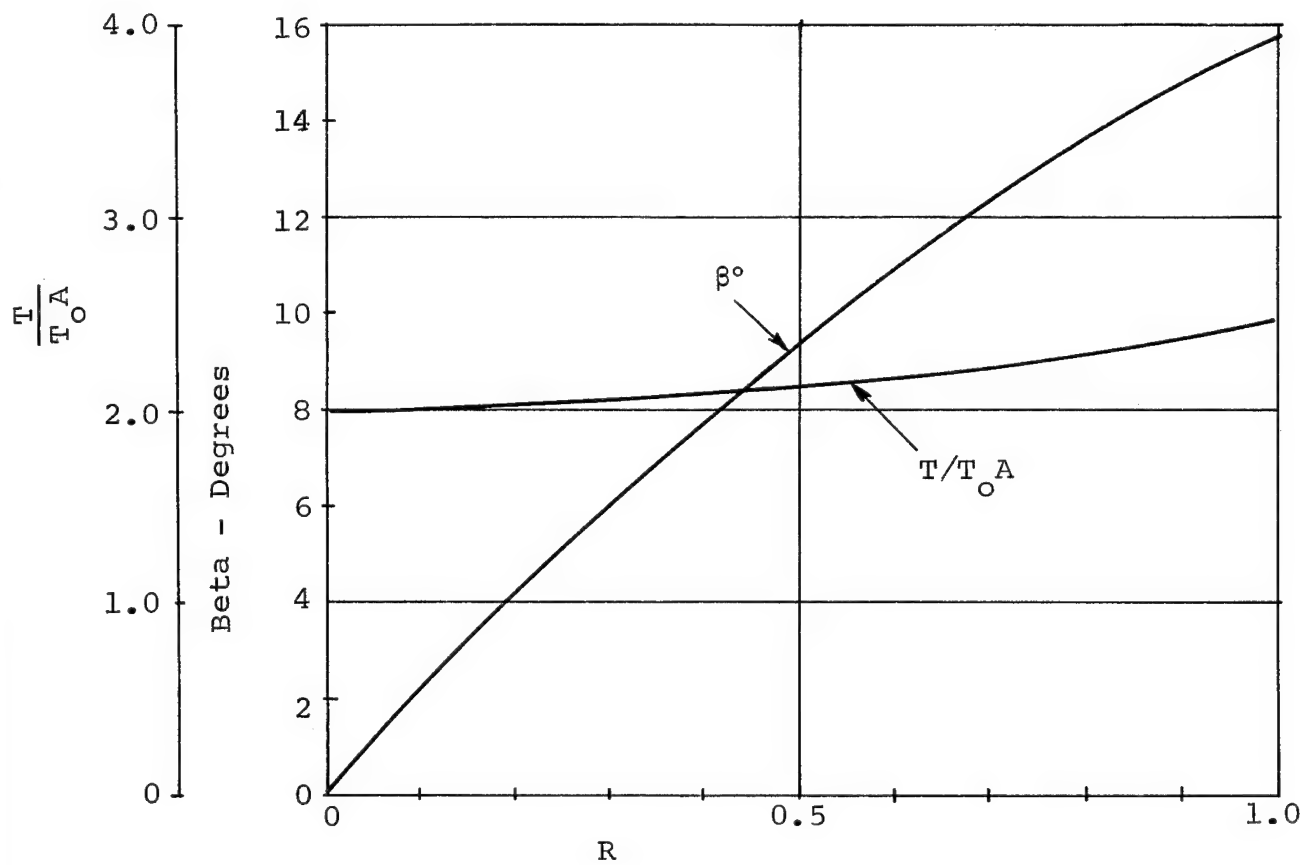
Figure 8. Filament Tension and Filament Angle in Gravity-
Loaded Parabolic Net

69
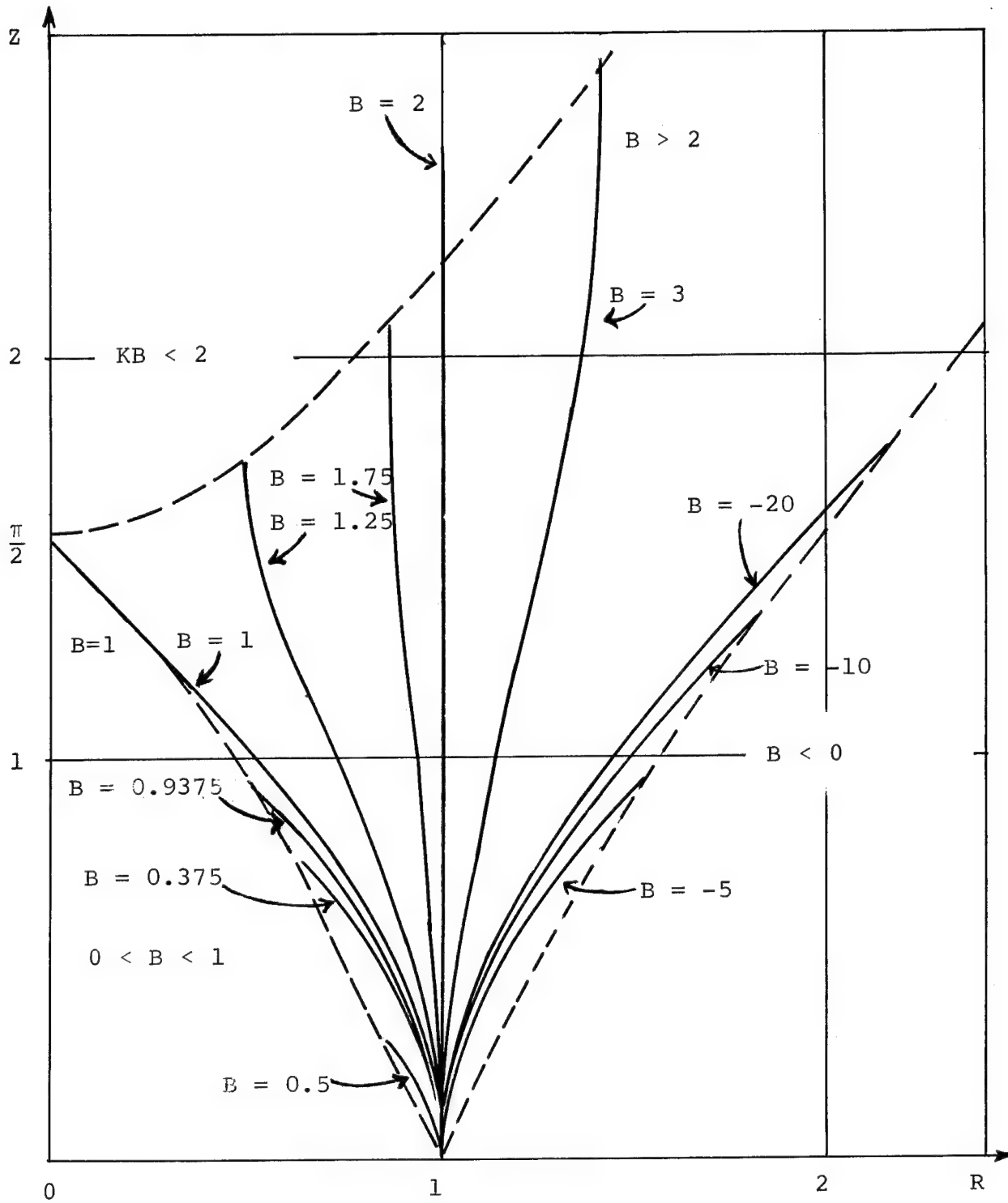
Figure 9. Meridians of Spinning Isotensoids
(Isocompressoids) $\beta_o = 45°$ $B = 1/\Omega$
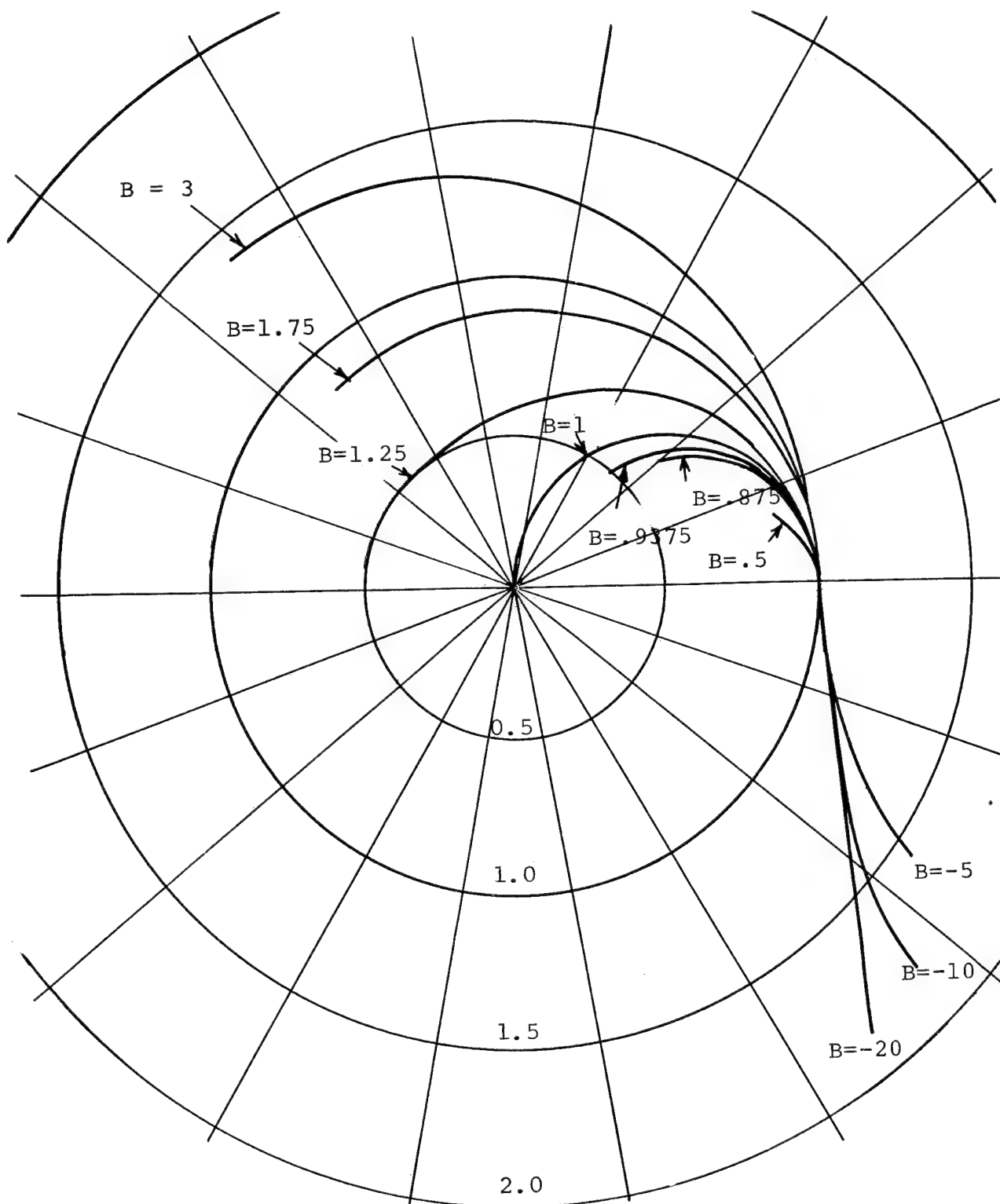
Figure 10. Fiber Path of Spinning Isotensoids
(Isocompressoids) $\beta_o = 45°$ $B = 1/\Omega$
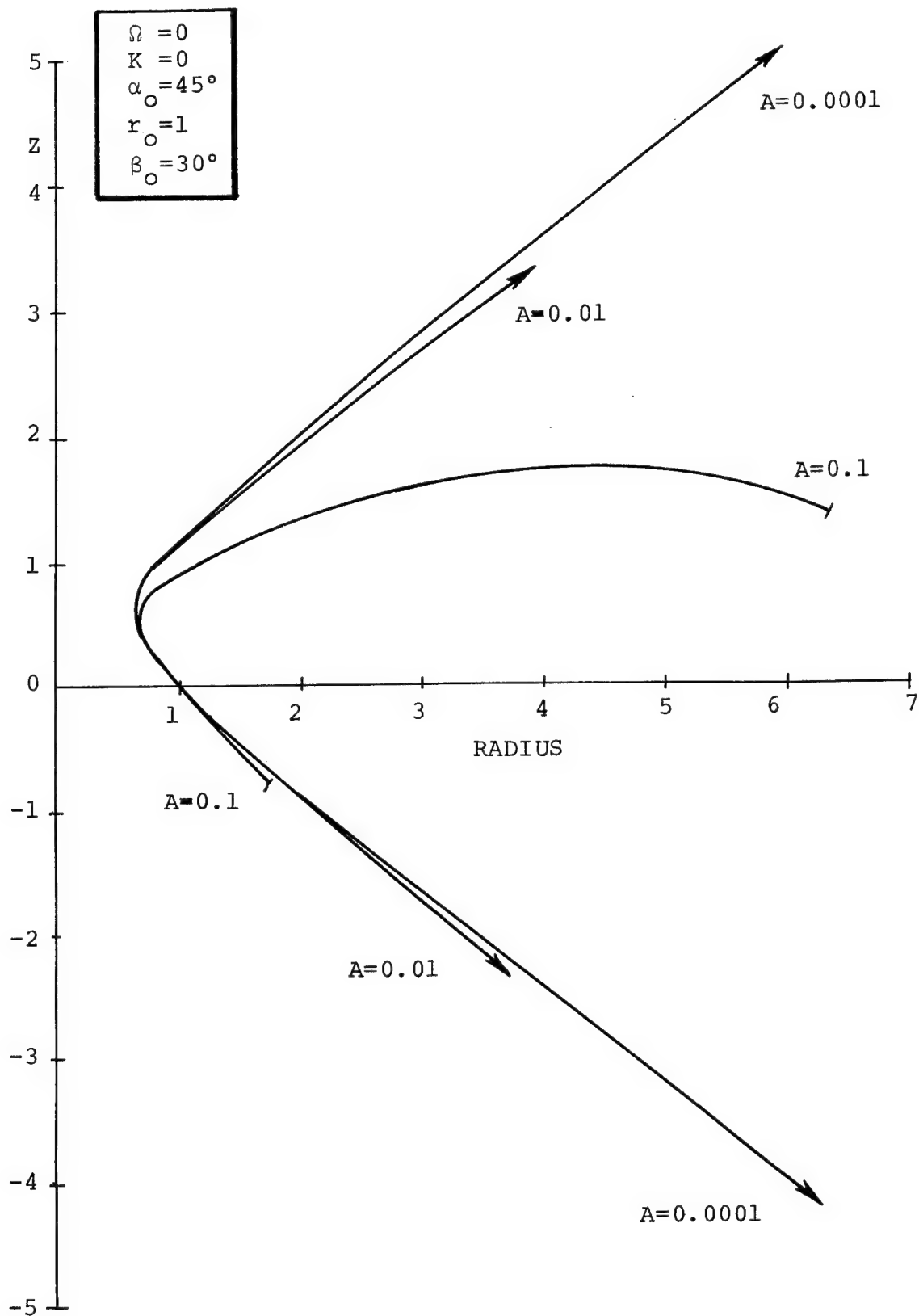
Figure 11a.   Computed Meridional Shapes for Axial
                Load (K = Ω = 0, À ≠ 0)
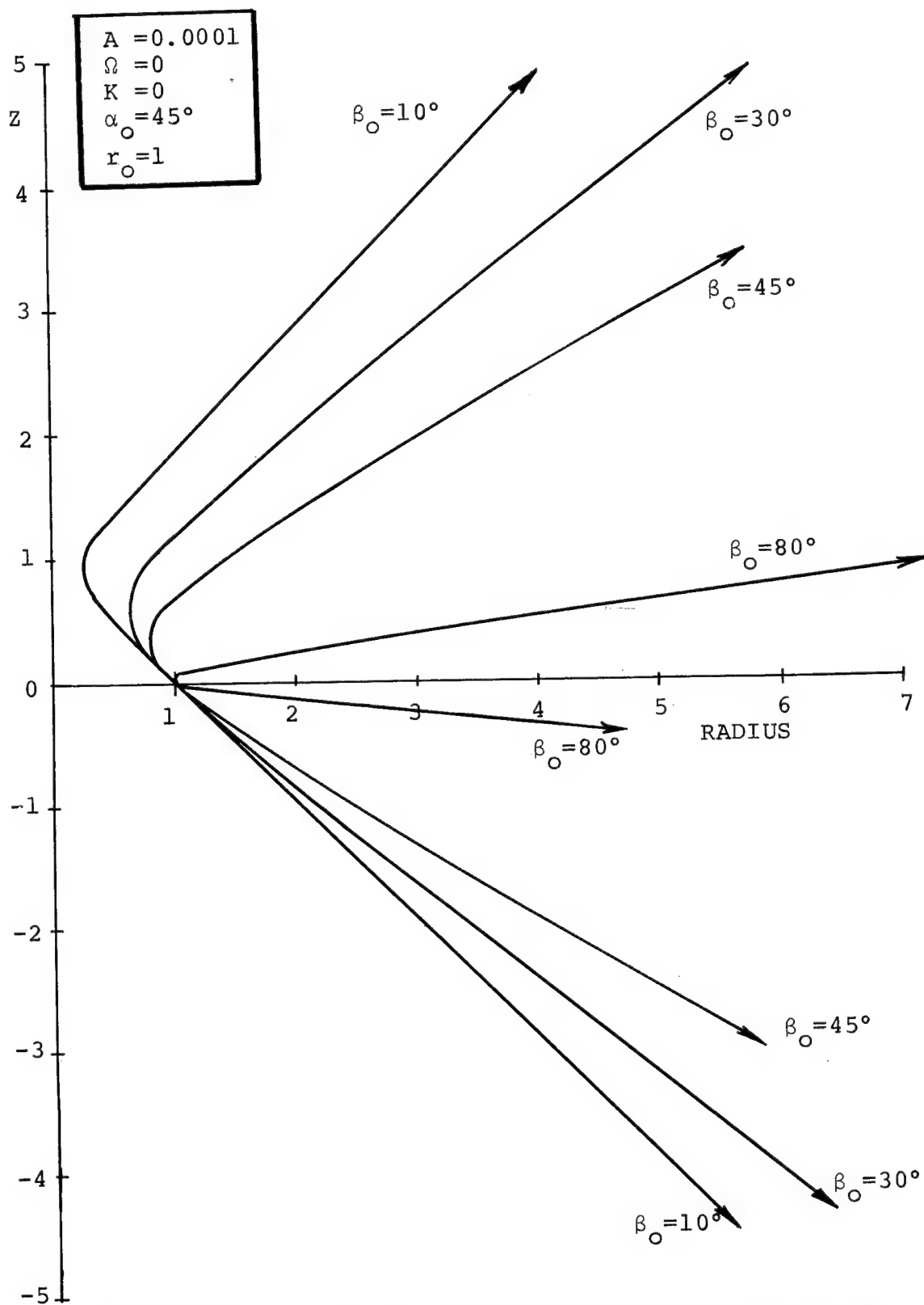
Figure 11b.   Computed Meridional Shapes for Axial
Load $(K = \Omega = 0, A \neq 0)$

73
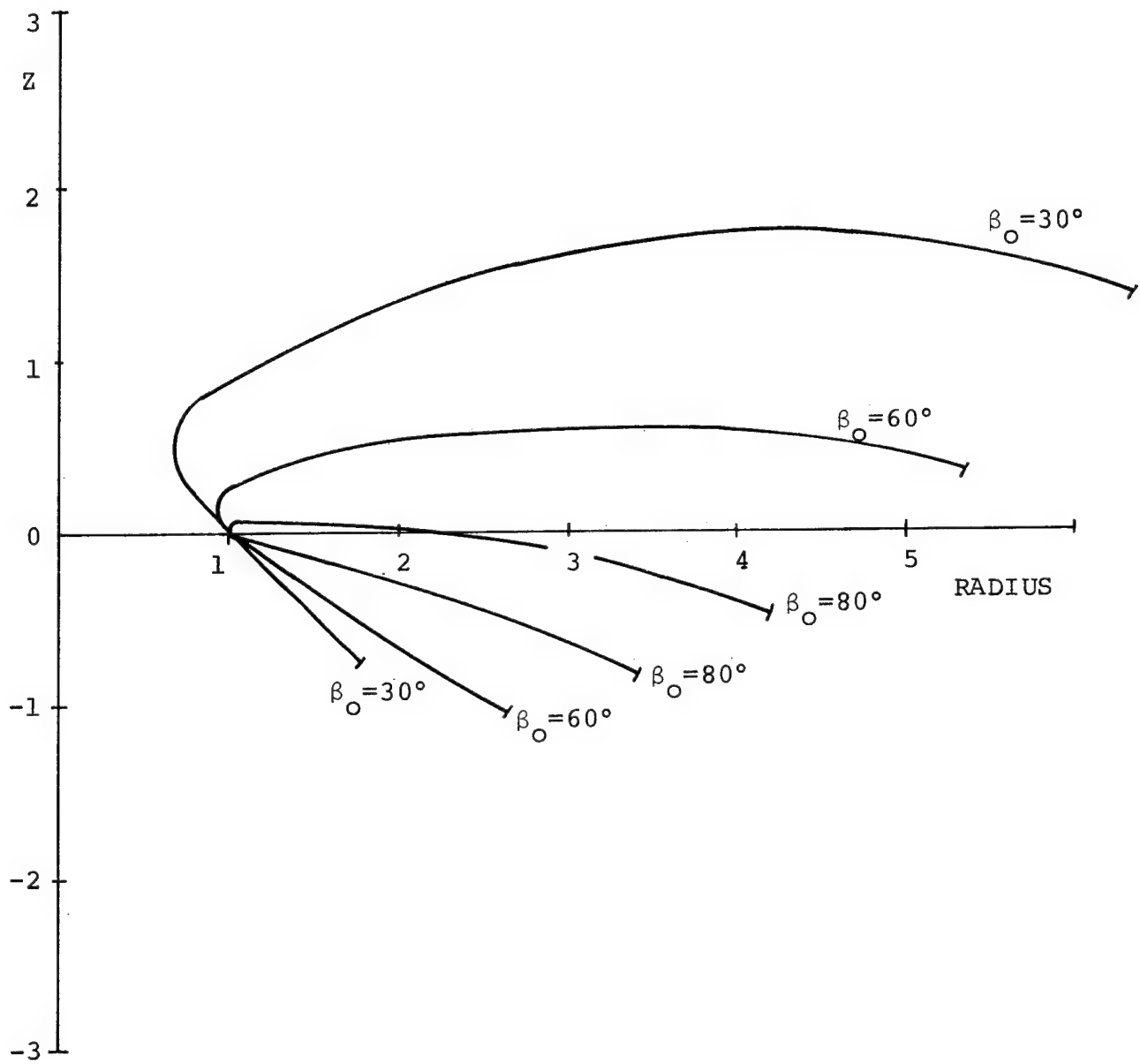
Figure 11c.   Computed Meridional Shapes for Axial
               Load (K = Ω = 0, A ≠ 0)

Isotensoid Shapes for A≠0, Ω=0, K=0
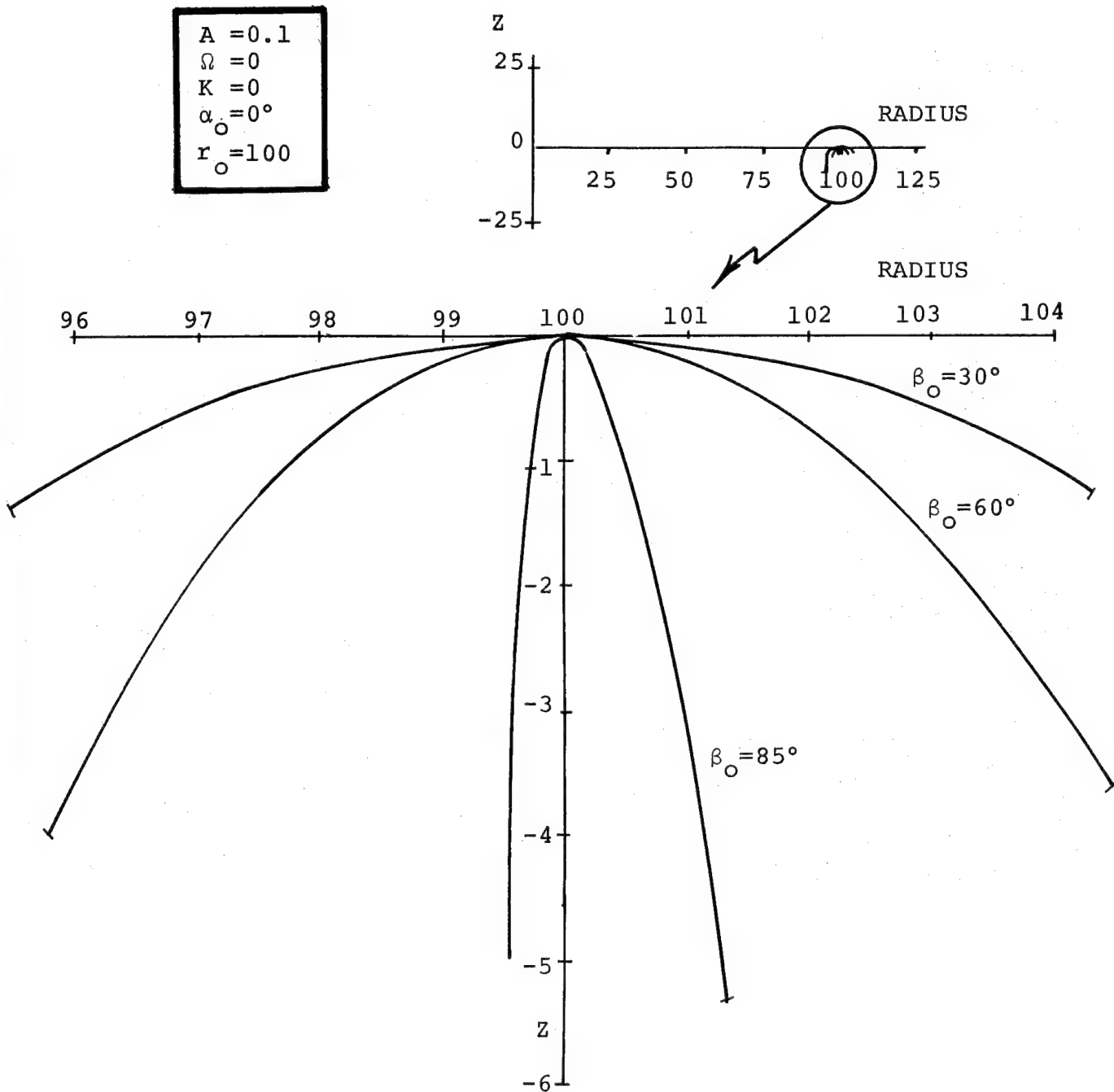
Figure 11d.   Computed Meridional Shapes for Axial
Load (K = Ω = 0, A ≠ 0)
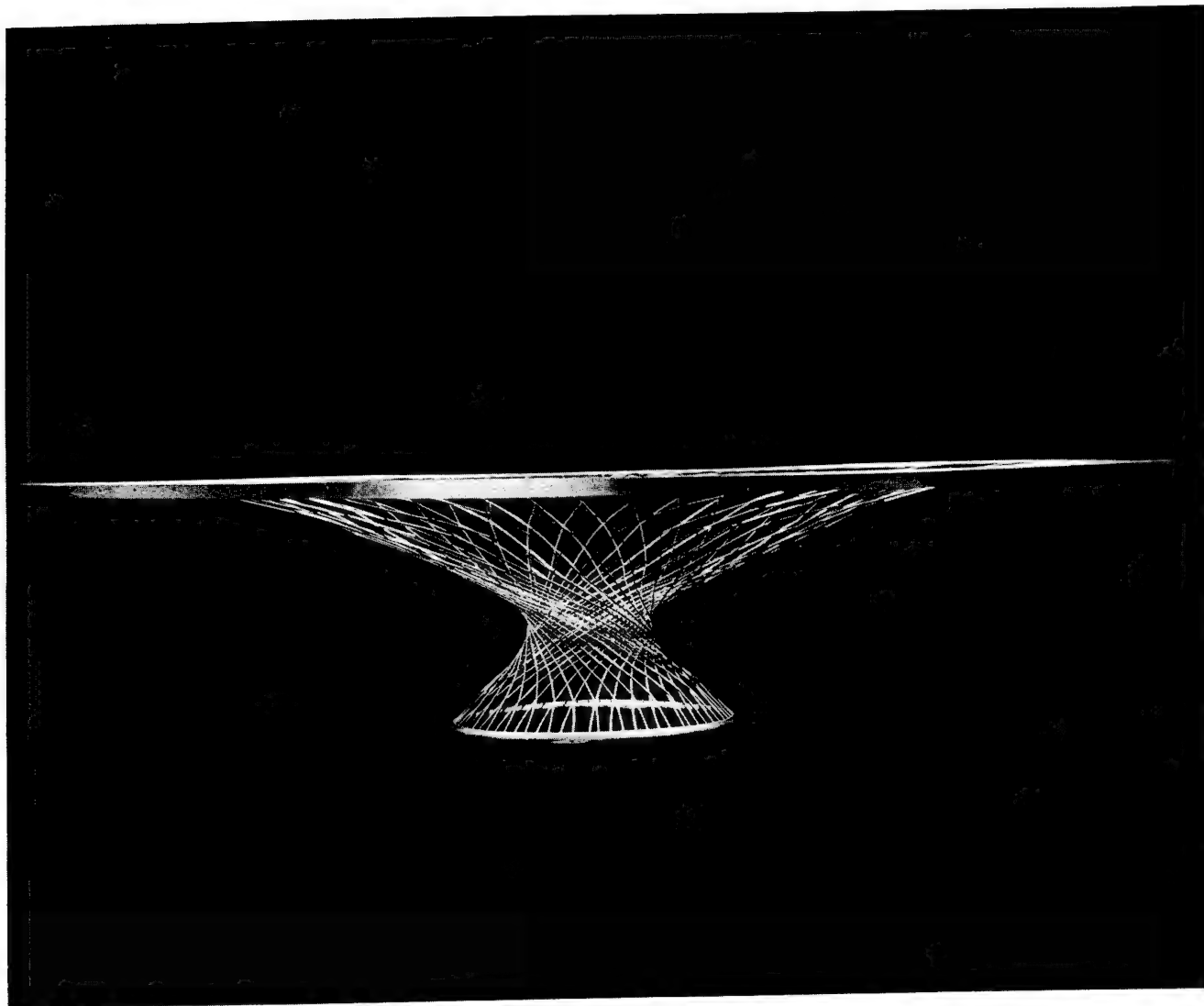
Figure 12.   Cantilever Dish, "Isocompressoid" Structure
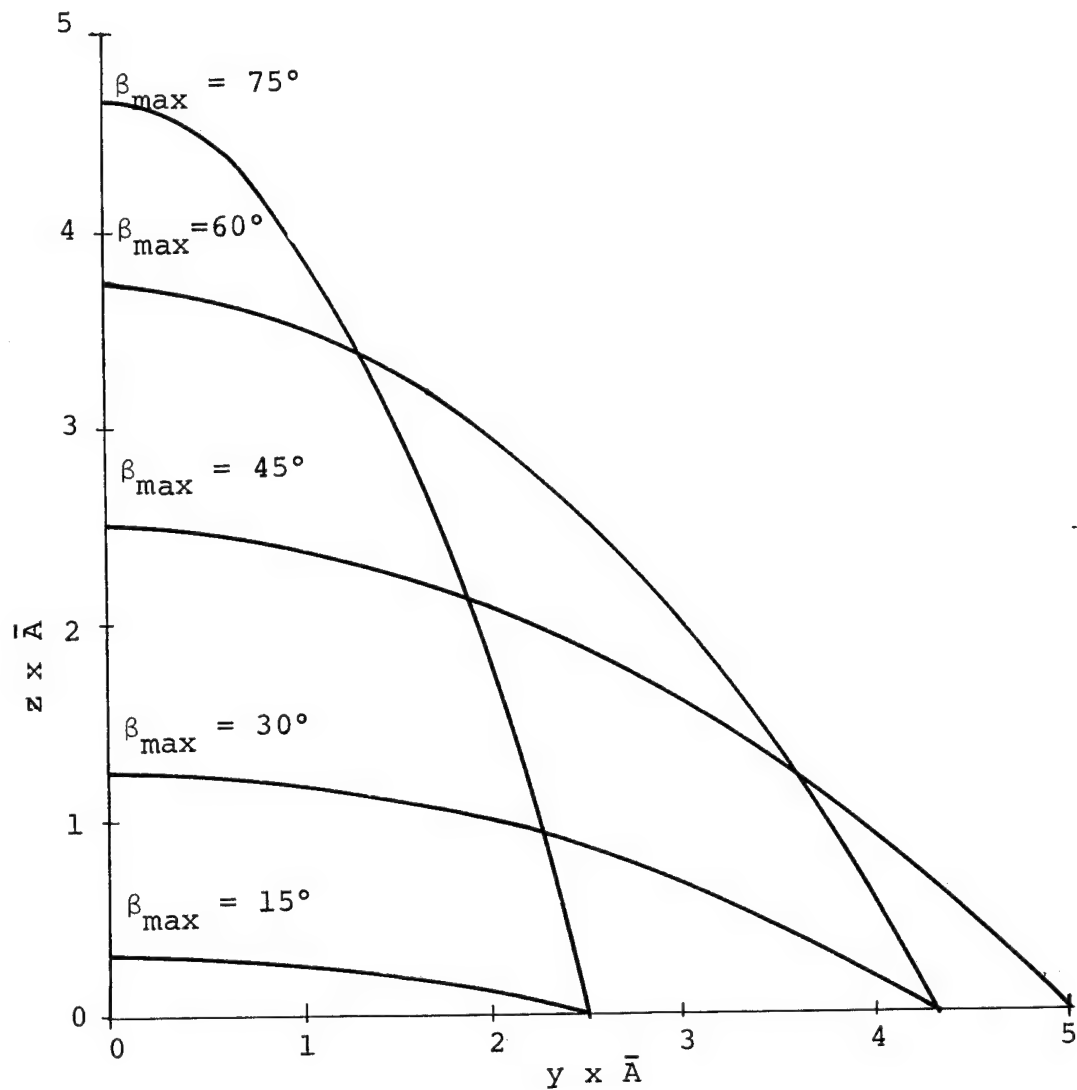
Figure 13a.   Parabolic Shape of Isotensoid
(Isocompressoid) Cylinders
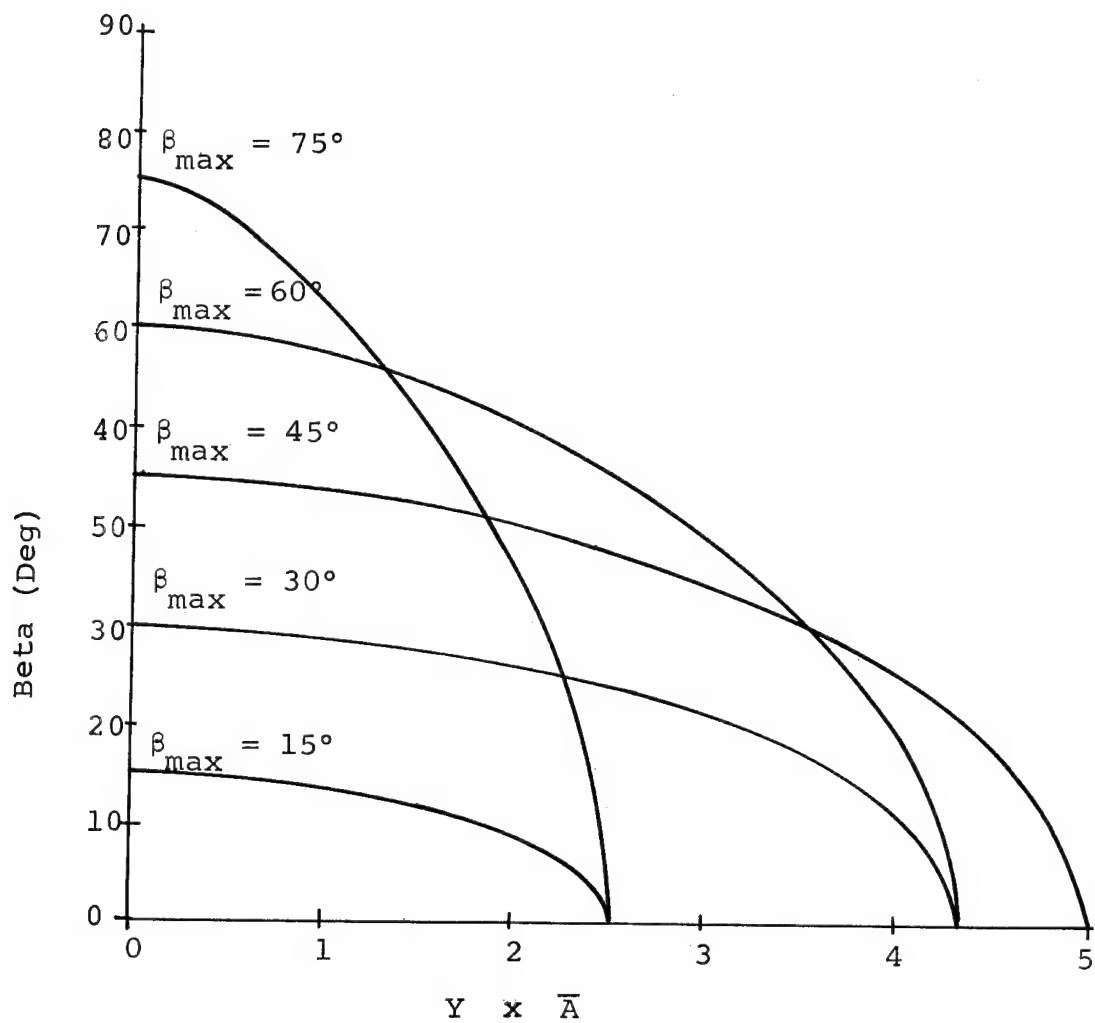
Figure 13b. Variation of Filament Angle β in the Isotensoid (Isocompressoid) Parabolic Cylinders of Figure 12

78
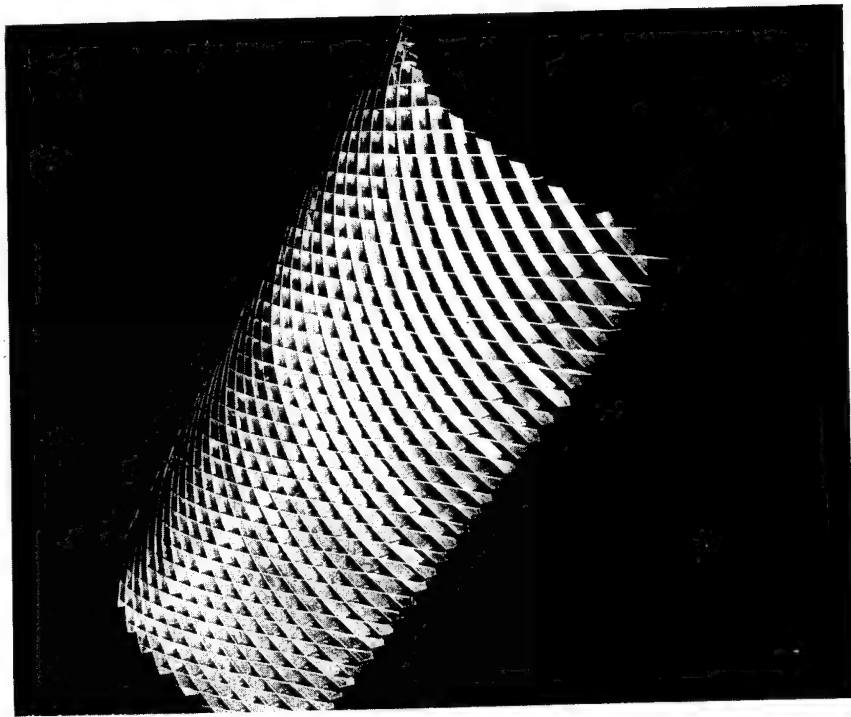
a. Deployed
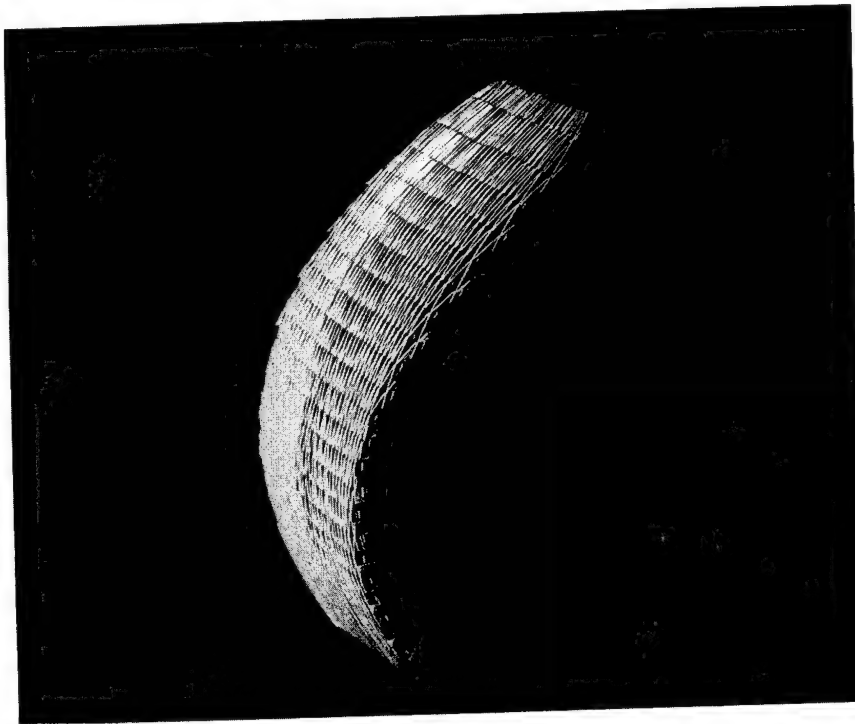
b. Folded

Figure 14. Model of Isotensoid (Isocompressoid) Parabolic Cylinder
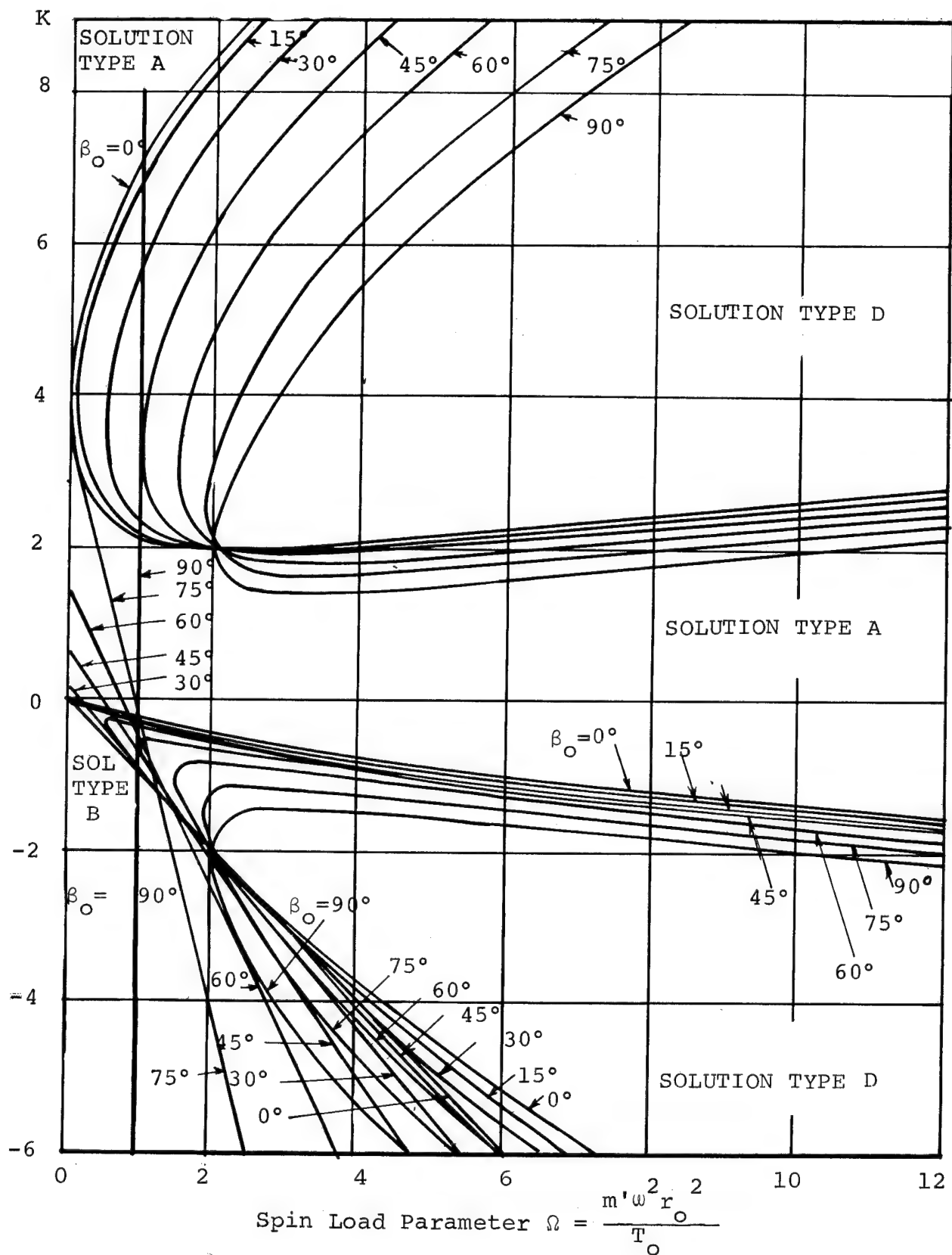
Figure 15. Spinning Isotensoid Network Structures Ranges of Solution Types (With β_o as Parameters)

The figure plots K (vertical axis) versus Spin Load Parameter $\Omega = \dfrac{m'\omega^2 r_o^2}{T_o}$ (horizontal axis). Curve labels include SOLUTION TYPE A, SOLUTION TYPE B, SOLUTION TYPE D, and β_o parameter values of $0°$, $15°$, $30°$, $45°$, $60°$, $75°$, $90°$.
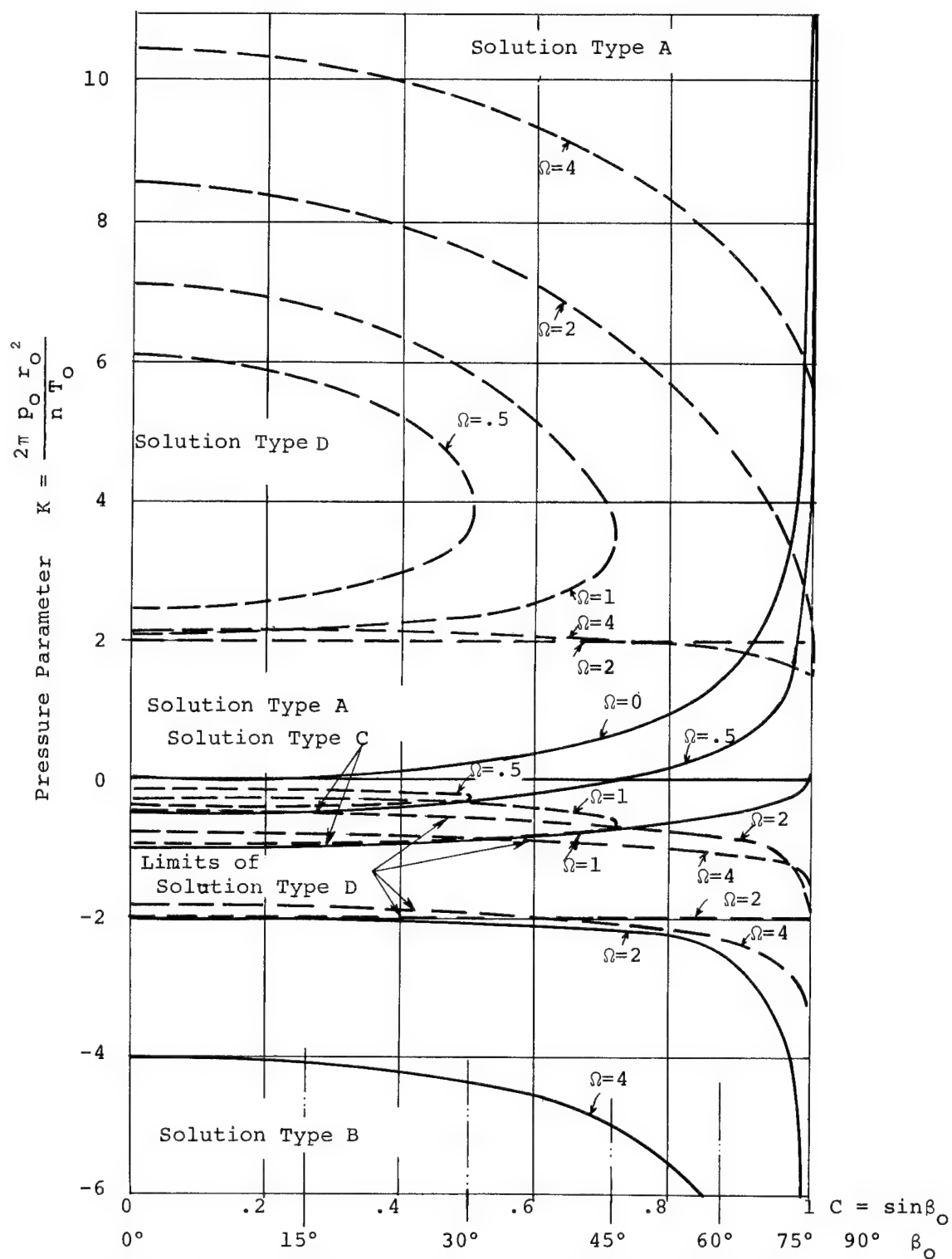
Figure 16.   Spinning Isotensoid Network Structures
Ranges of Solution Types (With Ω as
Parameters)
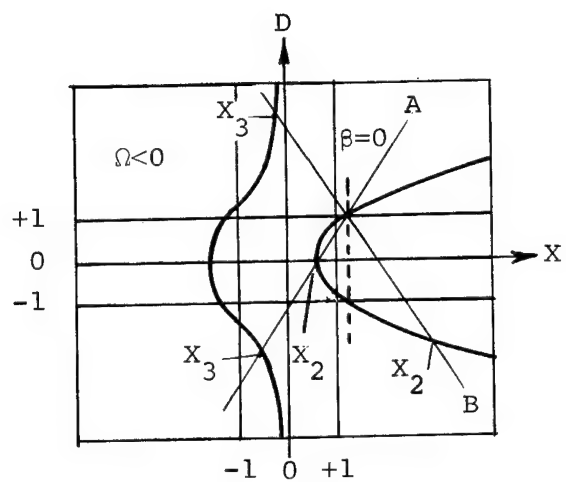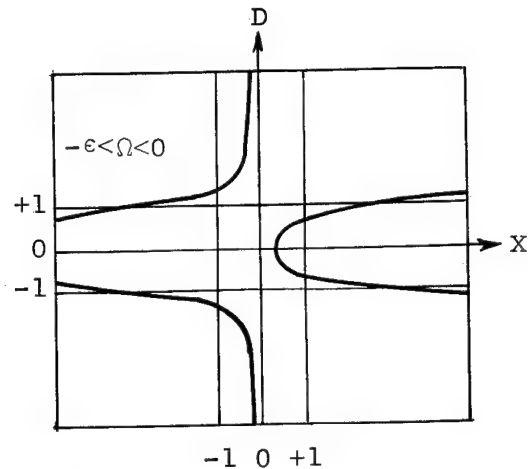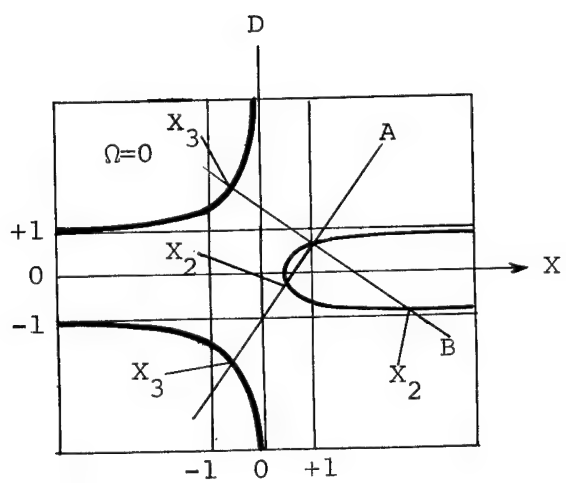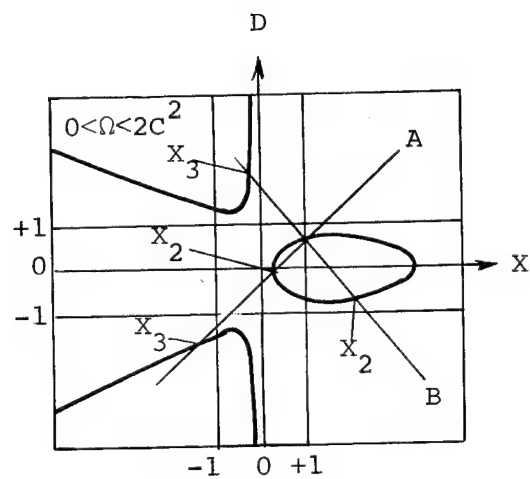
Figure 17. Typical Sketches of D for Different Regions of Ω

82
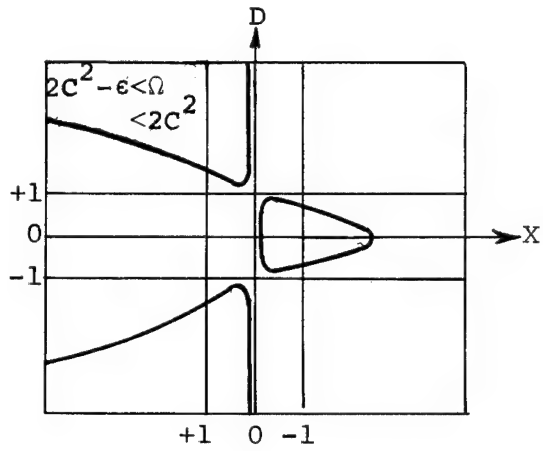
(e)
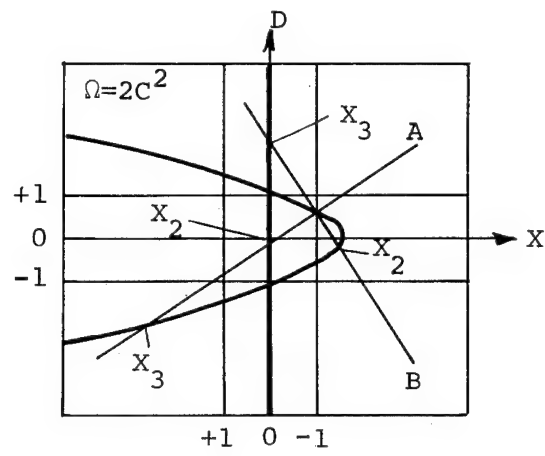
(f)

(g)

(h)

(i)

Figure 17 (continued)

83

Figure 18.   Composite Sketch of D   for All Regions of   Ω
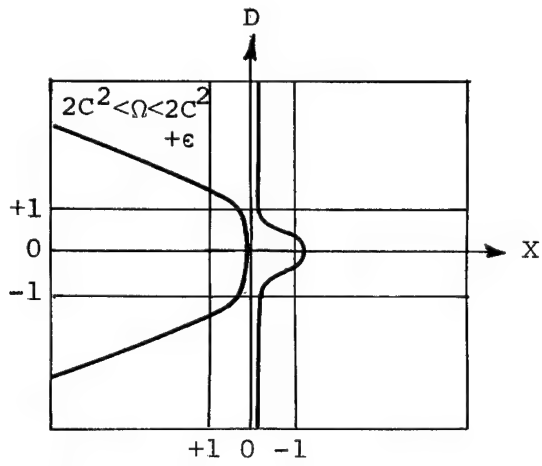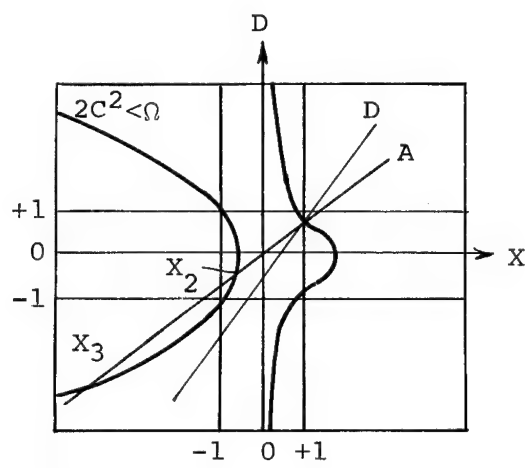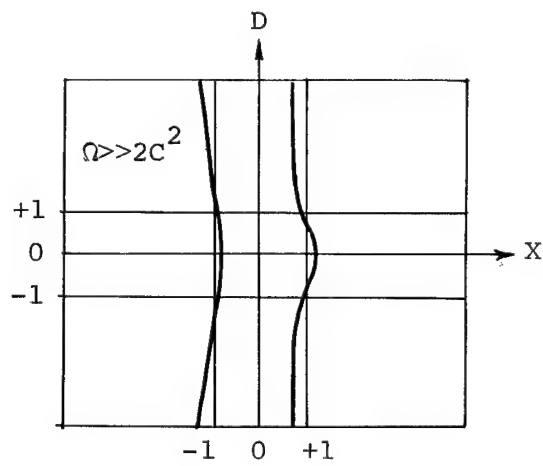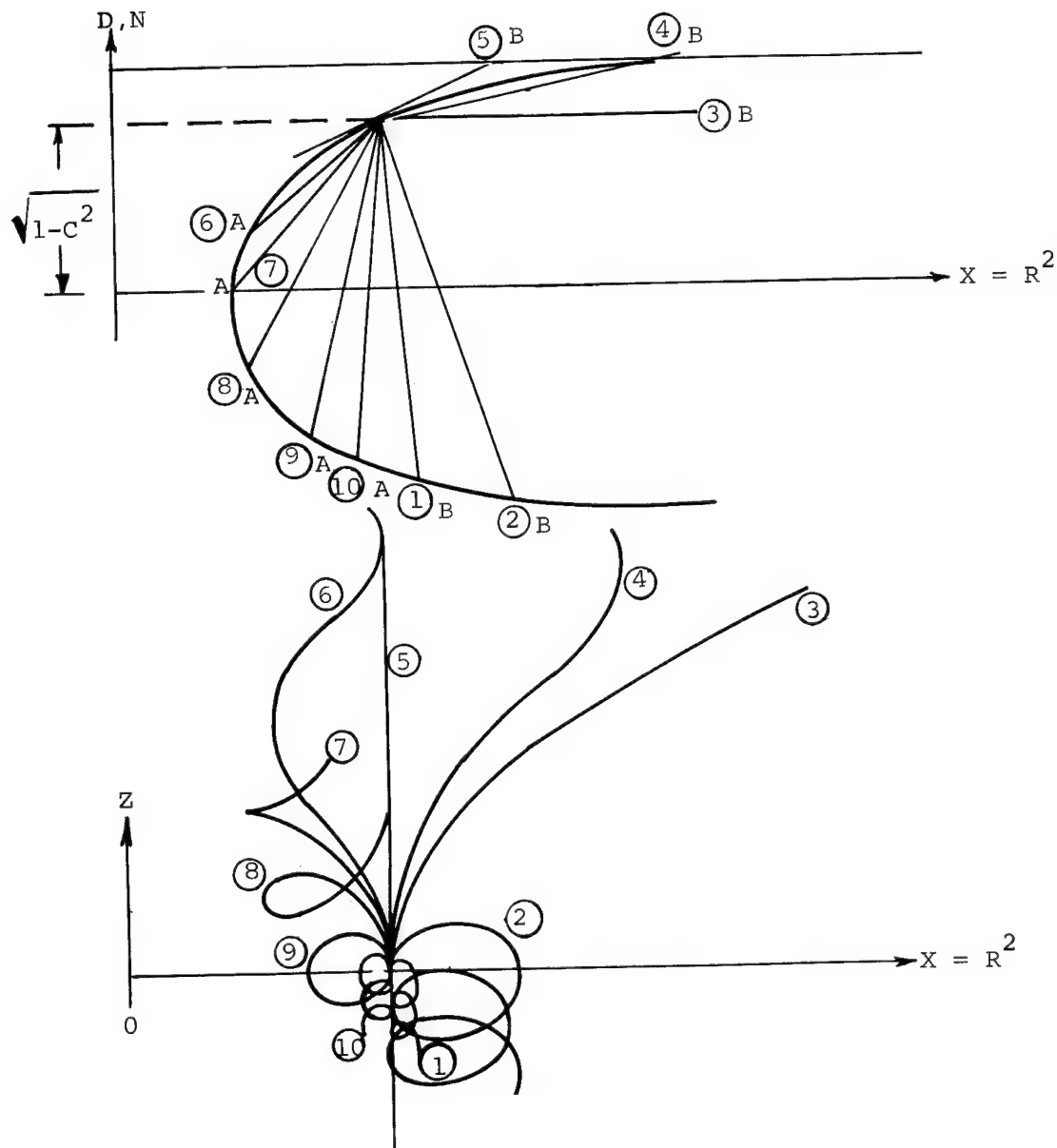
Figure 19a. Isotensoid Meridional Profiles for Boundary Case 1

$$A = 0 \quad K \neq 0 \quad \Omega = 0$$

85
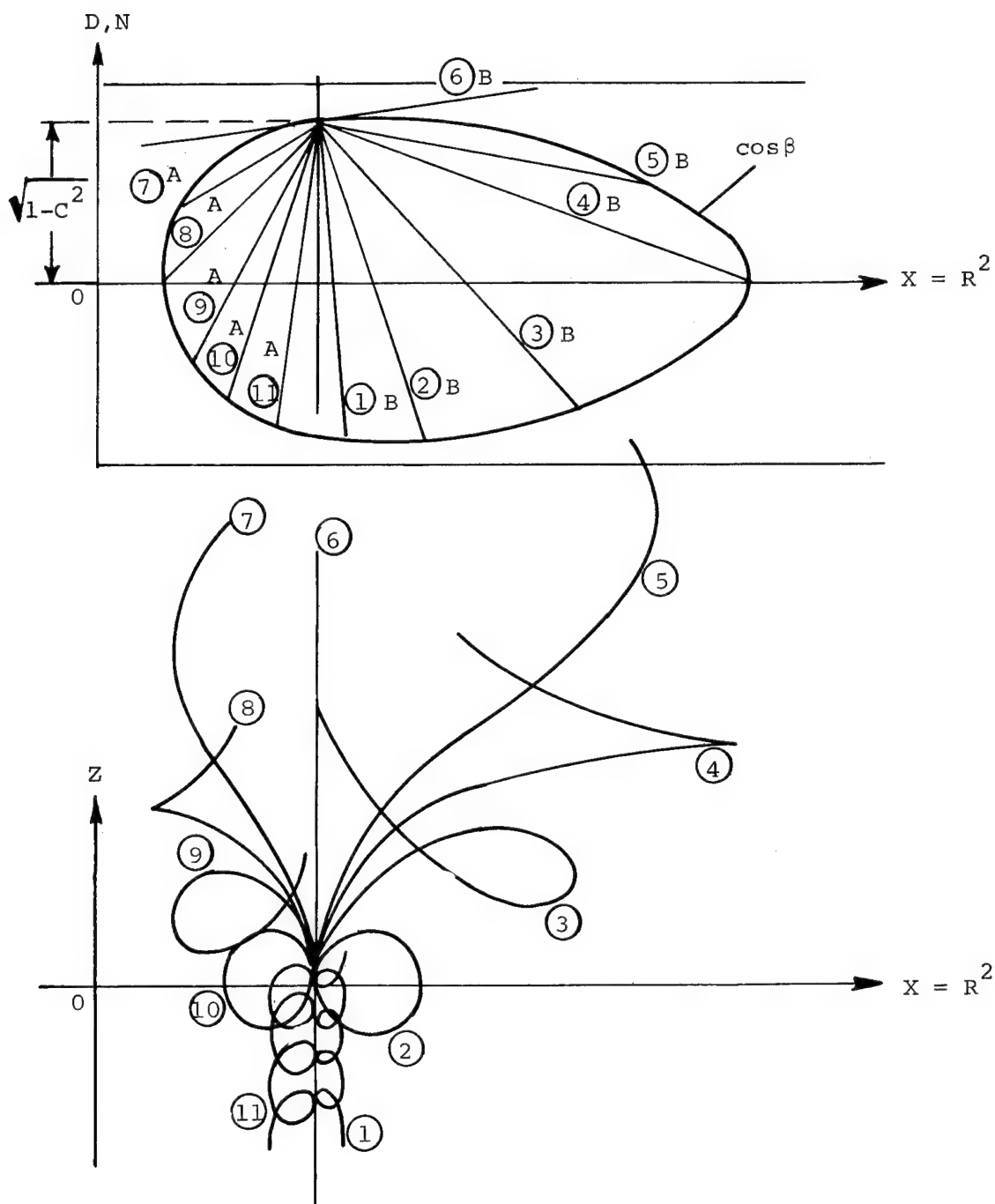
Figure 19b.   Isotensoid Meridional Profiles for Region 2
$A = 0$ $K \neq 0$ $0 < \Omega < 2c^2$
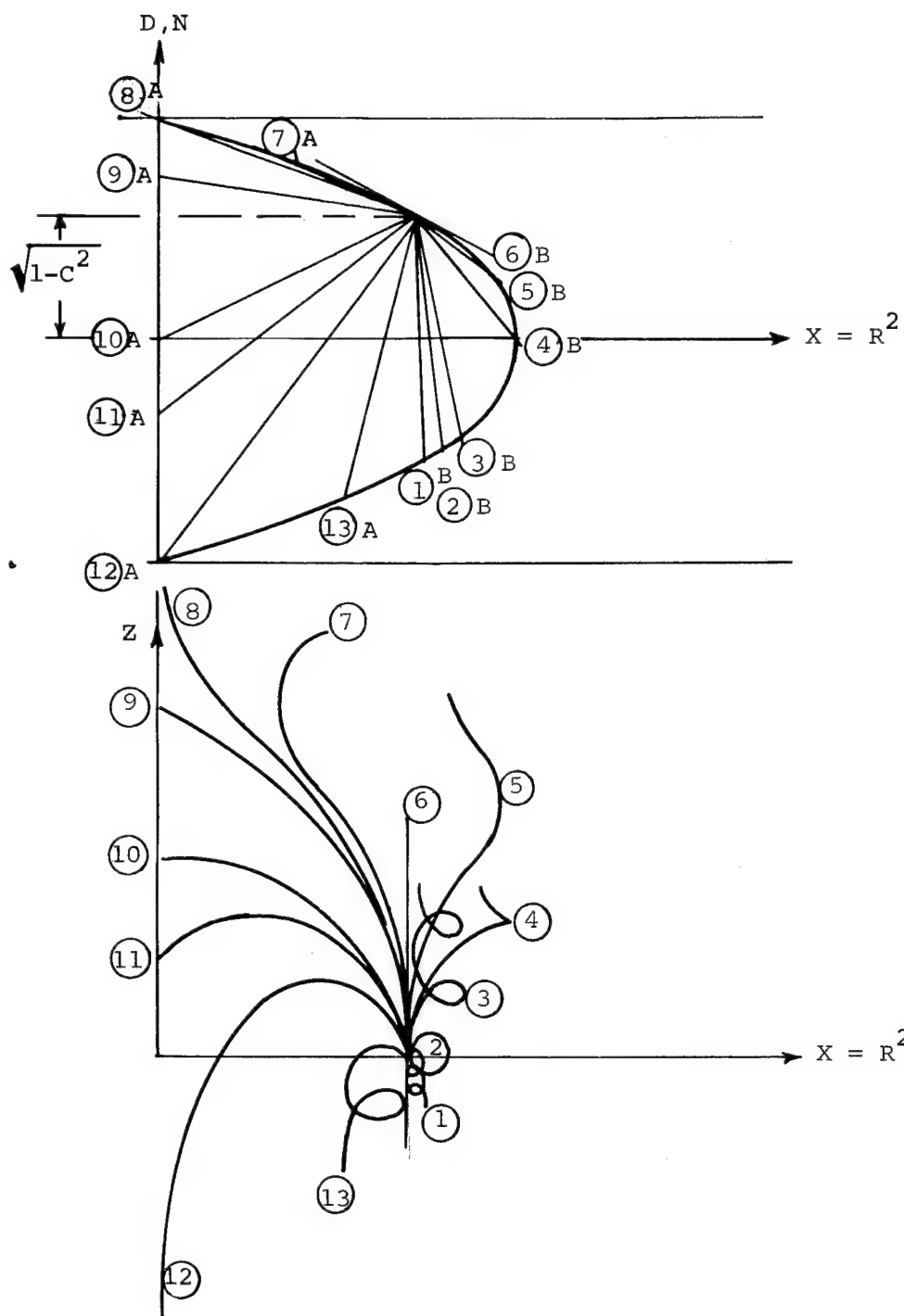
Figure 19c. Isotensoid Meridional Profiles for Boundary Case 2

$$A = 0 \quad K \neq 0 \quad \Omega = 2c^2$$

87
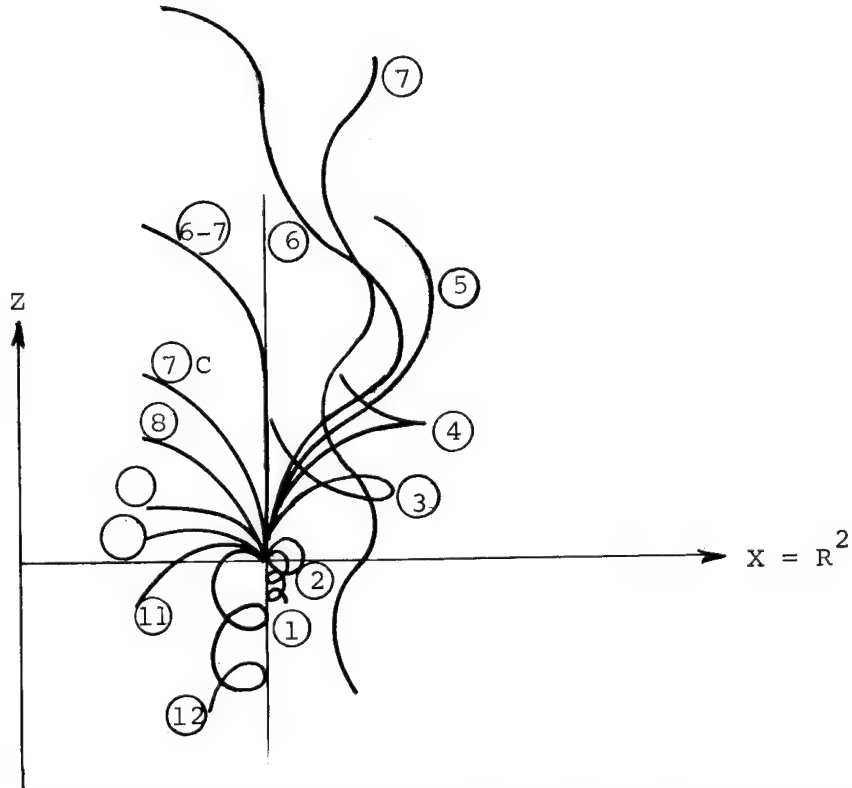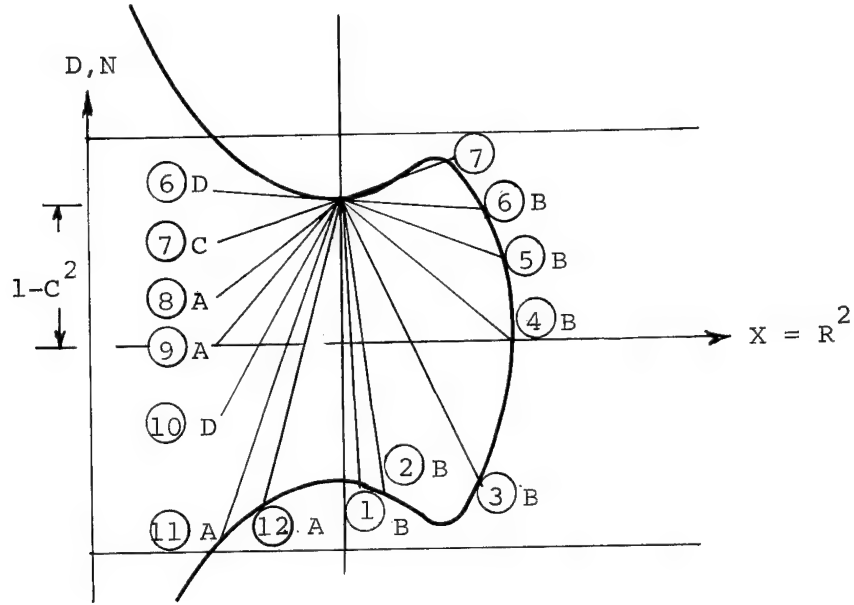
Figure 19d.   Isotensoid Meridional Profiles for Special Case 1 of
Region 3 $2c^2 < \Omega < 2$, $c^2 < 1/3$
$$1 - \sqrt{1-4c^2 + 3c^4} < \Omega < 1 + \sqrt{1-4c^2 + 3c^4}$$
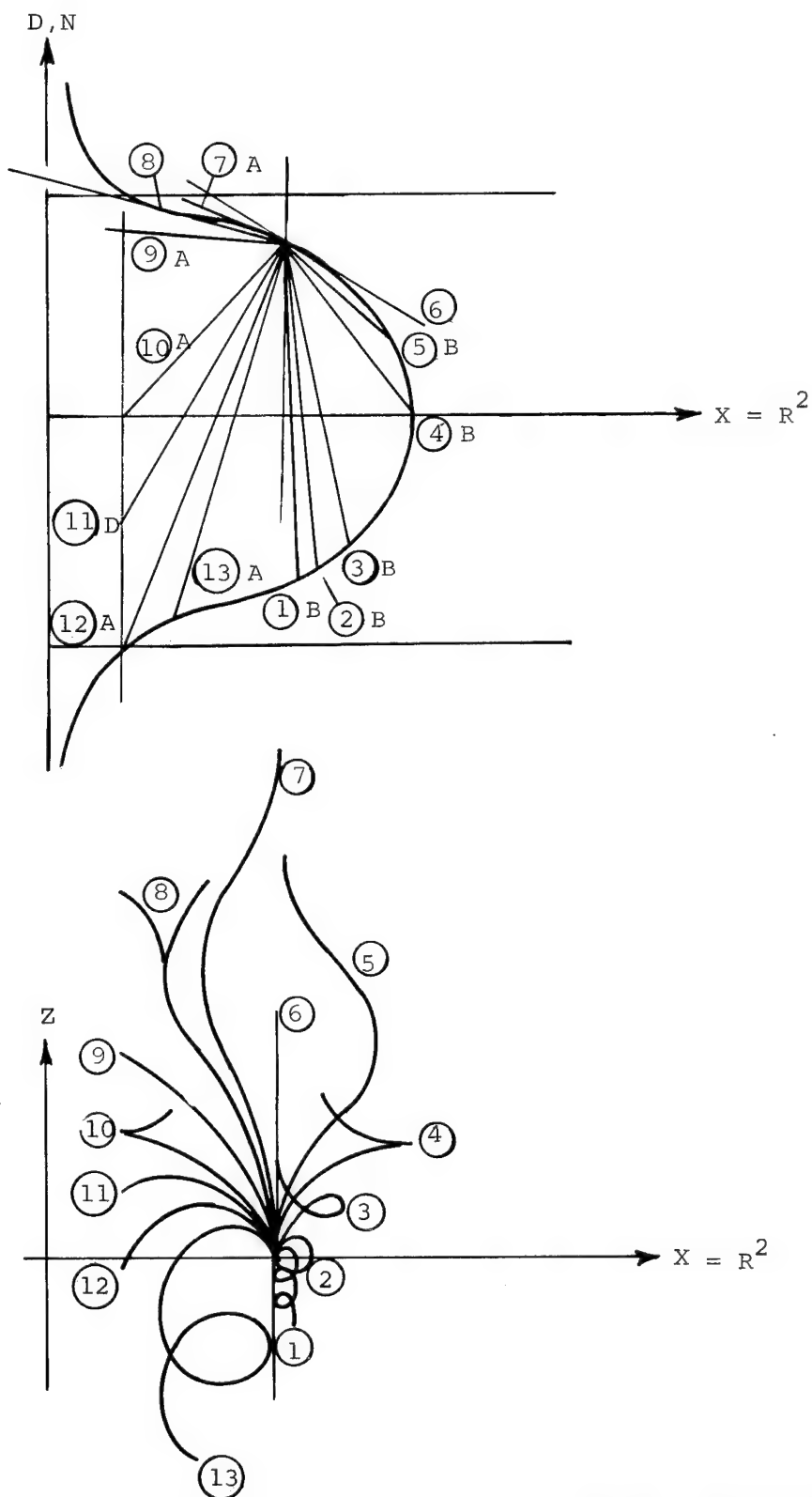
Figure 19e. Isotensoid Meridional Profiles for Special Case 2 of Region 3 $2c^2 < \Omega < 2, \quad 1 > c^2 > 1/3$

89
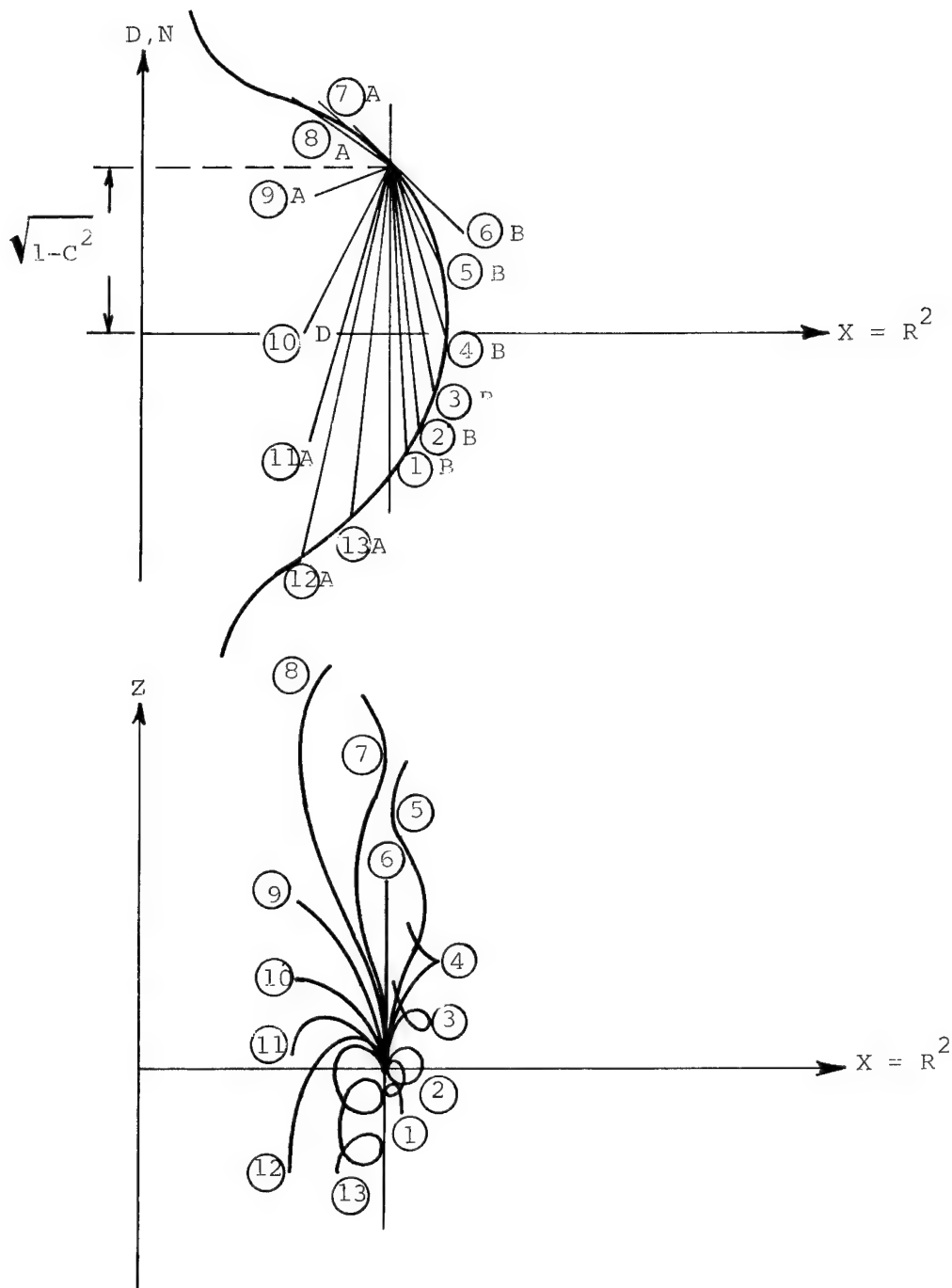
Figure 19f. Isotensoid Meridional Profiles for Special Case 3 of
Region 3   A = 0   K ≠ 0   Ω = 2
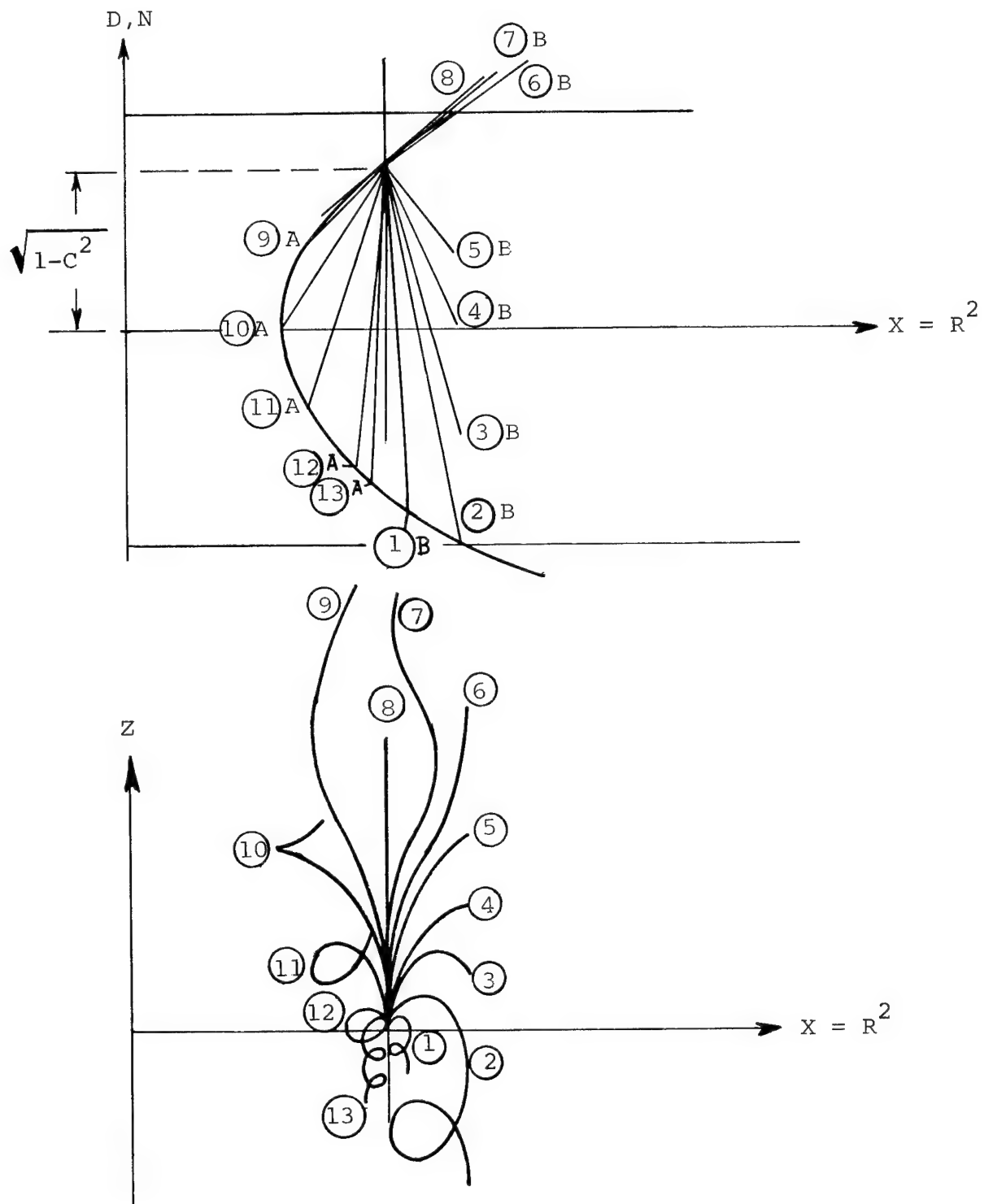
Figure 19g. Isocompressoid Meridional Profiles for Region 1

$$A = 0 \quad K \neq 0 \quad \Omega < 0$$

91

$$K=1; \quad C=\frac{\sqrt{3}}{2} \; ; \; r_{min}=0; \quad (\sin\beta)_{r_{min}}=1; \quad \Omega=1.5$$

$60°$
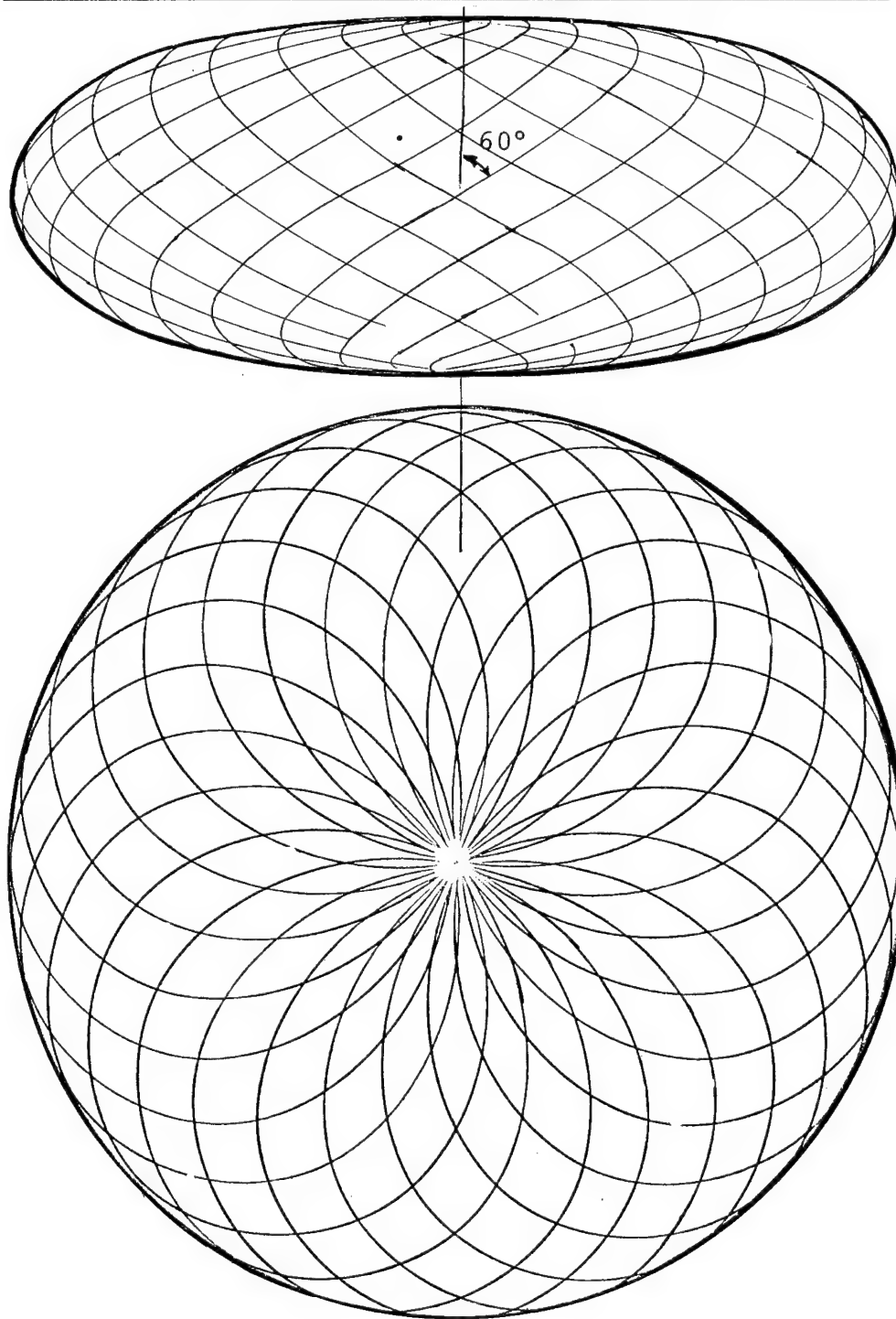
Figure 20.   Spinning Isotensoid Pressure Vessel
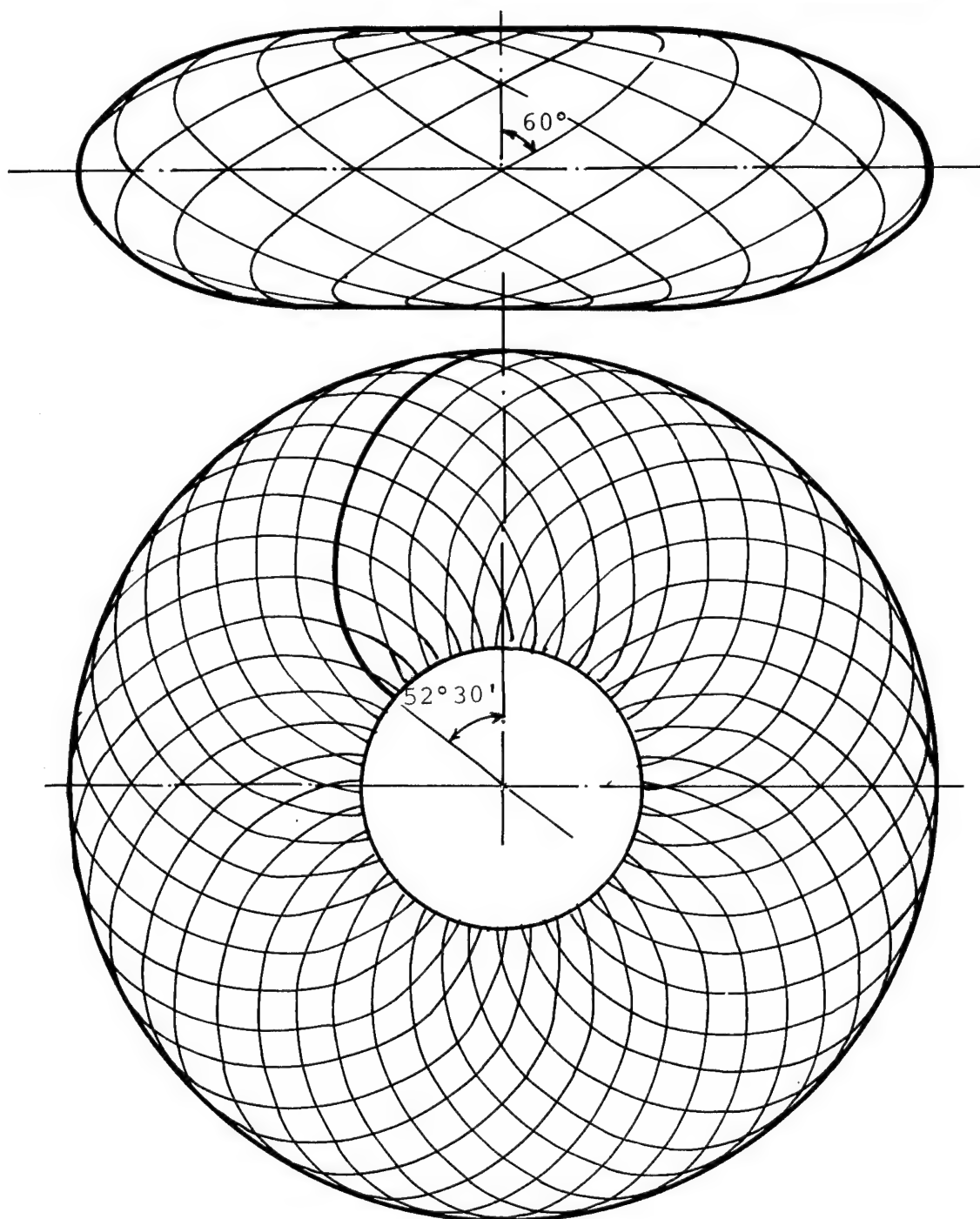
Figure 21. Spinning Isotensoid "Tire" Fibers
Radial At Hub

93

$$K=1.125; \quad C=\frac{\sqrt{3}}{2}; \quad r_{min/r_o}=1/3; \quad (\sin\beta)_{r_{min}}=1; \quad \Omega=1.313$$
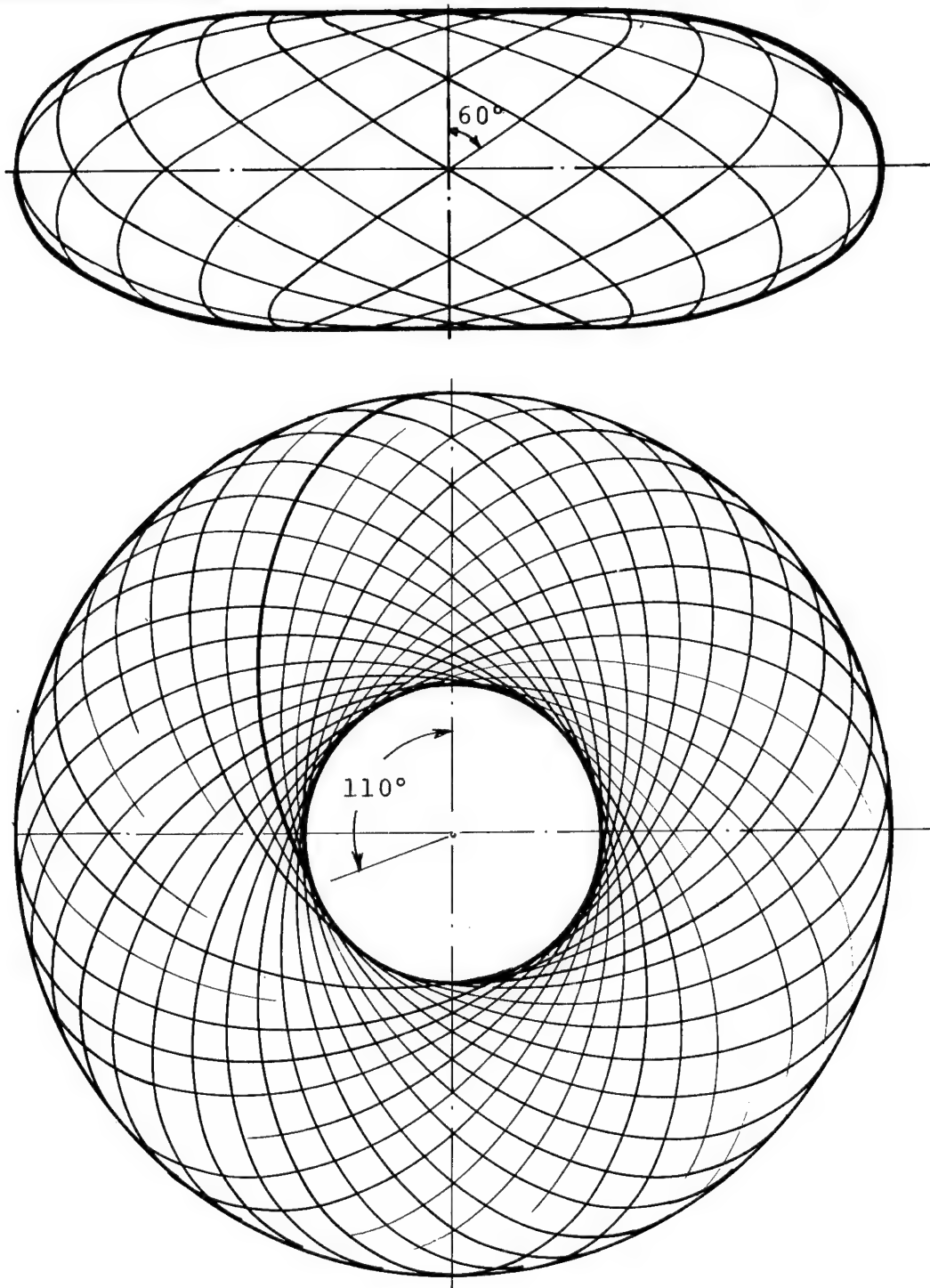
Figure 22.   Spinning Isotensoid "Tire" Fibers
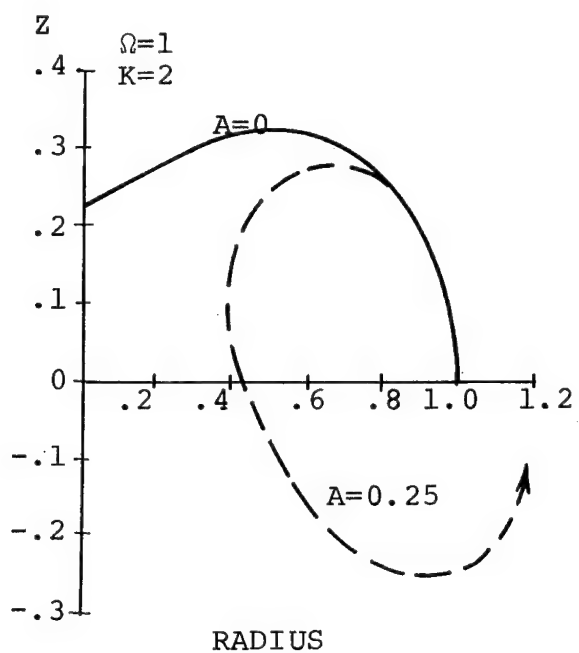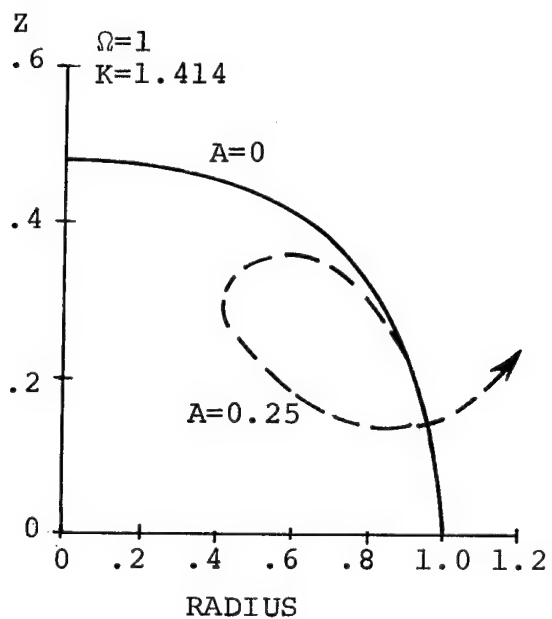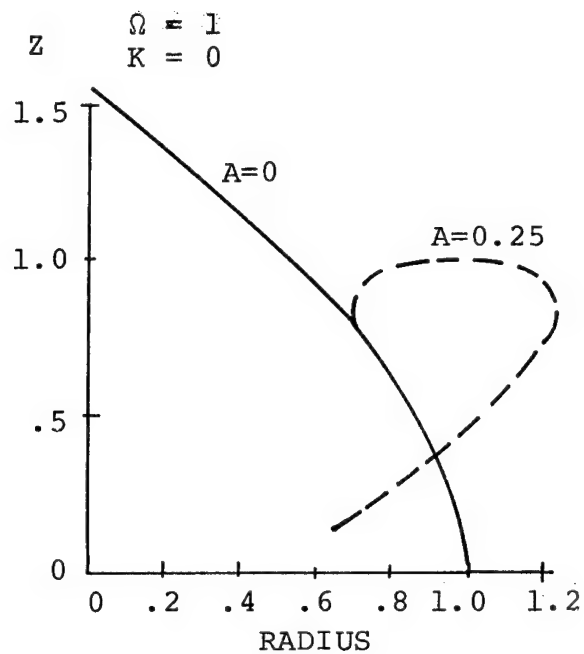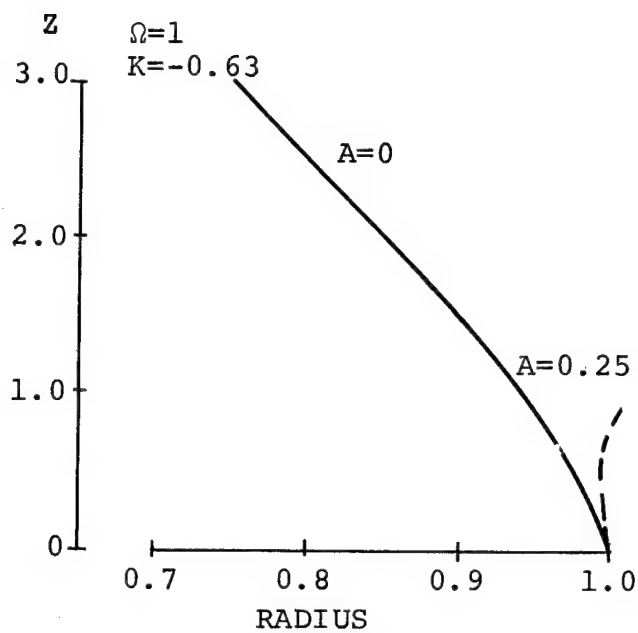Tangential   To Hub

94
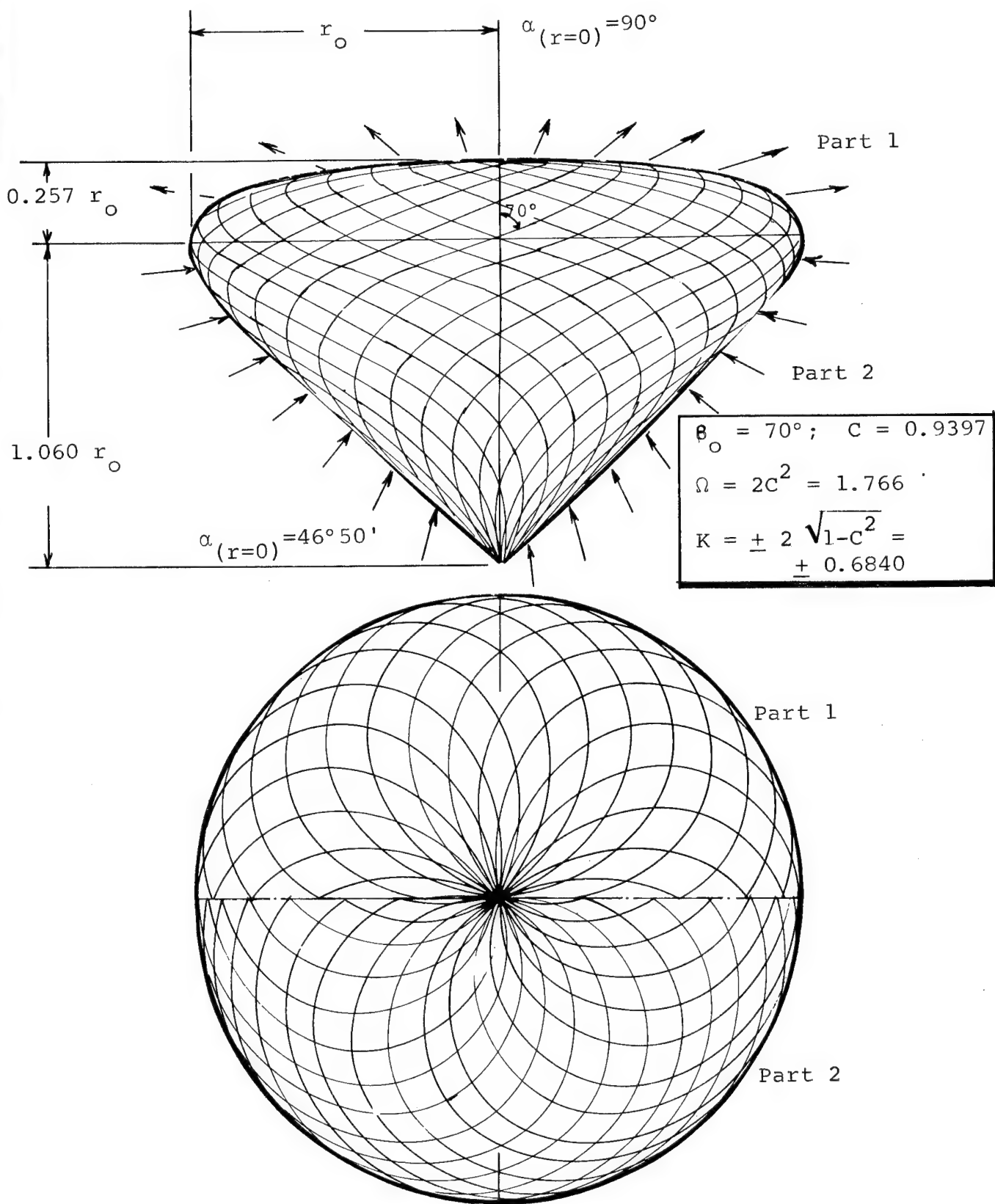
Figure 23. Spinning Isotensoid Net Loaded with Discontinuous Pressure Profile
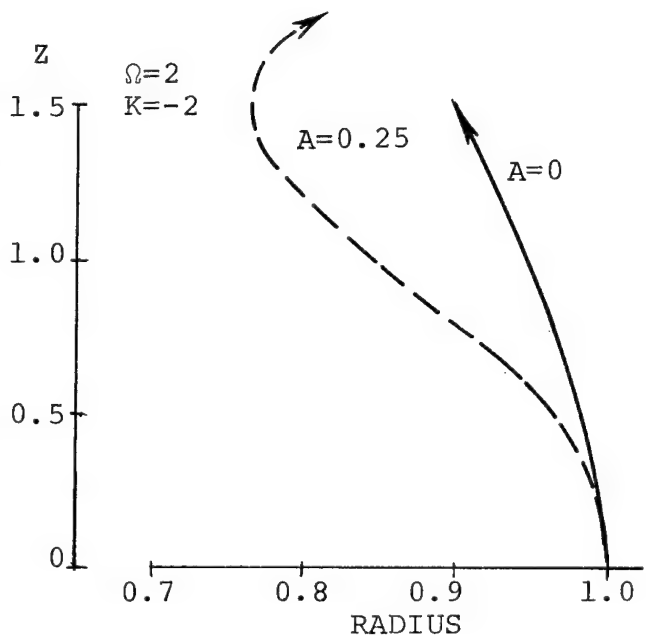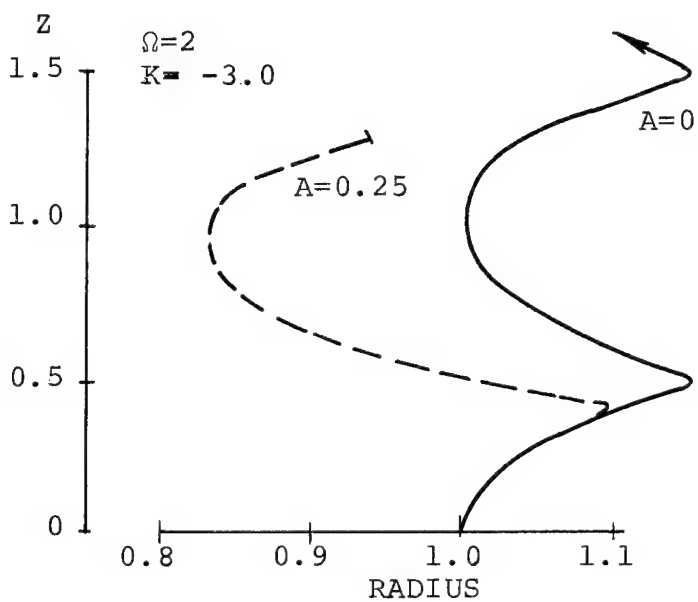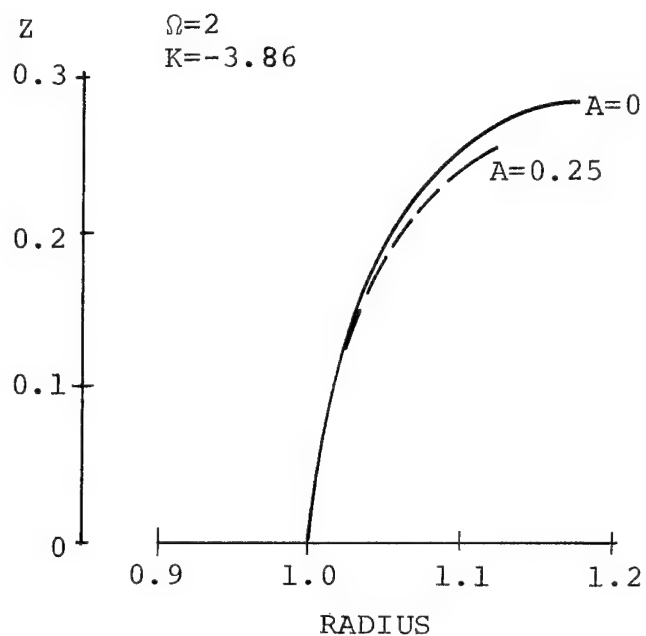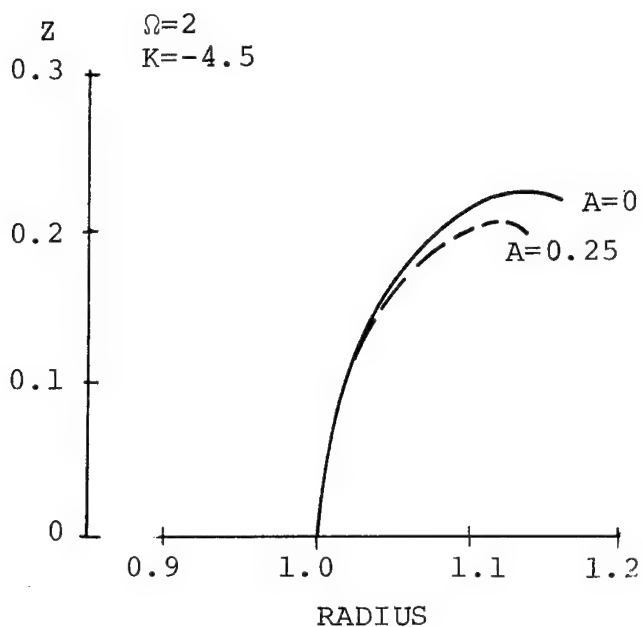
95

Figures 24.   Computed Meridional Shapes for Cases 4 and
5. $\alpha_o = 0°$, $\beta_o = 45°$, Load Parameters as
Indicated ($\Omega > 2c^2$)
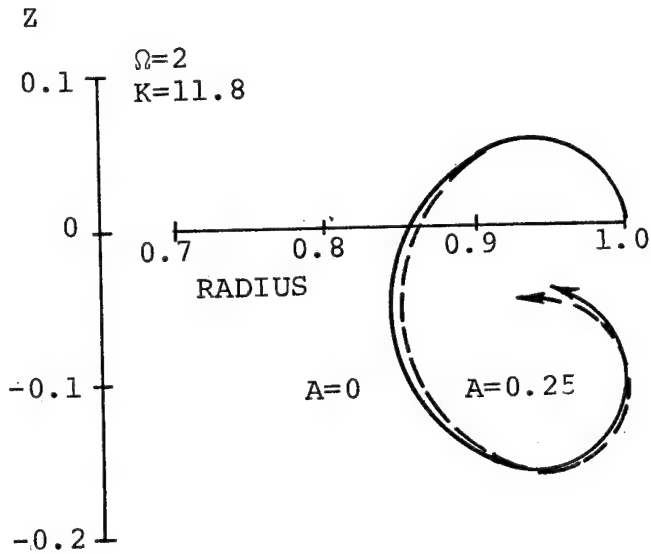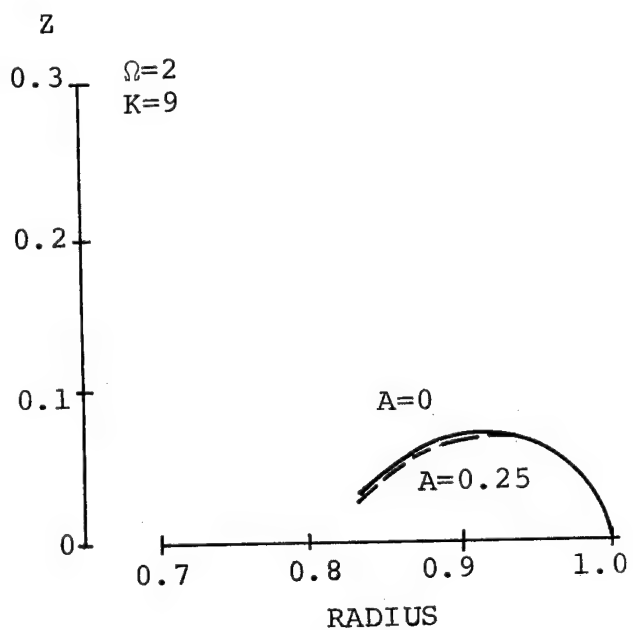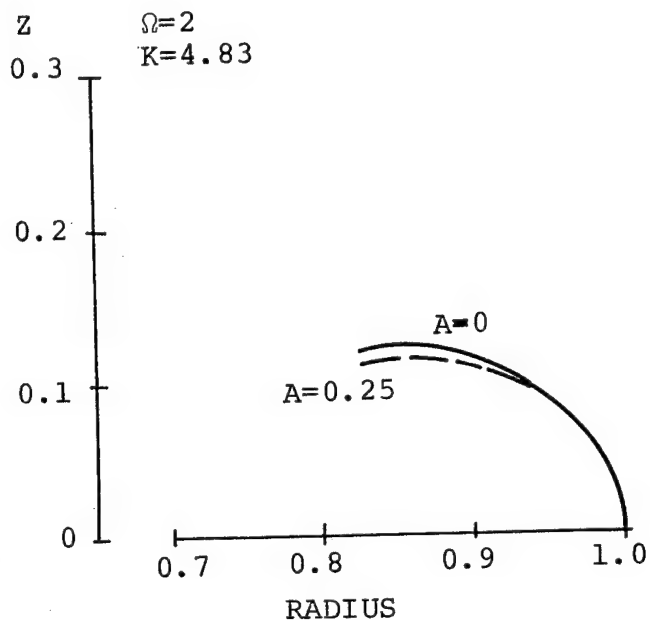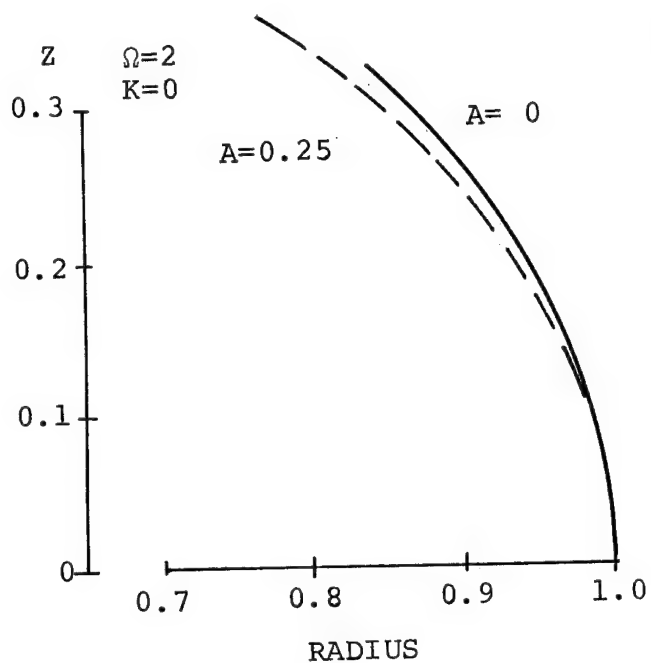
Figures 24.   Computed Meridional Shapes for Cases 4 and
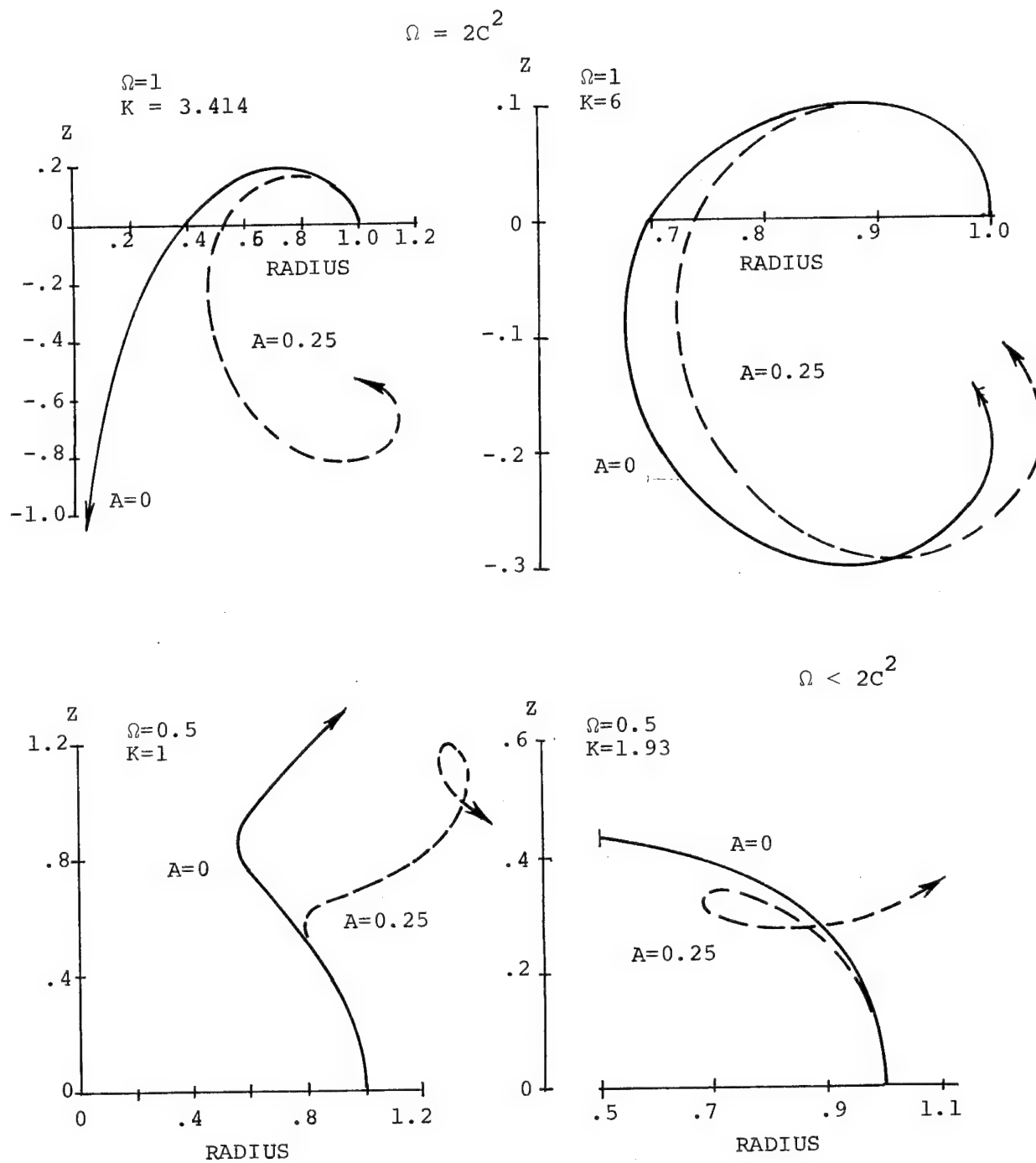5. $\alpha_o = 0°$, $\beta_o = 45°$, Load Parameters as
Indicated $(2 > 2C^2)$

Figures 24.   Computed Meridional Shapes for Cases 4 and
5. $\alpha_o = 0°$, $\beta_o = 45°$, Load Parameters as
Indicated $(\Omega = 2c^2)$

Figures 24.   Computed Meridional Shapes for Cases 4 and 5.
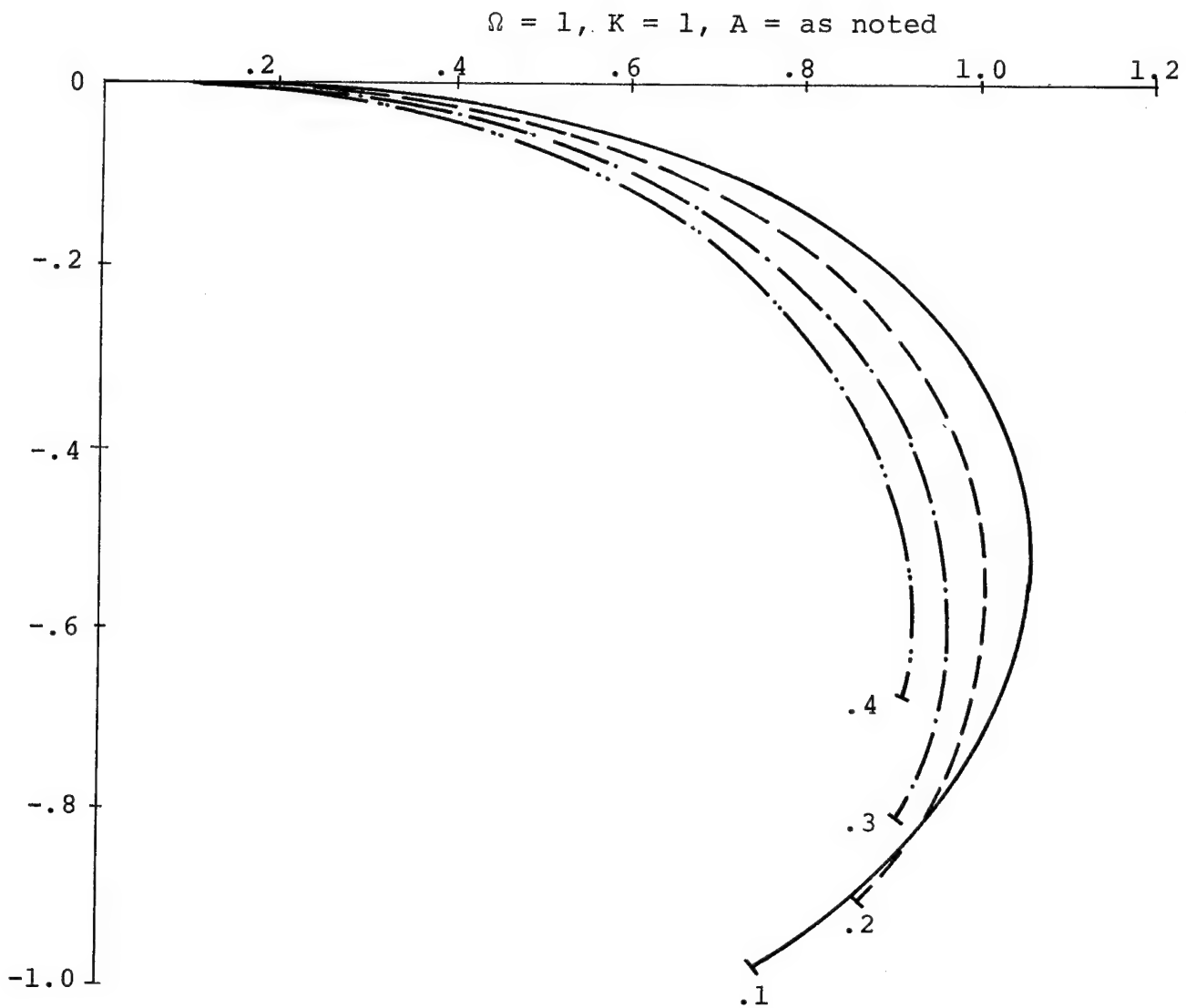$\alpha_o = 0°$, $\beta_o = 45°$, Load Parameters as Indicated

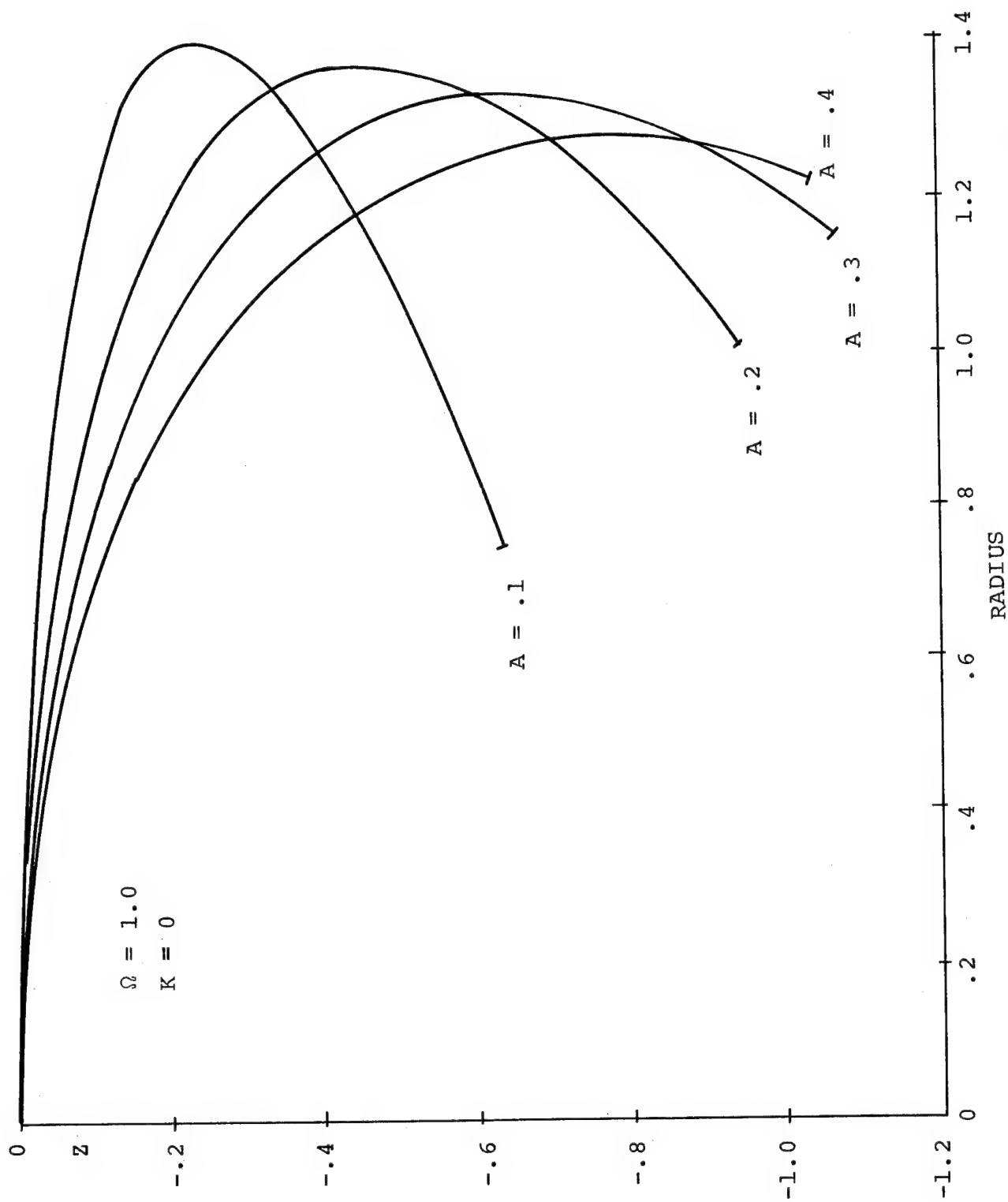Figure 25. Computed Isotensoid Shapes, Closed at Center. Loads as Indicated

Figure 26. Computed Isotensoid Shapes With Spin and Axial Load, Closed at Center
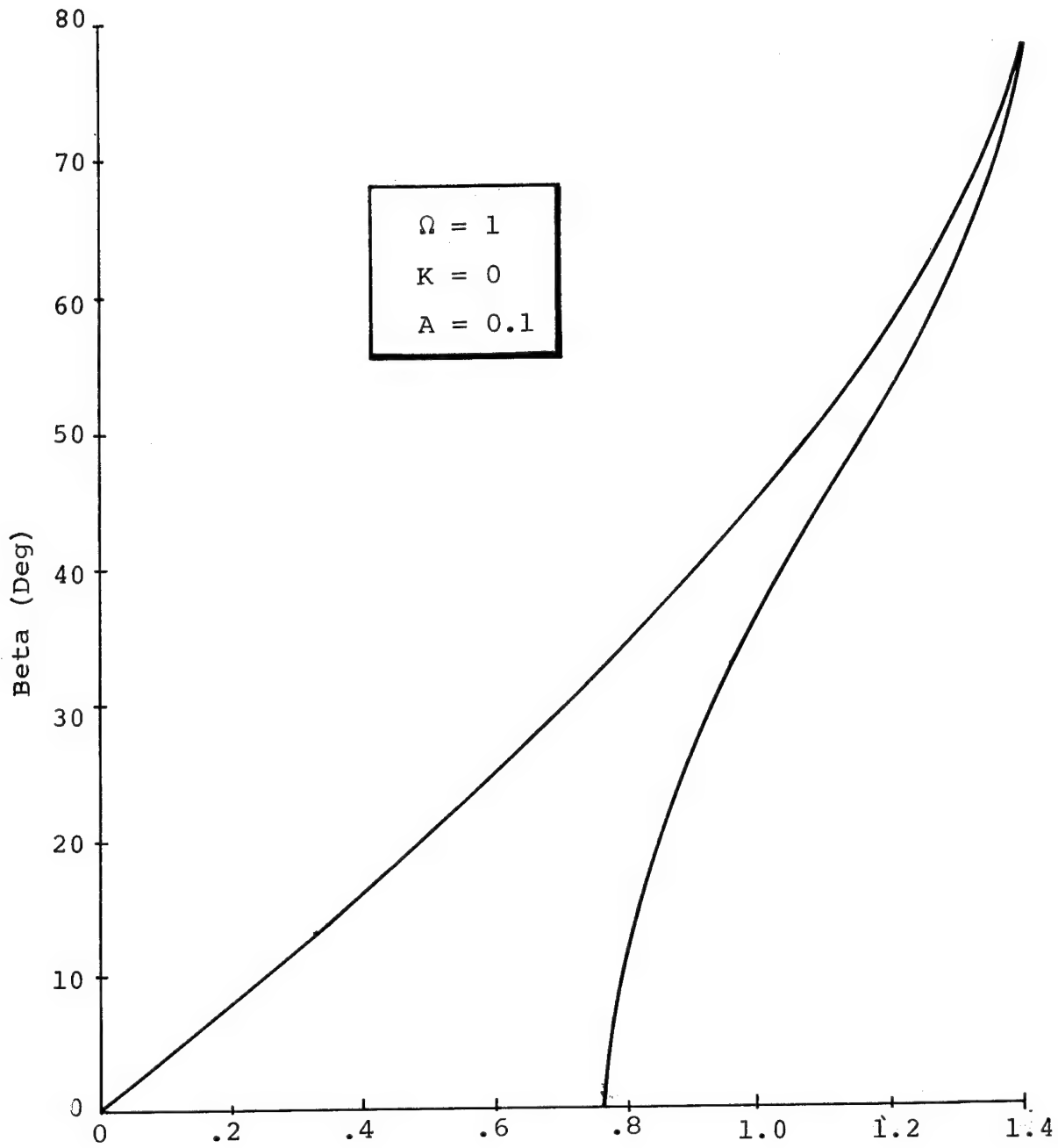
101

Figure 27.   Fiber Angle for Typical Shape of Figure 25

APPENDIX

NUMERICAL INTEGRATION OF GOVERNING EQUATIONS

The most convenient form of the governing equations for numerical integration are the equation sets (39), (40), and (18), or (41), (42), and (44). They read (for uniform pressure):

$$\frac{d\alpha}{dR} = -K \, R \, \csc\alpha \, \sec\beta - \Omega \, R \, \text{ctn}\alpha \, \sec^2\beta - A \, \sec^2\beta + \tan^2\beta \, \text{ctn}\alpha \, R^{-1}$$

$$\frac{d\beta}{dR} = \Omega \, R \, \csc\beta \, \sec\beta - A \, \text{ctn}\alpha \, \csc\beta \, \sec\beta - \tan\beta \, R^{-1} \qquad \left.\right\} \text{(A-1)}$$

$$\frac{dZ}{dR} = -\text{ctn}\alpha$$

$$\frac{d\alpha}{dZ} = K \, R \, \sec\alpha \, \sec\beta + \Omega \, R \, \sec^2\beta + A \, \tan\beta \, \sec^2\beta - \tan^2\beta \, R^{-1}$$

$$\frac{d\beta}{dZ} = -\Omega \, R \, \tan\alpha \, \csc\beta \, \sec\beta + A \, \csc\beta \, \sec\beta + \tan\beta \, \tan\alpha \, R^{-1} \qquad \left.\right\} \text{(A-2)}$$

$$\frac{dR}{dZ} = -\tan\alpha$$

A digital computer program was written for use in integrating equation sets (A-1) and (A-2) using a second order Runge-Kutta method. The program listing is given at the end of this appendix. In using this program to determine the surface profile $Z(R)$, the load parameters K, Ω, A and initial values for α, β, and R and Z are selected. The program can be then applied for either increasing or decreasing increments of Z and R. If α approaches zero, equations (A-2) must be used because of the $\text{ctn}\alpha$ term in (A-1), while if α approaches $\pi/2$, Equations (A-1) must be used because of the $\tan\alpha$ term in (A-2). In transferring from one equation set to another in the middle of a run, the last print out from the computations using one set

of equations is used for initial conditions in the other set of equations. In this manner, surfaces which go through 0, $\pi/2$ and cyclic increases of these angles can be determined.

For surfaces which approach $R = 0$, neither set of equations is satisfactory for digital computation near $R = 0$ because of the appearance of R^{-1} in both equation sets. In order to remedy this situation, Equations (A-1) were examined for limiting restrictions as $R \rightarrow 0$. These were chosen in preference to Equations (A-2) because, as will be shown, α must approach $\pi/2$ and dR/dZ therefore becomes unbounded.

Limit when $R \rightarrow 0$. - From the first two of Equations (A-1) it is apparent that $\tan\beta$ must approach zero with at least the first power of R. For the special case $A = 0$, no further restrictions are placed on any of the variables because singularities due to $\beta \rightarrow 0$ linearly with R are always cancelled by the appearance of R in the numerator. However if $A \neq 0$, a second singularity appears in the second of equations (A-1) which can only be cancelled if $\alpha \rightarrow \pi/2$ as $\beta \rightarrow 0$. Thus, all isotensoid shapes have zero slope $(dZ/dR = 0)$ at $R = 0$ for $A \neq 0$. In order to compute these shapes, it is necessary to determine proper initial conditions. To this end assume

$$\beta \cong C_1 R + C_2 R^2 \qquad\qquad R \rightarrow 0 \qquad\qquad \text{(A-3)}$$

and

$$\alpha \cong \pi/2 - C_3 R - C_4 R^2 \qquad\qquad R \rightarrow 0 \qquad\qquad \text{(A-4)}$$

The constants $C_1 - C_4$ are evaluated by substituting for β and α into Equations (A-1), making appropriate approximations for small R and matching coefficients of powers of R. After some manipulation, there results

$$\beta = \sqrt{\frac{\Omega - A^2}{2}} \, R - \frac{K A}{10 \sqrt{\frac{\Omega - A^2}{2}}} \, R^2 \qquad\qquad \text{(A-5)}$$

104

$$\alpha = \pi/2 - AR - \frac{K}{2} R^2 \qquad\qquad (A-6)$$

$$Z = - \frac{AR^2}{2} - \frac{KR^3}{6} \qquad\qquad (A-7)$$

Equations (A-5), (A-6), and A-7) can be used to generate initial conditions for α , β , and Z which generate isotensoid shapes closing on the axis of symmetry. Note that real solutions are only possible **if**

$$\Omega - A^2 > 0 \qquad\qquad (A-8)$$

Aside from the restriction of Equation (A-8), one can for all combinations of K , Ω , A ($\Omega - A^2 > 0$) determine initial conditions which generate surfaces which close on the axis of symmetry.

Illustrative examples of $\Omega = 1$, $K = 1$, and $\Omega = 1$, $K = 0$ both with parametric variation of A are demonstrated in Figures 24 and 25. Figure 26 shows the fiber angle for a typical loading; $\Omega = 1$, $K = 0$, $A = 0.1$.

105

REFERENCES

1. Dong, S. B.: Analysis of Laminated Shells of Revolution. J. of the Engr. Mech. Div., ASCE, vol 92, no. EM6, Dec 1966, pp. 135-155.

2. Rosen, B. W.; Dow, N. F.; and Hashin, Z.: Mechanical Properties of Fibrous Composites. NASA CR-31, 1964.

   Tsai, S. W.: Structural Behavior of Composite Materials. NASA CR-71, 1964.

   Adams, D. F.; and Doner, D. R.: Longitudinal Shear Loading of a Unidirectional Composite. J. Composite Materials, vol. 2, 1967, pp. 4-17.

   Chen, C. H.; and Cheng, S.: Mechanical Properties of Fiber Reinforced Composites. J. Composite Materials, vol. 1, 1967, pp. 30-41.

3. Flugge, W.: Stresses in Shells. Springer-Verlag, 1960.

4. Anon.: Aerodynamic Characteristics of Parachutes. Reports and Memoranda No. 862, compiled by R. Jones, Aeronautical Research Committee, London, H. M. Stationery Office, June 1923.

5. Kitzmiller, A. H.; DeHaven, C. C.; and Young, R. E.: Design Consideration for Spiralloy Glass-Reinforced Filament-Wound Structures as Rocket Insert Parts. Presented at the ARS Annual Meeting, Washington, D. C., November 1959.

6. Brink, N. O.: Research on Expandable Airlock Utilizing the Elastic Recovery Principle. NASA CR-351, 1965.

7. Zickel, S.: Isotensoid Pressure Vessels. ARS Journal, vol. 32, no. 6, June 1962, pp. 950-951.

8. Schuerch, H. U.; Burggraf, O. R.; and Kyser, A. C.: A Theory and Applications of Filamentary Structures. NASA TN D-1692, 1962.

9. Burggraf, O. R.; and Schuerch, H. U.: Analyses of Axisymmetric, Rotating Pressurized Filamentary Structures. NASA TN D-1920, 1963.

10. Pipkin, A. C.; and Rivlin, R. S.: Minimum-Weight Design for Pressure Vessels Reinforced With Inextensible Fibers. JAM March 1963.

11. Kyser, A. C.: The Uniform-Stress Spinning Filamentary Disk. NASA CR-106, 1964.

12. Byrd, P.F.; and Friedman, M. D.: Handbook of Elliptic Integrals for Engineers and Physicists. Lange, Maxwell & Springer, 1954.

13. Niederer, P.: Development of a High Altitude Stokes Flow Decelerator. Astro Research Corporation Report ARC-R-236, 1966.

14. Young, R. E.: Filament Wound Hollow Elements and Methods for Making Same. Patent #2,843,153, July 15, 1958.

15. Young, R. E.: Filament Wound Vessels and Methods for Forming Same. Patent #3,047,191, July 31, 1962.

16. Schuerch, H. U.; and Kyser, A. C.: Isotensoid Torus Design. Astro Research Corporation Report ARC-R-9, November 9, 1960.

17. Williams, Jerry G.; and Goodman, George P.: Structural and Materials Investigation of a 1/8-Scale-Model Space Structure of Toroidal Configuration and Filamentary Construction. NASA TN D-2652, February 1965.

18. Anon: A Report on the Research and Technological Problems of Manned Rotating Spacecraft. NASA TN D-1504, pp. 55-56, August 1962.

19. Anon: Materials for Space Operations. NASA SP-27, pp. 15-16, December 1962.

20. Schuerch, Hans U.: Isotensoid Structure. Patent No. 3,121,451, February 18, 1964.

05U OUL 5T   50 5US   70103 00042
PICATINNY ARSENAL
PLASTICS TECHNICAL EVALUATION CENTER
DOVER, NEW JERSEY 07801

ATT SMUPA-VP3

ble (Section 158
1) Do Not Return

"The aeronautical and space activities of the United States shall be conducted so as to contribute . . . to the expansion of human knowledge of phenomena in the atmosphere and space. The Administration shall provide for the widest practicable and appropriate dissemination of information concerning its activities and the results thereof."

— NATIONAL AERONAUTICS AND SPACE ACT OF 1958

NASA SCIENTIFIC AND TECHNICAL PUBLICATIONS

TECHNICAL REPORTS: Scientific and technical information considered important, complete, and a lasting contribution to existing knowledge.

TECHNICAL NOTES: Information less broad in scope but nevertheless of importance as a contribution to existing knowledge.

TECHNICAL MEMORANDUMS: Information receiving limited distribution because of preliminary data, security classification, or other reasons.

CONTRACTOR REPORTS: Scientific and technical information generated under a NASA contract or grant and considered an important contribution to existing knowledge.

TECHNICAL TRANSLATIONS: Information published in a foreign language considered to merit NASA distribution in English.

SPECIAL PUBLICATIONS: Information derived from or of value to NASA activities. Publications include conference proceedings, monographs, data compilations, handbooks, sourcebooks, and special bibliographies.

TECHNOLOGY UTILIZATION PUBLICATIONS: Information on technology used by NASA that may be of particular interest in commercial and other non-aerospace applications. Publications include Tech Briefs, Technology Utilization Reports and Technology Surveys.

Details on the availability of these publications may be obtained from:

SCIENTIFIC AND TECHNICAL INFORMATION DIVISION

NATIONAL AERONAUTICS AND SPACE ADMINISTRATION
Washington, D.C. 20546